Design, Manufacturing, and Characterization of a Novel Ceramic Matrix Composite

by

Taylor Robertson

A thesis proposal submitted to the Faculty of Graduate and Postdoctoral Affairs in partial fulfillment of the requirements for the degree of

Doctor of Philosophy

in

Mechanical Engineering

Carleton University

Ottawa, Ontario

Abstract

A novel ceramic matrix composite (CMC) system consisting of a commercially available SiC fibre, variations of electrophoretically deposited (EPD) fibre-matrix interphases, and a liquid metal melt infiltrated matrix was designed and characterised. A factorial design of experiments approach was undertaken to evaluate the deposition variables which would result in a functioning fibre-matrix interphase. A 2^{5-2} partial factorial design matrix was selected with factors: electric potential, deposition time, surfactant, binder, and solids loading. The design matrix was replicated for four different EPD fibre-matrix interphase coating combinations: Al_2O_3/SiC, BN/PSZ, ZrC/ZTA, and SiC/Si_3N_4/SiC. Microcomposites were evaluated for tensile properties using a standard displacement controlled tensile test program. Microcomposites were tested at room temperature immediately following fabrication and following exposure to a standard atmosphere at 1000 °C for 1 h. Samples with ZrC/ZTA and SiC/Si_3N_4/SiC coatings demonstrated the best tensile properties in room temperature tests while samples with BN/PSZ and SiC/Si_3N_4/SiC coatings demonstrated the best retention of tensile properties following high temperature exposure. Subsequent SEM analysis revealed that coatings with smaller particle diameters as the inner layer of the fibre-matrix interphase coating produced more uniform coatings and the less fibre degradation due to oxidation following high temperature exposure. Additional microcomposites were fabricated for high temperature tensile testing; however, these samples were unable to bear recordable loads, an SEM examination revealed significant degradation of the matrix phase beneath the high temperature adhesive. Optical microscopy was used to evaluate coating thicknesses of coated fibre bundles prior to heat treatments. Measured coating thickness indicated that generally higher deposition times resulted in thicker coatings; however, coatings produced using 25 V electric potential were thicker than coatings produced using 12.5 V and 50 V electric potentials. This is likely due to a greater deposition efficiency factor at 25 V. FEA analysis was used to evaluate the electrical properties of an idealized version of the stationary EPD cell. This analysis showed a significant variation in the electric field along the fibre axis as well as a significant variation in electrical field between fibres in the centre of the fibre bundle and on the outer edge of the fibre bundle.

Acknowledgements

To my co-supervisors Rick Kearsey and Xiao Huang, I have become greatly indebted to you over the course of this work. I have relied upon you for advice, guidance, encouragement, insight, and at times consolation. I have learned so much from the two of you and I'm grateful for your patience as I've developed my abilities over these years. It is not an exaggeration to say that without the two of you, I would not have the life I am currently enjoying in Ottawa.

To my colleagues at the National Research Council of Canada, thank you for the instructive discussions, the assistance with and operation of vital equipment utilized in this work, and always being available when I had a technical question or needed to conduct another HIP run over a long weekend. Scott Yandt, thank you for being a never ending source of technical know-how and a sanity check on some of my proposed approaches. Ryan MacNeil, Luc Lafleur, Olga Lupandina, Clinton Carnegie and Rolf Floeren thank you for teaching me the intricacies of the facilities under your care and accommodating the numerous requests that I've made of you. Devin Wang, thank you for helping me with experimental work when my schedule was overwhelming and for always being willing to aid me in exploring tangential research paths. Finally, I would like to thank the Aerospace Research Centre's Aerospace Futures Initiative program and everyone who has contributed to ensuring this worthy program exists. Many of the resources I relied upon for this work were made available through the Aerospace Futures Initiative program.

To my friends and family, thank you for providing moral support through the ups and downs of graduate research. Mom and Dad, thank you for always supporting me and providing a strong foundation which allowed me to take risks and explore. Erin, thank you for everything.

Contents

List of Figures

List of Tables

Nomenclature

Symbol	Definition	Equation
$a_1, a_2, a_3, b_1, b_2, b_3, c_1, c_2, c_3$	Interphase coefficients from [1]	(8)-(16), (18)-(20), (42), (44)
$\mathbb{a}, \mathbb{b}, \mathbb{c}, \mathbb{d}$	Heat Capacity at constant pressure constants	(35)
A_{sr}	Amplitude of surface aspirates	(21)
A_{xc}	Cross Sectional Area	(29), (30)
A_H	Hamaker constant	(23)
cn	Constant based upon Newtonian nature of a fluid	(22)
C	Constant	(31), (40)
C_{bulk}	Boundary Condition	(26), (27)
C_p	Heat capacity at constant pressure	(34), (35)
d_c	Capillary diameter	(39)
D	Diffusion Coefficient	(26), (27), (32), (39)
α	Dunder's parameter	(4)
ϵ^T	Stress due to thermal expansion mismatch	(8)
ε	Dielectric constant	(24), (25)
$\varepsilon_p, \varepsilon_u$	Strain	(41)
σ	Strength/Stress	(5)-(9), (18)-(20), (38), (40), (41)-(43)
Ξ	Crack Tip Ellipse Axis	(5), 33
η	Viscosity	(22), (29), (38)
ϱ	Area Fraction of Fibre (R_f/R)	(8)
ρ	density	(22), (29), (39), (40)
φ	Charge density	(48)
μ	Frictional coefficient along the debonding surface	(8), (9)
θ	Contact angle	(38)
ξ	Coefficient relating to sliding resistance	(8), (9)
ψ	Surface potential	(24)
ζ	Zeta potential	(28)
τ	Treatment effect	(41)-(44)
$\varkappa, \aleph$	Sintering exponents	(31)
ד	Thickness of Grain Boundary	(32)
Γ	Sintering Scaling Dimension	(32)
Ω	Atomic volume	(32)
E	Elastic Modulus	(4), (10), (12)-(14), (17)-(19), (41), (42), (44)

E	Electric Field	(48)
EV	Electric Potential	(29)-(30)
e_0	Electron charge	(24), (25)
F	Faraday Constant	(27)
F_l	Flux of gas particles	(33)
f_d	Deposition efficiency factor	(29)
$\mathcal{g}$	Energy release rate of debond crack growth	(8)
g	Acceleration due to gravity	(22)
G_G	Grain Size	(32)
G_f	Gibb's Free Energy	(34), (36)
h	Film/infiltrant thickness	(22), (38)
H	Shortest distance between two spheres	(23)
$\mathcal{H}$	Enthalpy of formation	(34)
I	Current Density	(27), (30)
k_B	Boltzmann Constant	(32)
k_{sz}	Specific electrical conductivity of suspension zone	(30)
K_T	Reaction constant	(36), (37)
$1/\kappa$	Debye length	(24)
l_c	Distance along crack tip	(5), 33
l	Length scale of matrix cracking	42-43
$\mathcal{L}$	Elastic strain index	(41), 42
L_D	Length Dimension	(32)
m	Weibull Modulus	(3)
M, M_A, M_B, M_c	Molar Mass	(39), (40), (33)
MV	Molar Volume	(39), (40)
P	Probability of Fracture (Weibull Modulus)	(3)
p	Partial pressure	(37)
q, q'	Kinetic constant, unit of velocity	(28)
V	Volume	(3)
V	Volume fraction	(1), (2), (11)
v	Poisson's Ratio	(12)-(14)
r	Crack tip radius	(5), 33
R_f, R	Fibre radius, Radius	(23), (24), (38), (40)
R_G	Universal Gas Constant	(33), (34), (36)
t	time	(26), (31), (38)
T	Temperature	(32), (33), (34), (36)
U	Rate substrate is drawn from bath	(22)
W_A, W_R	Energy of attraction and repulsion	(23),
z	valence	(24), (26)

Abbreviations

Abbreviation	Definition	Page Of First Occurrence
CMC	Ceramic Matrix Composite	1
CTAB	Cetrimonium bromide	35
CVD	Chemical Vapour Deposition	9
CVI	Chemical Vapour Infiltration	2
DLS	Dynamic Light Scattering	38
DoE	Design of Experiments	28
DVLO	Derjaguin-Landau-Verwey-Overbeek Theory	18
EDX	Energy Dispersive X-Ray	46
ELS	Electrophoretic Light Scattering	38
FMI	Fibre-Matrix Interphase	2
PALS	Phase-Analysis Light Scattering	38
PIP	Polymer Infiltration and Pyrolysis	9
PyC	Pyrolytic Carbon	9
RMI	Reactive Melt Infiltration	2
SI	Slurry-based Infiltration	9

1. Introduction

1.1 Ceramic Matrix Composites as High Temperature Materials

Superalloys have traditionally been used for the majority of structural applications where the temperature is expected to reach or exceed 1000 ˚C [2]. Advances in alloy design have steadily improved the high temperature limit at which superalloys can be used; however, these advances have been subject to greater and greater diminishing returns as applications approach the physical limit imposed by their inherent incipient melting temperatures [3]. In many high temperature applications, for example gas turbines, further increasing the operating temperature leads to improved efficiencies and performance [4] [5]. It is therefore advantageous to develop alternative materials which can operate at temperatures beyond superalloy's capability as seen in Figure 1.

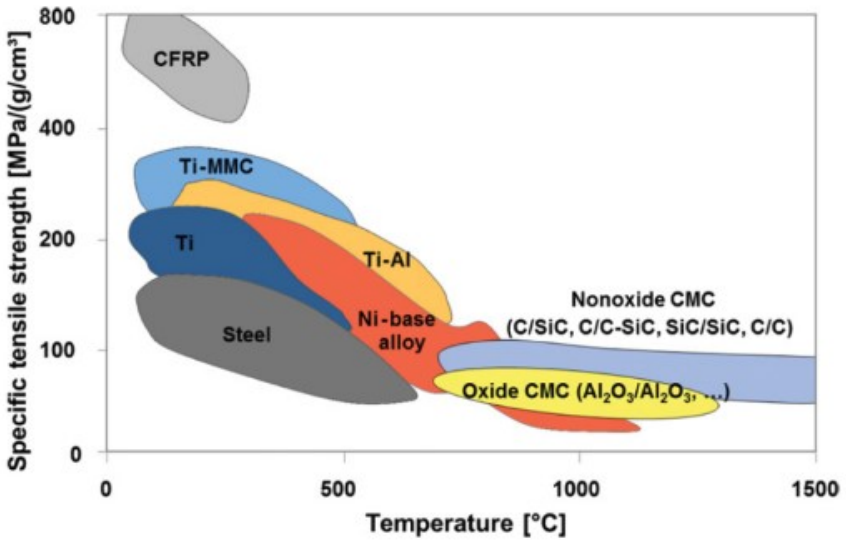

Figure 1: Specific strength of material classes vs. temperature range for material class applications [6]

In the past, advanced ceramics have been examined as a potential high temperature structural material because they possess high strength, high stiffness, good creep resistance, good environmental and chemical stability, and low density [7]. Unfortunately, their low damage tolerance, especially under tensile loads, has prevented their adoption in applications where reliability is crucial. Ceramic matrix composites (CMCs), on the other hand, employ an engineered microstructure of two or more ceramic phases to take advantage of the excellent high temperature properties which advanced ceramics exhibit while overcoming

their inherent brittle nature [3]. The improved reliability of CMCs has renewed interest in the potential adoption of ceramic components for high temperature structural applications.

Despite the attractive properties offered by CMCs, two major challenges prevent their widespread adoption. The high cost of production caused by complex production techniques places economic barriers to the availability of CMCs for high temperature applications. Secondly, the challenges of characterizing and certifying these complex and anisotropic material systems has further reduced their availability for high temperature applications. The high cost of CMCs is being addressed by new production techniques which reduce process times and materials waste as well as efforts to bring the benefits of economy-of-scale to CMC production [8] [9]. For fibre-based CMCs, manufacturing techniques have evolved from matrices being produced entirely by isothermal chemical vapour infiltration (CVI) with production times of several months per panel to reactive melt infiltration (RMI) and polymer derived ceramic infiltration techniques which can be accomplished in days [10] [11]. The standardization of characterization techniques, advances in modeling and simulation, and the generation of larger material properties knowledgebases are some of the approaches being taken to reduce the challenges presented by characterization and certification.

Fibre-based CMCs contain (1) a fibre phase which provides the structural integrity of the composite, (2) a matrix phase which transfers load between fibres and protects them from environmental degradation and in most cases (3) a fibre-matrix interphase (FMI) which controls the failure mode. Additionally, some sources consider an environmental barrier system to protect the matrix phase from environmental degradation to be an essential phase in the CMC system [12]. Pseudo-ductile behaviour is achieved through the incorporation of a mechanical fuse phase (to act as a sacrificial body) which directs cracks away from the structurally critical fibre phase. This allows damage that accumulates within the matrix during loading to be redirected before damaging the fibre phase. The intact fibres and matrix are then able to assume more of the loading of the CMC system as seen in Figure 2.

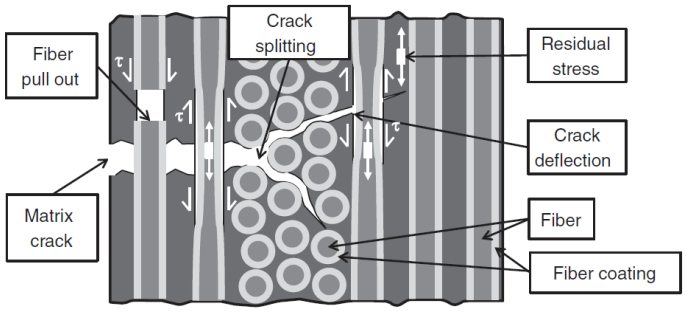

Figure 2: Damage tolerance mechanics within an idealized Ceramic Matrix Composite [6]

As the load on the fibres increases, fibres begin to fail individually according to the Weibull distribution of their strengths. As individual fibres begin to fail and can no longer bear load, the remaining fibres and intact matrix accumulate a greater share of the load until their carrying capacity is exceeded and failure occurs. The general shape of this failure progression can be seen in Figure 3 where a) indicates the proportional limit (the point where damage starts to accumulate in the matrix) of the idealized CMC, and b) indicates the pseudo-ductile region.

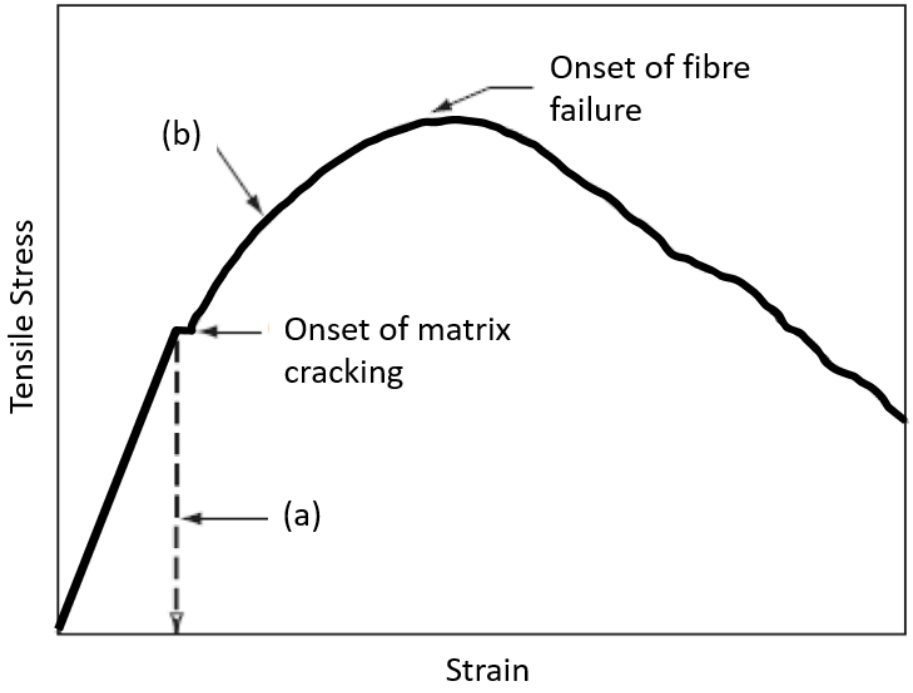

Figure 3: Idealized stress-strain failure curve of a fibre reinforced CMC [13]

The most common sacrificial phase is a weak FMI. The weak FMI easily debonds from the fibre when stressed and redirects matrix cracks which are approaching the fibre parallel to the fibre surface thereby preventing damage to the fibres [14]. Another less common approach is the implementation of a strong FMI. Strong FMIs absorb damage by deflecting incoming cracks into a series of micro-cracks in doing so preventing them from reaching and damaging the fibre. The third strategy is to forego the FMI and use a weak-porous matrix [15]. The weak matrix creates such a low resistance to crack propagation in comparison to the fibre phase that fibres remain undamaged until critical damage accumulation has occurred. This strategy is often used in applications where the operating temperature will remain far below the melting temperature of the matrix to avoid sintering of the matrix in service [16]. Figure 4 shows the relationship between fibre and matrix stiffness, relative fracture energy and ductile to brittle transition. In

this figure, G^1_c is the fracture energy of the fibre-matrix interphase, $G^{(2)}_c$ is the fracture energy of the fibre phase, E_f is the elastic modulus of the fibre phase and E_m is the elastic modulus of the matrix phase.

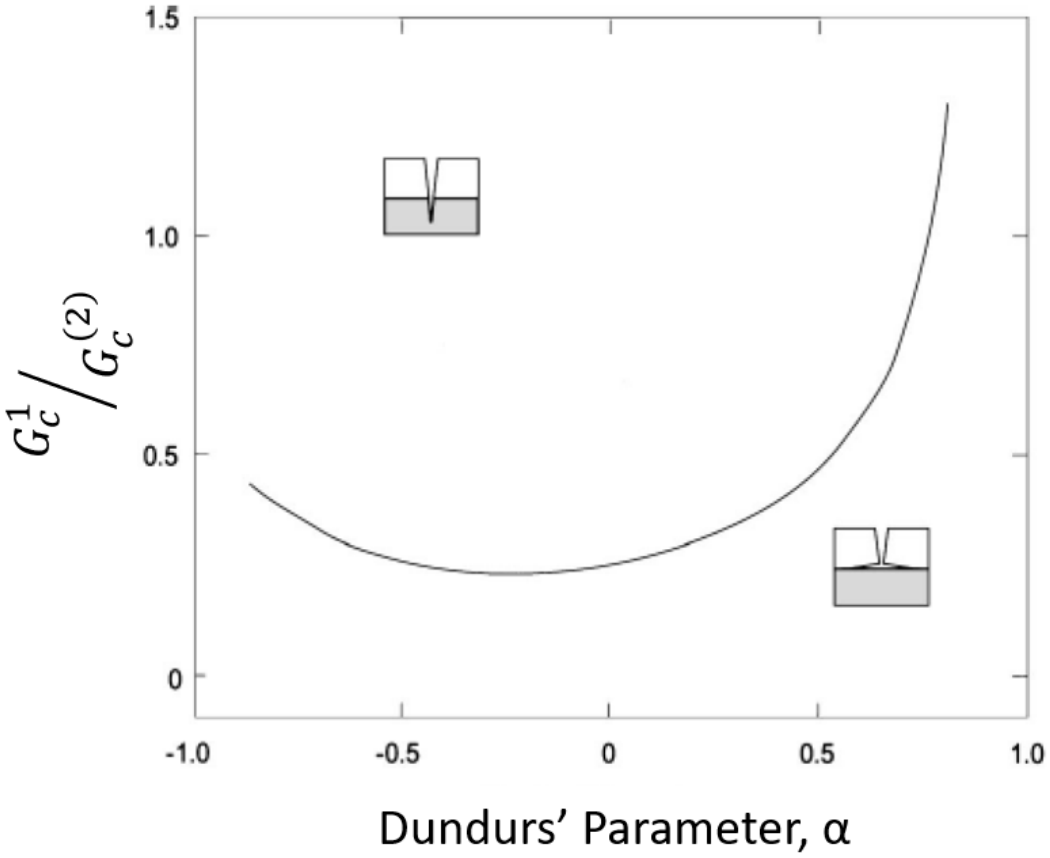

Figure 4: FMI fracture energy (G^1_C) to fibre fracture energy (G^2_c) ratio vs. Dunders' parameter showing mechanical fuse behaviour [1] [17], where Dunders' parameter is given by: $\alpha = \frac{E_f - E_m}{E_f + E_m}$.

1.2 Structure of Thesis

Section 1 of the thesis provides relevant background information and a brief overview of the advantages and challenges offered by CMCs as high temperature materials. Additionally, the structure and contributions of the thesis are covered.

Section 2 consists of the literature review of relevant topics. These topics include contemporary CMC systems, manufacturing techniques for the main components (fibre, FMI, and matrix) of CMCs, design of experiments and multiphysics-based computational modeling. The section concludes with an overview of the research motivation, objectives, and scope.

Section 3 covers the materials and methods utilized in the experimental portion of the work. This includes the sourcing of the raw materials, the factorial experimental design, and the production and characterization of microcomposites.

Section 4 provides the results and discussion of the microcomposite characterization using tensile testing and microscopy.

Section 5 provides the process and results of the multiphysics based computation modeling and a discussion of the implications of the results on this work.

Section 6 presents the conclusions of this research and recommendations for future research work.

1.3 Thesis Contributions

This thesis makes the following contributions to the field of CMC research:

The design and evaluation of an aqueous electrophoretic deposition (EPD) process for the manufacture of ceramic coatings on ceramic fibre bundles

The evaluation of microcomposite samples manufactured through a liquid melt infiltration technique

The application of a multiphysics based computational model to simulate and evaluate the process through which the novel interphase coating is produced

2. Literature Review

2.1 CMC Systems

This section will primarily examine continuous fibre reinforced CMCs, and the terminology and nomenclature present within this section will relate to these CMCs.

CMC systems are typically designated by the chemical composition of their fibre and matrix phases. The nomenclature which will be adopted for this paper is to present CMC systems in the *aa*/*bb* format where *aa* is the fibre phase and *bb* is the matrix phase. If attention is to be drawn to the FMI then it will be noted directly after the fibre/matrix composition.

The mechanical performance of composite systems are typically predicted to follow a rule of mixtures formulation where loading entirely parallel to the fibre axis provides an isostrain rule of mixtures condition providing the upper bound of the composite stiffness (1) and loading entirely perpendicular to the fibre axis provides an isostress rule of mixtures condition providing the lower bound of the composite's stiffness (2) [2].

Isostrain condition:
$$E_C = \sum_i \mathrm{V}_i E_i \tag{1}$$

Isostress condition
$$E_C = \sum_i \frac{\mathrm{V}_i}{E_i} \tag{2}$$

Where E is the elastic modulus and V is the volume fraction where subscripts *c* indicate the overall composite and *i* the composite constituents. There are four main varieties of fibres which can be incorporated into CMCs: carbon, carbide, nitride and oxide. Carbon fibre properties primarily depend upon the level of graphitization and alignment, the diameter, and impurities. Carbide and nitride fibres are covalently bonded crystalline fibres. Their properties primarily depend upon the crystalline structure, grain boundary composition, stoichiometry, and impurities [18]. Oxide fibres consist of crystalline metal oxides. Oxide fibre properties primarily depend upon grain structure, grain boundary composition, amorphous phases, diameter, and defects [19]. Ceramic fibres are brittle in nature and any defects or impurities in the structure will act as a stress concentrator which will quickly compromise the integrity of the fibre. Possible defects include micropores, surface roughness, kinks, non-uniform grain sizes and concentration of impure chemical structures. Defects in the fibre structure are often introduced during processing [9].

2.1.1 Silicon Carbide Fibres

Silicon carbide fibres are polycrystalline fibres consisting of nearly stoichiometric SiC. Commercial SiC fibres have diameters between 10 and 15 μm and are spun into yarns of 400-1600 filaments. Silicon carbide fibres are typically produced through the pyrolysis of a polymer precursor, often Polycarbosilane. Further treatment may include irradiation following pyrolysis to reduce the oxygen content which may segregate to the grain boundaries. This additional step separates 2nd generation and 3rd generation SiC fibres. Properties of commercially available SiC fibres are summarized in Table 1 and Table 2.

Crystalline carbide fibres, behaved as a highly brittle material (fracture toughness from 1-2 MPa $m^{0.5}$ [20]) and failed in a weakest-link failure-mode, can be best modelled using a Weibull distribution with a characteristic strength and Weibull modulus [21]. The strength of crystalline carbide fibres is controlled by the largest defect. The Weibull model provides a statistical description of failure probability based upon the characteristic strength and Weibull modulus shown in equation (3)

$$P = 1 - e^{-\int(\sigma/\sigma_0)^m dV/V_0} \quad (3)$$

Where P is the probability of failure, σ is the stress borne by the fibre, σ_0 is the characteristic strength, m is the Weibull modulus, V is the volume of the specimen and V_0 is a reference volume. The methods used to determine the Weibull parameters are outlined by ASTM standards C1239-13 and C1683-10 [22] [23]. It is important to note that without a reference volume, Weibull characteristics are impossible to apply.

Table 1: Characteristics of commercially available silicon carbide fibres [18]

TABLE 1. Production and Compositional Details for SiC-Based Fiber Types

Trade-Name	Manufacturer	Production Method	Elemental Composition, weight %	Approx. Maximum Production Temp.	~Grain Size, nm (~surface roughness)	Surface composition	Avg. Diam. μm	Fibers Per Tow
Nicalon, NL200	Nippon Carbon	Polymer	56 Si + 32 C + 12 O	1200°C	2	Thin carbon	14	500
Hi-Nicalon	Nippon Carbon	Polymer + Electron irr.	62 Si + 37 C + 0.5 O	1300°C	5	Thin carbon	14	500
Hi-Nicalon Type S	Nippon Carbon	Polymer + Electron irr.	69 Si + 31 C + 0.2 O	1600°C	100	Thin carbon	12	500
Tyranno Lox M	Ube Industries	Polymer	55 Si + 32 C + 10 O + 2.0 Ti	1200°C	1	Thin carbon	11	400/800
Tyranno ZMI	Ube Industries	Polymer	57 Si + 35 C + 7.6 O + 1.0 Zr	1300°C	2	Thin carbon	11	400/800
Tyranno SA 1-3	Ube Industries	Polymer + Sintering	68 Si + 32 C + 0.6 Al	>1700°C	200	Thin carbon	10 – 7.5	800/1600
Sylramic	(Dow Corning) COI Ceramics	Polymer +t Sintering	67 Si + 29 C + 0.8 O +2.3 B + 0.4 N +2.1 Ti	>1700°C	100	Thin carbon + B + Ti	10	800
Sylramic-iBN	COI Ceramics + NASA	Polymer + Sintering + Treatment	Sylramic	>1700°C	>100	Thin in-situ BN (~100 nm)	10	800
SCS-6-9/Ultra SCS	Specialty Materials	CVD on ~30 μm C core	70 Si + 30 C + trace Si + C	1300°C	~100 by ~10	SiC/ Thin carbon	140 – 70/140	mono-filament

Table 2: Mechanical properties of commercially available silicon carbide fibres [18]

TABLE 2. Property and Cost Details for SiC-Based Fiber Types

Trade-Name	Manufacturer	Density, g/cm^3	Avg. R.T. Tensile Strength GPa	R.T. Tensile Modulus GPa	R.T. Axial Thermal Conduct. W/m K	Thermal Expansion, ppm/°C (to 1000° C)	Current Cost, (<5Kg), $/Kg
Nicalon, NL200	Nippon Carbon	2.55	3.0	220	3	3.2	~2000
Hi-Nicalon	Nippon Carbon	2.74	2.8	270	8	3.5	8000
Hi-Nicalon Type S	Nippon Carbon	3.05	~2.5	400–420	18		13000
Tyranno Lox M	Ube Industries	2.48	3.3	187	1.5	3.1	1500/1000
Tyranno ZMI	Ube Industries	2.48	3.3	200	2.5		1600/1000
Tyranno SA 1-3	Ube Industries	3.02	2.8	375	65		~5000
Sylramic	(Dow Corning) COI Ceramics	3.05	3.2	~400	46	5.4	10000
Sylramic-iBN	COI Ceramics + NASA	3.05	3.2	~400	>46	5.4	>10000
SCS-6-9/Ultra SCS	Specialty Materials	~3	~3.5 /~6	390–350/390	~70	4.6	~9000

Reported production techniques for silicon carbide fibres are provided in Table 1 and reported properties for silicon carbide fibres are provided in Table 2. Silicon carbide fibres will experience degradation at temperatures ranging from 650 °C to 1400 °C, with the extent depending upon the atmosphere. In inert environments the property degradation will occur through microstructural evolutions such as grain growth, coarsening, and under stress SiC fibres will exhibit creep [24]. In oxidizing atmospheres, the temperature range at which degradation occurs begins at 1000 °C. This is due to the oxidation of the fibres, SiC will form a protective SiO_2 scale which is most stable at temperatures from 650 to 850 °C [25]. Above 1300 °C the growth of SiO_2 scale will leave the parabolic regime and enter the breakaway regime leading to the rapid degradation of SiC fibres. In the breakaway regime, cracks forming in the SiO_2 scale allow oxygen to penetrate towards previously protected SiC leading to rapid oxidation no longer rate controlled by diffusion of oxygen through SiO_2. The most aggressive atmosphere under which SiC will be subject to is moisture-containing, high-temperature environments. This is due to the volatilization of the SiO_2 scale through the formation of silicon hydrides. Stress crack corrosion has also been shown to play a significant role in the lifetime of SiC fibres at elevated temperatures in aggressive environments. The mechanism proposed by Gauthier et al. [26] is the reaction of oxygen with free carbon trapped between grains. The associated formation of SiO_2 or SiOC at the crack tip is accompanied by a volume increase, forcing the grains open.

2.1.2 Silicon Carbon-Nitride Fibres and Silicon Carbon-Boron-Nitride Fibres

In an effort to produce a covalently bonded fibre with greater oxidation resistance than SiC, researchers have explored compositions of Si-C-N-B. SiCN and SiCNO fibres have been produced from a novel polycarbosilazane cross-linked using polysilasilazane cured in an inert atmosphere with γ-ray radiation [9] [27]. Evidence of greater oxidation resistance of the as-produced SiCNO fibres was presented as the SiO_2

oxide scale layer which developed was thinner than that seen in SiC fibres and the oxidation kinetics remained parabolic up to 1400 °C, 200 °C greater than that seen on SiC. SiCBN ceramics, which have a greater oxidation resistance than SiCN, can be spun into fibre form using a polyborosilazane precursor. SiCBN fibres have shown good oxidation resistance up to 1500 °C [9].

2.1.3 Carbide Fibre Composites

CMCs with silicon carbide fibres within silicon carbide matrices (SiC/SiC) form the bulk of industrialization and research efforts for CMCs targeted at temperatures above 1000 °C and below 1800 °C. Several review papers have been published upon the variety of SiC/SiC composites, their processing techniques and their properties [28] [29] [30]. SiC/SiC composites originally incorporated a pyrolytic carbon (PyC) FMI deposited onto the fibre using a chemical vapour deposition (CVD) process. This interphase was chosen due to the fibre pull-out properties witnessed in C/C composites which is attributed to cleaving along basal planes parallel to the fibre direction [14] [31]. PyC interphases were soon replaced with boron nitride interphases produced through CVD [32]. Boron nitride has a similar molecular structure to graphitic carbon; however, the oxidation resistance of BN far exceeds that of PyC and is therefore a preferable material for carbide based CMCs. During oxidation BN forms a borosilicate glass which forms a barrier to further oxygen penetration until the glass is itself volatized by water vapour, this greatly slows down the oxidation of the BN interphase in comparison to PyC which immediately volatizes into $CO_{(g)}$ and $CO_{2(g)}$ [33] [34]. The final processed fiber is shown in Figure 5.

The four process routes to matrix production for SiC/SiC composites are CVI, polymer infiltration and pyrolyzation (PIP), slurry-based infiltration (SI) and RMI. Each of these production techniques will be addressed with more detail in section 2.2. Typically, CVD is reserved for applications where the matrix requires a highly refined microstructure where cost and time constraints are not a concern. PIP is reserved for applications where the composite cannot retain any unreacted metal and precursor phases. For example, applications where the dielectric properties of the composite are strongly considered [35]. The volume loss incurred by converting the polymer into a ceramic requires multiple reinfiltration cycles and may lead to porosity and microcracking within the matrix. RMI is favoured in applications where manufacturing time is to be minimized at the expense of producing a matrix with flaws such as residual metal, residual carbon constituents, and porosity. This is the production method which is used to produce General Electric's HiPerComp™ which is the first CMC to be adopted within a commercial turbine engine [11]. Slurry-based processing techniques have similar benefits and drawbacks to PIP systems depending upon the purity of the powder within the slurry and the volume loss converting the green body to a sintered ceramic. A typical SiC/SiC thus produced is shown in Figure 5.

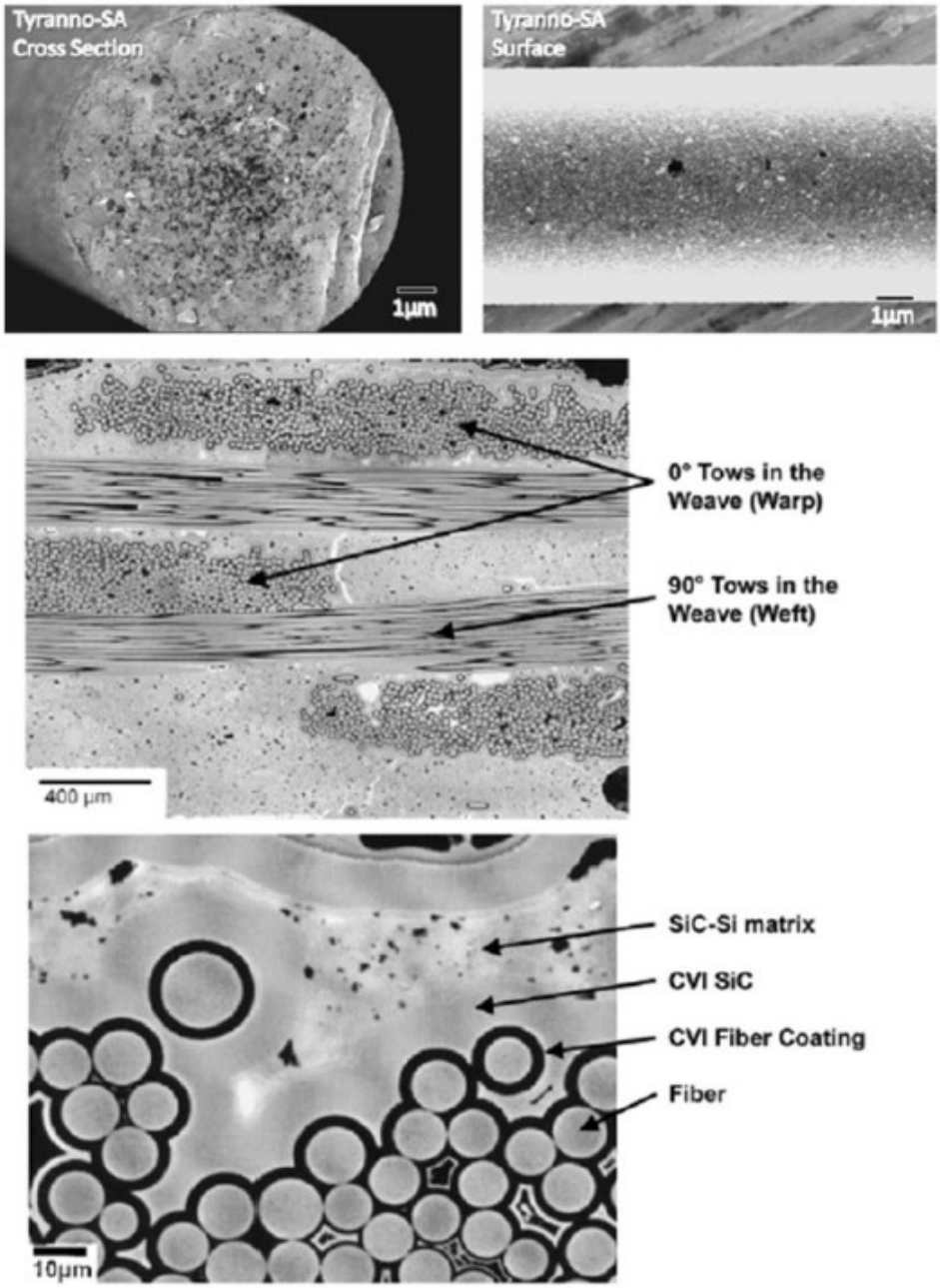

Figure 5: Cross section, surface of a SiC fibre [36]; cross section of a SiC/SiC composite [11]

The microstructure of the SiC matrix will affect the mechanical properties of the composite. The ability to maintain load and contribute to the stiffness and strength of the composite will be particularly affected by

the microstructure and defect structure of the matrix. The microstructure with respect to SiC/SiC includes the grain size, grain orientation, and segregated content within grain boundaries. The defect structure includes porosity, microcracking, residual stress states, and unreacted precursors. Additionally, the properties of the interphase will have some effect on the matrix's ability to transfer loading between fibres, this will be covered in greater detail in section 2.2.2. The stiffness and strength of the matrix will affect the stress-strain behavior of the composite up until the proportional limit has been reached, beyond this point the hysteresis response of the composite will be primarily fibre dependant [37].

Silicon carbide and silicon nitride fibres have been included in multi-phase covalent matrices. Most commonly these matrices will be based upon a SiC/SiC baseline design and will incorporate additional carbide or boride phases. The intention of the additions is to improve the oxidation resistance properties of the composite or to improve the mechanical properties of the matrix. An example of a composite with its matrix altered to improve oxidation resistance includes SiC/Si-B-C which capitalizes on the formation for borosilicate glass to improve the oxidation resistance properties [38]. Another example of additional phases included with the intention to improve the mechanical properties of the carbide matrix include the addition of carbon nanotubes to the carbide matrix with the intent of improving the fracture toughness of the matrix [39].

2.2 Component Design

2.2.1 Fibres

Fibre selection is critical to the performance of CMC. The fibres will ultimately determine the stiffness, tensile strength, creep properties, and fatigue properties of CMC. Additionally, the fibre choice will drive design decisions for the FMI, the matrix, and the environmental barrier coating. Finally, the availability and cost of the fibres will determine viability of the designed CMC.

The intended operating environment for the CMC must be considered when choosing a fibre (and matrix), if the intended application requires strength retention during lengthy temperature exposures above 1425 °C then the most appropriate fibre will be carbon; however, a much greater burden will be placed upon FMI, matrix, and environmental barrier coating design to prevent the degradation of the fibre phase through oxidation. If the intended application will be for temperatures between 1000 °C and 1425 °C then commercially available SiC fibres will perform adequately. Below 1000 °C oxide fibres will be sufficient and may offer cost savings and oxidation resistance [6].

The desired fibre architecture will also play a role in fibre selection due to the limitations placed upon fibres with respect to their bending radii [40].

2.2.2 Interphase

CMCs consist of both brittle fibres and a brittle matrix, to prevent a crack from propagating catastrophically through both components a mechanical fuse is necessary. Initial explorations into CMCs produced few results which were promising. Cracks which developed within brittle matrices at low stresses could easily traverse through the brittle ceramic fibres resulting in a composite which behaved much like a porous ceramic. The first success in CMC production came from the labs of Sambell et al during their work on carbon fibre reinforced glass [41]. It was discovered that a thin layer of pyrolytic carbon coating the carbon fibres allowed cracks to be deflected along the fibres rather than through them. This discovery enabled future work on CMCs and weak FMIs [17].

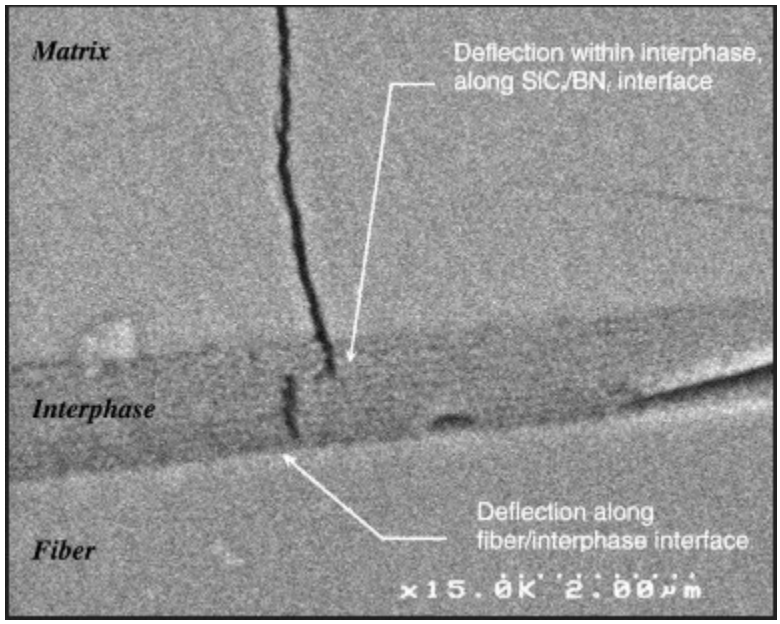

Figure 6: Matrix crack deflection within a SiC/BN multilayered FMI [42]

A properly designed FMI diverts the path of a crack propagating through the matrix into a direction that is parallel to the fibre axis. The deflection of the crack and associated dispersion of fracture energy alleviates the sharp plastic deformation zone which precedes the crack tip, thereby preventing the plastic deformation zone from fracturing the fibre. To successfully deflect or adsorb cracks FMIs must preferentially fail parallel to the fibre's primary axis. Additionally, the energy required to generate cracks within the FMI must be lower than the energy to generate cracks within the fibre phase. Original analysis of this behavior was first presented by He & Hutchison [43] and has been incorporated into many studies on CMC interfaces [44, 45, 17]. According to this analysis the ratio of interface fracture energy to fibre fracture energy should be less than values ranging from 0.4 to 1.25; the exact ratio is based upon the Dunders' parameter of the

composite. The Dunders' parameter (α) is given by equation (4), which is controlled by the elastic modulus of the fibre (E_f) and the elastic modulus of the matrix (E_m).

$$\alpha = \frac{\overline{E_f} - \overline{E_m}}{E_f + E_m} \tag{4}$$

Where the moduli's given in the nominator are the plane strain moduli given by $\overline{E_x}=E_x(1-\nu^2)$.

The He & Hutchison [43] analysis provides a good rule of thumb for interface selection; however, a more nuanced approach must take into account the stress field propagated ahead of a crack tip and its interaction with the interface. This stress field was initially described by Cook & Gordon [46], the interaction of this stress field with the varying strengths and moduli of the interface has been formalized by Lamon [1]. The r-axis runs along the crack length and the z-axis runs parallel to the crack opening direction (as shown in Figure 7).

$$(\Xi_a - \Xi_b)^2 \left(\frac{\sigma_{rr}}{\sigma_a}\right)_{z=0} = -{\Xi_a}^2 + \frac{\Xi_a|r|}{\sqrt{r^2 - {\Xi_a}^2 + {\Xi_b}^2}}\left[\Xi_a - \frac{b^2(\Xi_a - b)}{r^2 - {\Xi_a}^2 + {\Xi_b}^2}\right] \tag{5}$$

$$(\Xi_a - b)^2 \left(\frac{\sigma_{zz}}{\sigma_a}\right)_{r=0} = {\Xi_b}^2 + \frac{\Xi_a|r|}{\sqrt{r^2 - {\Xi_a}^2 + {\Xi_b}^2}}\left[\Xi_a - 2b + \frac{b^2(\Xi_a - \Xi_b)}{r^2 - {\Xi_a}^2 + {\Xi_b}^2}\right] \tag{6}$$

Where Ξ is the axis of the crack tip ellipse with subscripts *a* and *b* notating major and minor axis, respectively.

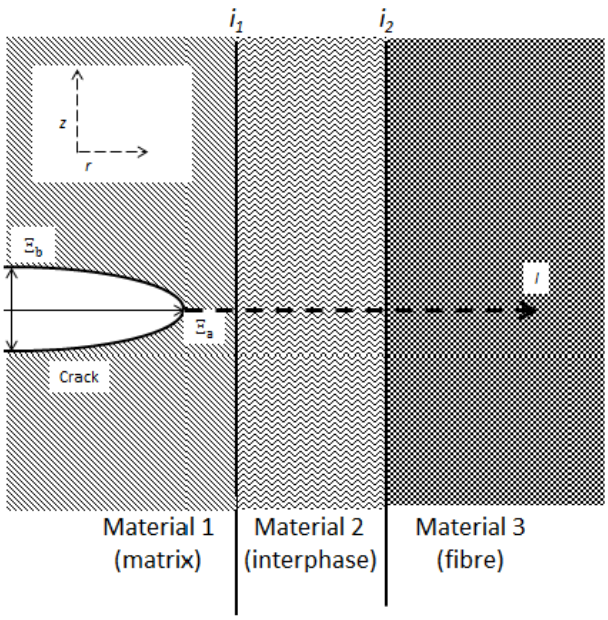

Figure 7: Orientation of axis and directions for equations (5)-(7 a, b)

To initiate the debonding behavior which leads to pseudo-ductile failure in CMCs the crack-tip stress field needs to generate cracks parallel to the fibre axis. This will either be mode II cracks (shear stress acting parallel to the plane of the crack) generated by σ_{zz} stress or mode I cracks (tensile stress normal to the plane of the crack) generated by σ_{rr} stress, or a combination of the two. Furthermore, these cracks must be generated and propagated before transverse fracture within the fibre. This failure criterion can be expressed by equations (7 a, b). Where subscripts *r* and *z* indicate directions parallel to the crack primary axis and perpendicular to the crack primary axis respectively. Interfaces bordering the interphase (Material 2) are given the notation i_1 and i_2 where material 1 is the cracked material (matrix), material 2 is the interphase and material 3 is the uncracked material (fibre) (Figure 7). The distance from the crack tip along the r-axis is assigned symbol *l* [1].

$$\frac{\sigma^c_{II\,2}}{\sigma^c_{I\,3}} \leq \frac{\max \sigma_{rr}(r=l_{i1},l_{i2})}{\max \sigma_{zz}(r>l_{i2})}, \quad \frac{\sigma^c_{I\,2}}{\sigma^c_{I\,3}} \leq \frac{\max \sigma_{zz}(r=l_{i1},l_{i2})}{\max \sigma_{zz}(r>l_{i2})} \qquad (7\text{ a, b})$$

Where $\sigma^c_{II\,2}$ is the mode II failure strength of material 2 (interphase), $\sigma^c_{I\,2}$ is the mode I failure strength of material 2 (interphase), $\sigma^c_{I\,3}$ is the mode I failure strength of material 3 (fibre), $\max \sigma_{rr}(r = l_{i1}, l_{i2})$ is the maximum r-axis stress component of the crack-tip stress field found between interface 1 and 2, *i1* and *i2* in Figure 7 respectively, and $\max \sigma_{zz}\,(r > l_{i2})$ is the maximum z-axis stress component at distances greater than interface 2.

The overall axial stress within the composite wherein the interphase begins to crack is assigned the symbol (σ_i). Once cracks are initiated within the interphase, they travel parallel to the fibre generating debonding between the fibre and the matrix, this debonding transfers load from the matrix to the fibre. Debonding can be divided into three regions, (1) the region where bonding is still intact and the load is shared between the fibre and the matrix, (2) the region where debonding is progressing and matrix stress is being shed to the fibre through frictional loading, and (3) the region where debonding is complete and the fibre bears the load. Debonding is governed by the elastic properties of the fibre, matrix, and composite (E_f, E_m, $\bar{E}v_f$, v_m), fibre and matrix volume fractions (V_f, V_m), fibre radius (R_f), residual processing stress due to thermal expansion mismatch (ϵ^T), energy release rate of debond crack growth ($\mathcal{G}$), the frictional coefficient along the debonding surface (μ), and the peak stress (σ_p). Loading due to frictional sliding resistance is given by equation (8).

$$\Delta\sigma_f = \frac{1-\varrho}{\varrho}\frac{1}{c_1 c_3}\sqrt{\frac{E_m \mathcal{G}}{R_f}} - \frac{\bar{\sigma_r}}{b_1}\left[1 - e^{-\xi}\right] \tag{8}$$

$$\xi = \frac{2\mu b_1 E_m}{R_f b_2 \sigma_p} \tag{9}$$

$$a_1 = \frac{E_f}{\bar{E}} \tag{10}$$

$$a_3 = 0, \text{ when } V_f = V_m \tag{11}$$

$$b_1 = \frac{\left\{(1-v^2)E^* + (1-v)^2 E_m - (1+v)\left[2(1-v)^2 E_f + (1-2v)\left(1-v+\varrho(1+v)\right)\left(E_m + E_f\right)\right]\right\}}{2v(1-v)[(1+v)E^* + (1-v)E_m]} \tag{12}$$

$$b_2 = \frac{(1+v)E_m\left\{2(1-v)^2 E_f + (1-2v)[1-v+\varrho(1+v)]\left(E_m - E_f\right)\right\}}{(1-v)E_f[(1+v)E^* + (1-v)E_m]} \tag{13}$$

$$b_3 = \frac{\varrho(1+v)\left\{(1-\varrho)(1+v)(1-2v)\left(E_f - E_m\right) + 2(1-v)^2 E_m\right\}}{(1-v)(1-\varrho)[(1+v)E^* + (1-v)E_m]} \tag{14}$$

$$c_1 = (2\varrho)^{-1}(1-\varrho a_1)(b_2 + b_3)^{1/2} \tag{15}$$

$$c_2 = \frac{1}{2}a_1(b_1 + b_2)^{1/3}$$

$$c_3 = \frac{1-\varrho}{1-\varrho a_1} \tag{16}$$

$$E^* = \varrho E_m + (1-\varrho)E_f \tag{17}$$

The normal stress upon the fibre, σ_r, is given the superscript $^-$ to indicate that this is the normal stress within the debonded region. The normal stress is determined using equation (18).

$$\sigma_r^- = -\frac{(1-\varrho)}{\varrho}\left(\frac{b_1}{c_3}\right)\left[\bar{\sigma}_0 - \bar{\sigma}_i + \frac{\varrho a_3 c_3}{b_1}(\bar{\sigma}_0 - \bar{\sigma})\right] \tag{18}$$

$$\sigma_i = \frac{1}{c_1}\left(\frac{\mathcal{G}}{\overline{ER_f\epsilon^T}}\right)^{1/2} - \frac{c_2}{c_1} \tag{19}$$

The length of the debond zone is determined through equation (20).

$$l = \frac{R_f}{2\mu b_1}\ln\left[\frac{\bar{\sigma}_0 - \bar{\sigma}_i + \frac{\varrho a_3 c_3}{b_1}(\bar{\sigma}_0 - \bar{\sigma})}{\bar{\sigma}_0 - \bar{\sigma}}\right] \tag{20}$$

Where $\bar{\sigma}$ is the stress applied to the composite, $\bar{\sigma}_i$ is the stress at which interphase cracking initiates, $\bar{\sigma}_0$ is the maximum value of stress that can be applied to the composite, ϱ is the area fraction of the fibre (R_f/R), and μ is the frictional coefficient associated with fibre sliding. It should be noted that coefficients a_1 through c_3 are determined through the elastic properties of the composite and the boundary conditions imposed upon the debond zone. The work exhibited in this research uses a boundary condition where there is no normal displacement of the matrix material following debonding and assuming that $V_f = V_m$. Derivations for the coefficients may be found in appendix B in Hutchinson & Jenson's paper [1] [47].

Further resistance to pull-out is derived from the initial roughness of the fibre surface [48] [49]. This can be factored into equation (21) by altering the ϵ^T term to include the addition to interfacial clamping due to surface roughness.

$$\epsilon^{T*} = \epsilon^T + {A_{sr}}/{R_f} \tag{21}$$

Where A_{sr} is the amplitude of the fibre surface aspirates. This effect will be reduced to zero if the thickness of the interphase is above an order of magnitude larger than A_{sr} [17].

Designing a proper FMI becomes a challenge of balancing mode II crack growth energy and frictional sliding resistance. Low crack growth energy allows cracks to preferentially initiate within the interphase rather than the fibre. The frictional sliding resistance must be low enough that fibre pullout is enabled; however, a higher sliding resistance is preferred to reduce the size of l, which increases the crack saturation within the matrix phase increasing the overall toughness and strength of the CMC [14].

There are several strategies employed to achieve a low fracture resistance within the FMI. The most common strategy which has exhibited the greatest success is identifying a material with low energy release rate of mode II crack growth. Some of the potential materials include pyrolytic carbon, boron nitride and monazites; these materials preferentially fracture along the (1 0 0) plane due to their crystal structure. The

second strategy is to use a porous FMI; high porosity will greatly decrease the fracture resistance of ceramics. The issue with porous FMIs is that the sliding resistance is often too great to allow the degree of fibre pull-out necessary to produce tough composites with the A_{sr} term of equation (21) increasing to the size of the grainsize of the porous interphase. The third strategy is to use fugitive coatings which are volatized during the ceramic production process. This strategy can produce sufficiently low fracture resistance between the matrix and the fibre provided there is minimal bonding between the two phases. The final strategy is to use a multi-layered coating with sharp interfaces between the coating layers. This strategy requires the maintaining of sharp interfaces upon which cracking preferentially develops through production and during operation conditions. Additionally, the roughness between the cracked interface layers must be controlled to the extent that pull-out can occur [14].

Currently, commercially produced interphases are processed primarily using CVD, although some exploration work has been conducted to examine dip coating or EPD techniques to produce these coatings.

2.2.2.1 Chemical Vapour Deposition

CVD is a deposition process wherein a desired substrate is exposed to reactive chemical precursor gasses at desired conditions and the resultant chemical reaction produces a solid deposit upon the substrate [50]. Typically, the desired conditions are set at a high enough temperature that reaction kinetics will produce a deposit at a reasonable rate while not degrading the substrate [51].

CVD is the favored technique for producing FMI coatings since it is a relatively low temperature operation, it produces thin and even coatings, and is a non-line of sight application process which can infiltrate fibre bundles coating individual fibres. Furthermore, CVD coatings can be produced continuously which makes it a scalable process. Drawbacks to using the CVD coating process include expensive equipment requirements (a lab-scale CVD set-up can cost $500,000 not including costs for incorporating the set-up into existing facilities) and the necessity of working with toxic chemicals such as the CH_3SiCl_3-H_2 mixture (SiC precursors) or the BF_3-NH_3 mixture (BN precursors) [52]. Additionally, there is the requirement that there exists a chemical compatibility of the substrate and the coating material, for example, a carbide fibre cannot be coated with an oxide coating since the carbide fibre would react with the requisite oxygen before the coating is produced. Finally, there is the potential for variability between coating batches due to the complexity of the interaction of the processing variables.

2.2.2.2 Slurry Based Processing

CVD processes employed in the coating of ceramic fibres require hazardous and expensive precursor gasses in addition to expensive equipment. Alternative methods of depositing the FMI have the potential of reducing production costs associated with CMCs while mitigating environmental concerns. These methods

include depositing nano-particle precursors directly upon the fibre out of a nano-particle suspension and EPD.

Dip Coating

Dip coating refers to the process wherein suspended particles within a colloid are adhered to the substrates surface as it is drawn from a colloid bath. The removal of the liquid phase occurs both through draining and evaporation. Draining is governed by the speed at which the substrate is drawn from the bath and the viscosity of the liquid. This creates a force balance between the viscous drag and gravity where the remaining height of the film thickness, h, is given by equation (22).

$$h = c_1 \left(\frac{\eta U_0}{\rho g}\right)^{1/2} \tag{22}$$

Where c_1 is a constant based upon the fluid (roughly 0.8 for Newtonian fluids), U_0 is the rate at which the substrate is drawn from the bath, η is the viscosity, ρ is the liquid density and g is the constant of gravitational acceleration. Additionally, the liquid-vapour surface tension will modulate this equation by $h'=h\gamma^{-1/6}$. Above the stagnation point, at which all liquid content is moving upwards, liquid removal is governed by evaporation. Here the solids mass is conserved provided there are no external forces removing mass content. Evaporation is rate controlled by the ratio of partial pressures, enthalpy of vaporization, and temperature [53].

Electrophoretic Deposition

EPD is a slurry based technique wherein particles are charged and migrated through the slurry by the imposition of an electric field. The technology for EPD has existed since the early 19th century; however, the technique wasn't scientifically studied until Hamaker's work in the 1940's [54]. Although an electrically controlled process, EPD is different from electrolytic deposition processes in that the particles which are to be deposited are already in colloidal solution and are not ions electrically induced by solution. Since the 1980's when EPD's application to the production of thin ceramic layers, the process has been adapted to a large variety of coating media and coating sizes. A summary of the many applications can be found in a review by Besra and Liu [55].

The suspension of the charged particles within the colloid is critical to creating a functional EPD process. A stable colloid is formed through the interaction of Van der Waals attraction, steric repulsion, and double-layer repulsion. The first attempt to study the stability of colloids included only Van der Waals and double layer forces as summarized in the Derjaguin-Landau-Verwey-Overbeek (DVLO) theory [56] [57] [58]. The DVLO theory balances the attraction of Van der Waals forces with the repulsion due to the coulombic

double-layer, if the energy barrier to coagulation is large enough a stable colloid will form. The equations for attractive and repulsive energies are given in equations (23)-(25).

$$W_A = -A_H \frac{R}{12H} \tag{23}$$

$$V_R = 2\pi\varepsilon_r\varepsilon_o a\psi^2 \ln[1 + e^{-\kappa H}] \tag{24}$$

$$\kappa = \left(\frac{{e_0}^2 \sum n_i {z_i}^2}{\varepsilon_r \varepsilon_0 k_B T}\right)^{1/2} \tag{25}$$

Where W_A is the energy of attraction, A_H is the Hamaker constant, H is the shortest distance between the two spheres, R is the particle radius, W_R is the repulsion energy, ε_r is the dielectric constant of the solvent, ε_0 is the dielectric constant of a vacuum, ψ is the surface potential, $1/\kappa$ is the Debye length, e_0 is the charge of an electron, k_B is the Boltzmann constant, T is the absolute temperature, n_i is the concentration of ions with valence z_i [58]. DVLO theory does not take into account several other interparticle forces which may affect EPD, these include attractive ion correlation forces which may occur in more concentrated colloids, manipulation of the lysosphere due to the electric field, and the depletion of hydrogen ions at the cathode affecting local pH [59] [60]. The model proposed by Sarkar and Nicholson [59] [60] which addresses the coagulation effect assumes the lysosphere as a distorted ellipse due to the imposed electric field. In this model the charged particle is surrounded by a lysosphere of oppositely charged ions, the imposed field causes the lysosphere to distort as the particle moves from the centre, creating a thinner side and a thicker side. The thinner side will pose less resistance to the attraction of the particle to the electrode while the thicker side will push the particle towards the same electrode. Once the particle is deposited onto the electrode the lysospheres of adjacent particles will combine coagulating the particles, this process is shown in Figure 8 [59] [61].

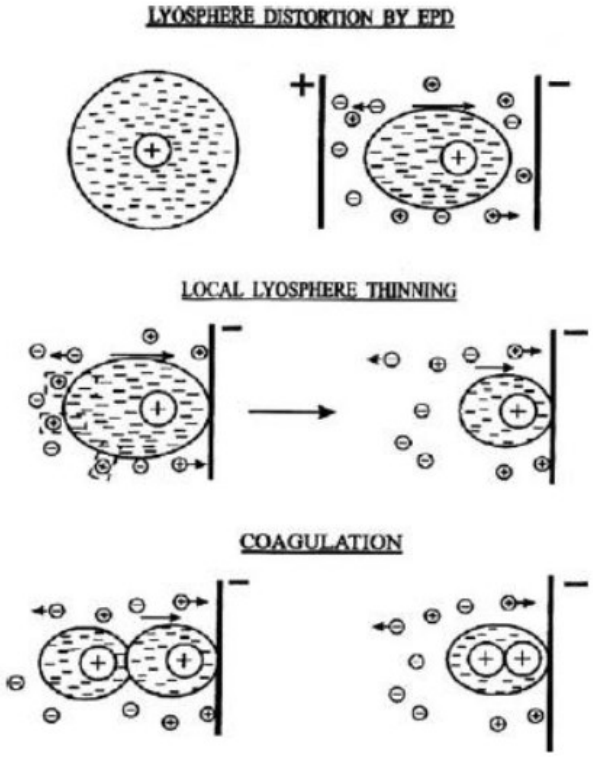

Figure 8: Mechanism for EPD drift due to lysosphere manipulation [61]

Ion depletion at the electrode occurs through the flow of charge carrying ions towards their oppositely charged electrodes, upon reaching the outer Helmholtz plane of the electrode the ions react and become depleted. This results in a concentration gradient of pH with respect to distance from the outer Helmholtz plane which is governed by the drift velocity of the charge carrying ions. The concentration gradient results in a loss of zeta potential of the particles as they reach the deposition electrode which reduces their deposition rate but encourages coagulation [60]. This concentration gradient can be modelled using classic diffusion theory with boundary conditions of $C=C_{bulk}$ *at* $x=\infty$, *and* $J_{c,\ x=0} = -D_{eff}\left(\frac{\partial C}{\partial x}\right)_{x=0}$ where $D_{eff}=D_cD_a(Z_a+Z_c)/(Z_cD_c+Z_aD_a)$. Subscripts c and a denote cations and anions respectively, Z is the valence, J_c is the flux and D is the diffusion coefficient. The concentration can be simplified to

$$C = C_{bulk} - \frac{\lambda}{{D_{eff}}^{1/2}}\left[2\left(\frac{t}{\pi}\right)^{1/2} e^{\left(-\frac{x^2}{4D_{eff}}\right)} - \frac{x}{{D_{eff}}^{1/2}}\left\{1 - \mathrm{erf}\left(\frac{x^2}{4D_{eff}t}\right)^{1/2}\right\}\right] \quad (26)$$

Where $\lambda = I/Z_cF$ (at $x=0$), F is the Faraday constant, I is the current density, and *erf* is the error function [60] [59]. Position x=0 will trend towards a steady state condition with a pH of 7 as the concentration of charge carrying ions at the electrode is depleted. The time it takes for x=0 to reach of pH of 7 is given by equation (27)

$$\tau = \left(\frac{z_c F}{2I} C_{c,bulk}\right)^2 \pi D_{eff} \tag{27}$$

Where z_c and $C_{c,bulk}$ are used if the electrode in question is the cathode, for the anode z_a and $C_{a,bulk}$ will be used. It is important to note that these equations are calculated using the assumption of hydrostatic equilibrium, any naturally arising flow or forced flow of the solvent will alter the relevant concentration gradients. Once the variables in equation (27) are established it is possible to calculate τ and the *pH* gradient at steady-state. Typically, any variation in the pH from the bulk value will occur within distances of less than 100 μm from the electrode [60].

The rate of deposition, as measured by the increase in the mass of the deposited layer over time is given by equations (28)- (29).

$$\frac{dw(t)}{dt} = w_0(1 - e^{-qt}) \tag{28}$$

$$q = \frac{A_{xc} f_d}{V} \frac{\varepsilon_0 \varepsilon_r \zeta}{\eta} (EV - \Delta EV) \tag{29}$$

Where q is the kinetic constant, q*'* is the unit of velocity, h is the height of the deposited layer, A_{xc} is the surface area of the substrate, f_d is the deposition efficiency factor, V is the volume of the suspension, w_0 is the starting weight of the particles in the suspension, ζ is the zeta potential, ε_0 is the permittivity of free space, ε_r is the solvent's dielectric constant, EV is the applied DC voltage and ΔEV is the voltage drop due to shielding by the deposited layer [55] [62]. The shielding effect can be measured through the current density assuming that current is carried through the suspension zone between the two electrodes. This results in equation (30) where I is the current, A_{xc} is still the cross-sectional area of the electrode and k_{sz} is the specific electrical conductivity of the suspension zone.

$$(EV - \Delta EV) = \frac{I}{k_{sz} A_{xc}} \tag{30}$$

The use of constant current rather than constant voltage can ensure that E-ΔE will not vary during the deposit build up. The model represented by equation (28) assumes that the zeta potential remains constant throughout the suspension, that the packing density is close-packed and consistent. To address the variance in zeta potential due to electrochemical reactions the zeta potential function needs to be incorporated as a function of time and distance from the electrode. This can be avoided if the solvent is stirred or agitated during the EPD process. The packing factor assumption is more challenging to address. Packing factor

will be affected by the electrode shape, the particle shape, any agglomeration of particles occurring before deposition, and the formation of gasses due to electrochemical reaction at the electrodes. One method of examining the packing particles is the use of a discrete element modeling code which models and tracks individual particles within the solution. This method examines the level of flocculation which occurs before deposition; the packing becomes much more disordered should flocculation occur prior to deposition [63]. Additionally, this model assumes that the particles are spherical and generally the same size. Recent work by Coelho et al. models the effect of particle shape on the packing density using a model which considers translations and rotations of particles during settling. This work found that an increase of one order of magnitude of aspect ratio can increase the porosity of the particle bed from 40% up to 80% [64]. Additionally, the rate of deposit build up may affect the particle packing if particles are deposited too quickly thereby inhibiting particle settlement into the tightest packing formation [55].

Another interaction to note is the effect of particle shape and solids loading on the rheology of the solution. As seen in equation (28) viscosity of the solution will inversely affect the rate at which the deposit builds.

EPD also enables the deposition of bi-modal particle slurry. This application takes advantage of the different mobilities of particles of different sizes within the solution. Additionally, the difference in surface area to volume ratio of the particles results in different zeta-potentials which can further be used to tailor the deposition ratio of the two particles. Functionally graded materials of WC-Co, ZrO_2-WC and Al_2O_3-PSZ have demonstrated the potential of this process; however, there is still much research which can be conducted within this field [65] [66] [67] [68].

To properly control the quality and thickness of the deposit many parameters must be accounted for or controlled. These include: solvent rheology, solvent polarity, solvent conductivity, cathode and anode shape and conductivity, dispersant additions, binder additions, particle size, particle shape, particle concentration, solution agitation, zeta potential, electrical field strength, electrical field consistency, deposition time, and drying conditions.

Solvent properties, including rheology, polarity, conductivity, and dispersant or binder additions can be tailored to the EPD application to an extent. Water is the most commonly used solvent due to its inherent availability, safety, and environmental considerations. One concern which arises with the use of water as a solvent is electrolysis which can occur at applied voltages as low as 1.23 V. Electrolysis may result in hydrogen or oxygen bubbles becoming trapped within the ceramic coating which leads to defects within the coating. The extent of electrolysis bubble trapping can be controlled through the deposition rate, solvent agitation, and voltage difference. The use of non-aqueous solvents must take into account the lower dielectric constant of non-polar fluids, which results in the requirement of higher voltages.

Sintering of Deposited Coatings

An additional challenge of using particle based deposition techniques is the difficulty of transforming individual deposited ceramic particles into a coherent ceramic layer without further introducing flaws or damaging the fibre phase. Furthermore, any non-ceramic precursors contained within the deposit layer must be removed prior to sintering or incorporated as a useful component of the ceramic layer. This may include any dispersants, binders or sizing used to stabilize the colloid or the deposition layer.

The primary mechanism of sintering is the reduction of surface area through atomic diffusion. The relationship between particle size and sintering rate is given by equation (31).

$$\left(\frac{H}{R}\right)^{א} = \frac{C}{R^{ע}}t \tag{31}$$

Where C is a constant, א has a value between 2 and 6, and $ע$ a value between 2 and 4. The exact values of א and $ע$ will depend upon the rate limiting mechanism. It can be seen that in general as the powder size is reduced the sintering time is also greatly reduced accordingly.

The reduction of surface area and consolidation of ceramic particles will result in a shrinkage of the powder compact dimensions, the rate of which can be related to the rate of sintering through equation (32).

$$-\frac{dL_D}{L_D dt} = \frac{\gamma\Omega}{k_B T}\left(\frac{\Gamma_v D_v}{{G_s}^3} + \frac{\Gamma_{bo} ד D_{bo}}{{G_s}^4}\right) \tag{32}$$

Where γ is the surface energy, Ω is the atomic volume, k_B is the Boltzmann constant, T is the absolute temperature, G_s is the mean grain size, t is the time, L_D is the sample length, D_v and D_{bo} are the coefficients of volume and grain boundary diffusion, ד is the thickness of the grain boundary, and Γ_v and Γ_{bo} are scaling parameters which are related to geometric features [69]. Traditionally sintering is carefully controlled to maximize density without run-off grain growth which weakens the resultant ceramic; however, in the case of the FMI a weak ceramic layer is a benefit, therefore grain growth is less of a concern.

Additionally, differing rates of shrinkage during sintering in the separate layers of the ceramic multilayered FMI will lead to residual stresses and possible delamination between layers, this is a property which is typically considered detrimental; however, in multilayered FMI production it is advantageous [70].

2.2.3 Matrix Fabrication and Associated Deposition Methods

Selection of the matrix will depend upon compatibility of the FMI and the environment of the intended application. The matrix will provide a degree of stiffness and strength to the composite up to the proportional limit. More importantly, the matrix will transfer load between fibre bundles and provide some environmental protection to the FMI and fibres.

2.2.3.1 Chemical Vapour Infiltration

CVI is the term used to describe chemical vapour deposition used to infiltrate a fibre preform and produce the matrix phase. This technique was the original method used to create functional CMC structures in the SNECMA laboratories in France [71]. Advantages of using CVI to create the matrix phase include a matrix phase built up and adhered closely to the fibre structure, little chance of poisoning the FMI, tight control over the matrix microstructure, and the ability to create layered multi-phase matrices. Disadvantages to CVI include long processing times, the need to use machining to re-open the pore networks, residual porosity, expensive equipment, and limited matrix compositions [10].

To determine the rate at which deposition takes place, an estimate must be made for the rate at which gas molecules are impacting the substrate, the reaction energy available at the substrate and the reaction kinetics. The flux of gas particles impacting the surface can be estimated using the Hertz-Knudsen equation (33)

$$F_l = \frac{P}{\sqrt{2\pi M R_G T}} \tag{33}$$

Where F_l is the flux of gas particles, P is the partial pressure of the gas, M is the molar mass of the gas, R_G is the universal gas constant, and T is the absolute temperature. This equation assumes that the gas adheres to ideal gas behavior and the Knudsen law of particle impact. The rate at which the reaction occurs is determined by the Gibbs free energy of the reactants and the products. Gibbs free energy is determined using equation (34), where heat capacity at constant pressure can be estimated by equation (35). Once the Gibbs free energy is determined for each reactant and product the reaction equilibrium constant is determined through equation (36) which gives partial pressure balance (37)

$$\Delta G_f(T) = \Delta \mathcal{H}_f{}^0(298) + \int_{298}^{T} C_p dT - TS^0(298) - \int_{298}^{T} \left(\frac{C_p}{T}\right) dT \tag{34}$$

$$C_p = \mathbb{a} + \mathbb{b}T + \mathbb{c}T^2 + \mathbb{d}T^{-2} \tag{35}$$

$$K_T = \exp\left(-\frac{\Delta G_r}{R_G T}\right) \tag{36}$$

$$K_T = \frac{{p_C}^c {p_D}^d}{{p_A}^a {p_B}^b} \tag{37}$$

Where ΔG is the Gibbs free energy $\Delta\mathcal{H}$ is the enthalpy of formation, C_p is the heat capacity at a constant pressure, S is the standard entropy, T is the absolute temperature, $\mathbb{a}$ through $\mathbb{d}$ are constants, R_G is the universal gas constant, K_T is the reaction constant at temperature T, p is the partial pressure where subscripts and superscripts designate reactants and products in the standard molar equation aA+bB⇔cC+dD where lowercase letters are the mol numbers of the uppercase letters. Standard values and constants for most species which may be used in CVD will be available in many chemistry databases. The solid content precipitated from the product gasses once again depends upon a chemical equilibrium where the Gibbs free energy is minimized. To determine this minimum the mass balance of the total molecular content where mass allocated to solid state is based upon the chemical activity of the condensed phase and the mass balance of the gaseous phase is based upon the partial pressure. This process is repeated for each element in the system creating a linear system of equations. To simplify this process CVD phase diagrams are created using computer programs to handle the math. These diagrams present the ratios of reactants to products at set temperatures and pressures. It should be noted that more than one reaction may be occurring in the chamber, the reaction with the lowest Gibbs free energy will be favoured, the energy difference will determine how dominant it is. Furthermore, these calculations are based upon many assumptions which may not prove to be correct, they will not provide quantitative predictions but can be used to design the CVD process [50].

CVD processes typically use either halides, hydrides or metal-organic compounds. These halides and hydrides are preferred because they are small molecules with a high electronegative component which makes the gas and reaction kinetics easy to predict. Metal-organic compounds are used in a highly specialized CVD process which produces more complex structures.

There are a few variations on the CVD process of interest to the production of CMCs. The first variation is cold wall reactors vs. hot wall reactors. Cold wall reactors use an energy source to heat the substrate itself, this may be microwave energy [72] [73], induction heating or resistive heating. Cold wall reactors reduce the energy requirements for CVD and prevent products from forming on the chamber walls. Continuous fibre coating CVD chambers are another CVD adaption for the CMC industry. In continuous fibre coating CVD, the fibre tow is pulled through the reaction chamber at a rate determined to keep the fibre in the chamber long enough to form a thick enough interphase. This process presents many challenges to ensure that as the fibre enters and exits the reaction chamber no contaminants are introduced and the vacuum is maintained [50].

2.2.3.2 Polymer Infiltration and Pyrolysis

PIP uses the same principles as seen in the conversion of polymer precursors to ceramic fibres [74] [75]. Polycarbosilane (PCS) is the polymer most often used as SiC precursor, the pre-treatment or curing step is used to break Si-H and C-H bonds in order to bond Si-C and C-C to form the basis of the SiC ceramic. Originally this was achieved by heating the precursor in oxygen at 190+ °C to volatize the SiH and CH_3 sidechains and create amorphous Si-C-O which is later converted into ß-SiC in the pyrolysis stage [9]. This process produces a higher density matrix with a fine grain structure; however, due to the loss of volume of the polymer during pyrolysis, infiltration must be repeated several times to achieve high density; typical PIP processes recommend 7-9 infiltration cycles. Similar to the mechanisms behind crack formation in the drying of thin films, tensile stresses form in the unconstrained surface of the polymer during the volume loss process resulting in microcracking throughout the matrix. Selecting the polymer which will be infiltrated to form the matrix depends upon the chemical structure of the matrix which is desired. Similar to the fabrication of carbide fibres, the chemical make-up of the polymer chains will determine the ceramic which is formed. As with any infiltration process, the flux of the polymer into the preform is critical; additionally, the escape of the gaseous by-products during pyrolysis must be ensured to prevent the entrapment of pores.

2.2.3.3 Reactive Melt Infiltration

RMI is the process wherein the ceramic matrix is produced in two steps. The first step utilizes a carbon precursor that is infiltrated into the fibre preform and pyrolyzed into a porous carbon. The second step involves infiltrating the porous carbon with a liquid metal, upon contact the metal and carbon react to form a carbide ceramic. RMI is an attractive method for producing ceramic matrices due to the minimal volume change during reaction and the reduction in infiltration steps as compared to CVI and PIP processes. The primary drawback of the RMI is the likelihood that unreacted phases will remain present within the matrix at the conclusion of infiltration. These pockets of unreacted precursors have the potential to reduce the properties of the matrix, especially at operating temperatures.

An ideal melt infiltration process must achieve full infiltration and reaction without altering the preform shape or creating residual tensile stresses, this is nearly impossible to achieve in reality. However, through the careful selection of precursors and controlling of processing steps a near ideal matrix can be produced. Initially the desired matrix must be identified; this will dictate the metal which will be used for infiltration and the composition of the precursor. Metallic properties which affect the liquid metal infiltration process include melting point, as well as the viscosity and molar volume of the liquid phase. The carbon precursor is selected for its ability to form porous carbon with a well-connected uniform pore network. The carbon precursor must also be capable of infiltrating the fibre preform without damaging the FMI. Therefore,

properties which must be considered when selecting the carbon precursor include viscosity, carbon yield, bulk density, pore structure of the char, and reactivity of the char. To achieve these desired properties in a carbon precursor an accepted technique involves mixing two or more carbon precursors with a range of properties to achieve an optimized porous carbon. Finally, the fibre preform will also introduce properties which must be considered. These include fibre weave architecture, preform shape, any prior particle infiltration steps, and reactivity of the FMI to the infiltrated reactants.

Carbon precursors are organic compounds which are converted to carbon through pyrolysis. There are many organic compounds which can serve as carbon precursors; however, when accounting for desired properties several candidates appear to be the most ideal. These include resins containing aromatic carbon chains, typically phenol or furan [76] [77], and crystalline cellulose [78] [79]. Additionally the organic nature of most binding agents can be utilized to produce some carbon content [11]. Prior to pyrolyzation it may be necessary to heat treat the precursor to stabilize its structure. This process is similar in reaction mechanics to the mesophase forming treatment during carbon fibre production. Phenolic and furoic resins produce porous carbon with low reactivity and a closed pore network since they undergo densification during pyrolyzation similar to a sintering process and the carbon atoms tend to be tied up in sp^2 bonds [79]. Crystalline cellulose precursors exhibit much lower densification and much higher reactivity. This is due to the lack of aromatic content resulting in highly amorphous carbon with much greater specific surface area.

Infiltration proceeds through capillary mechanics as the liquid metal penetrates the porous preform. The diameter of the capillaries and the viscosity of the metal will limit the speed at which the metal infiltrates the preform according to the equation (38) [80].

$$h^2 = \gamma_{lv} \frac{cos\theta}{2\eta} Rt \tag{38}$$

Where h is the depth of infiltration, γ_{lv} is the surface tension of the liquid, η is the viscosity of the melt, θ is the contact angle of the melt on the solid, R is the effective pore radius and t is the time. As the liquid metal infiltrates, the preform reaction along the capillary wall will occur on a much smaller timescale than the infiltration rate, essentially instantaneously. The diameter of the capillaries will be altered by the ratio of the relative molar volumes of the reactants and products as seen in equation (39).

$$d_c{}' = d_c{}^0 - 2\sqrt{2D_e \frac{M_A}{M_B}\frac{\rho_B}{\rho_A} t}\left(1 - \frac{1}{MV_R}\right) \tag{39}$$

Where d_c is the diameter of the capillary, D_e is the binary diffusion coefficient of reactant B within reactant A, M is the molar mass of the specified reactant, ρ is the density of the specified reactant, t is time, and

MV_R is the molar volume coefficient of the product. As the infiltration proceeds reaction within the preform becomes rate controlled by the diffusion of the carbon particles through the newly produced ceramic which significantly reduces the reaction rate [81] [82]. Ideal pore volume is determined through d_c^0-d_c'→0.

$$\rho_{ideal} = {}^{M_C}/_{MV_{SiC}} \tag{40}$$

Where ρ_{ideal} is the ideal bulk density of the porous carbon preform, M_C is the molar mass of carbon and V_{SiC} is the molar volume of SiC. Ideally the carbon preform approaches ρ_{ideal} while maintaining a majority of pore radii near $d_{c\,,ideal}^{\,0}$.

2.3 Design of Experiment

Since the pioneering work of R.A. Fischer in the 1930's design of experiments (DoE) has become an increasingly developed and defined approach to experimentation [83]. This is due to two features which arise from the careful DoE: a great reduction in the number of experimental trials which must be conducted to establish meaningful results, and the ability to examine the contributions of variables to the response surface behavior and additionally the interactions between separate input variables upon the response surface behavior.

2.3.1 Factorial Design of Experiment

To properly examine the principles of factorial DoE it is important to establish some terminology. In DoE the input variables are called factors, the set points for each factor are known as a levels. An experimental trial with each factor set to a level is known as a treatment combination which will be represented by the symbol T_r in this work. The difference in the experimental response between two treatment combinations is known as a treatment contrast. The influence of a single factor on the response of the experiment is known as a main effect whereas the influence of the combination of two or more factors on the experimental response is known as an interaction effect. A full factorial design is an experimental setup which consists of enough treatment combinations to determine every main effect and every interaction effect. The number of runs necessary to create a full factorial experimental design is given by $\Pi_{i=1}^{n} s_i$ where n is the number of factors and s is the level of these factors. Full factorial designs are given the notation: s^n factorial designs. Adding additional factors or increasing the levels for one or more factors will increase the number of experimental runs by an exponential amount. Therefore, a more common approach is to use a fractional factorial design. Fractional factorial designs reduce the number of experimental runs by aliasing higher order interaction effects with additional factors. Fractional factorial designs are given the notation s^{n-k}, where k is the fraction which is determined by the desired number of treatment combinations given the number of factors being examined.

Treatment contrasts are the heart of the factorial DoE process and the key to proper minimum aberration design because they allow one to measure main effects and interaction effects. The generalized form of treatment contrasts is given by equation (41)

$$L(F_{q_1} \dots F_{q_r}) = \sum_{j_1=0}^{s_1-1} \sum_{j_n=0}^{s_n-1} l(g_q \dots g_{q_r})\, \tau(j_1 \dots j_n) \tag{41}$$

Where F is the factorial effect being examined, s is the level of factor n, j and g are tuples of n and q_r elements which specify the effect being examined by the treatment contrast, l is a coefficient array specified by the g-tuple, and τ is the treatment effect corresponding to each j-tuple. The q index of factorial effect F holds to the relation ($1 \leq q_1 < \dots < q_r \leq n$; $1 \leq r \leq n$); r is determined by the order of the effect being examined, for example a main effect will have an r value of 1, a 3 factor interaction will have an r value of 3. The g-tuple is given by the $q_1 \dots q_r$ elements of the j-tuple, for example an F_1F_3 interaction effect results in g-tuples specified by j_1j_3 elements of the j-tuple. The elements of the coefficient array l must sum to 0, in the special case of a symmetrical factorial design with s=2 then the values of l are $1/2^{(n-1)}$. To clarify these definitions further the example of a symmetrical two factor two level factorial is provided.

In a 2^2 factorial (s=2, n=2) the full list of treatment combinations is specified by the following j-tuples: 00, 01, 10, 11. The treatment contrasts to determine the effect of factor are given below:

$$L(F_1) = \frac{1}{2}[\{\tau(10) - \tau(00)\} + \{\tau(11) - (01)\}] \tag{42a}$$

$$L(F_1) = -\frac{1}{2}\{\tau(00) + \tau(01)\} + \frac{1}{2}\{\tau(11) + \tau(01)\}$$

r = 1, g = 1, 0; l = -1/2, 1/2

$$L(F_2) = \frac{1}{2}[\{\tau(01) - \tau(00)\} + \{\tau(11) - (10)\}] \tag{42b}$$

$$L(F_2) = -\frac{1}{2}\{\tau(00) + \tau(10)\} + \frac{1}{2}\{\tau(11) + \tau(10)\}$$

r = 1, g = 1, 0; l = 1/2, -1/2

$$L(F_1F_2) = \frac{1}{2}[\{\tau(11) - \tau(01)\} + \{\tau(10) - (00)\}] \tag{42c}$$

$$L(F_1F_2) = -\frac{1}{2}\{\tau(01) + \tau(10)\} + \frac{1}{2}\{\tau(11) + \tau(00)\}$$

r = 2, g =11, 00, 01, 10; l = 1/2, 1/2, -1/2, -1/2

Equation (41) may also be expressed as equation (43) to allow for the incorporation of Galois field theory and defining pencils which is useful for the identification of fractional factorial design matrices

$$L = \sum_{j=0}^{s-1} l_j \left\{ \sum_{x \in V_j(b)} \tau(x) \right\} \tag{43}$$

$$V_j(b) = \left\{ x = (x_1, \dots, x_n)' : b'x = \alpha_j \right\} 0 \le j \le s-1 \tag{44}$$

Where L is the treatment contrast, s is the level of the factors, j is an index indicating the effect being examined, l is a coefficient array that sums to 0, $V_j(b)$ is given by equation (44), x is a vector of treatment combinations, b is a fixed nonnull vector of size 1 x n -1 over Galois Field Space GF(s) and α_j is a vector consisting of the elements of the Galois Field of order GF(s). A Galois Field, GF(s), is defined as a finite set of integers {0,1,…,s-1} which utilizes modulo s addition and multiplication. A GF(3) consists of elements {0,1,2} and 2^1 in GF(3) is equivalent to 2 whereas 2^2 in GF(3) is equivalent to 1. For the Galois Field space GF(s), there are $(s^n-1)/(s-1)$ distinct pencils that can be specified which is equivalent to the number of distinct factorial effects in symmetric factorials, presenting the result that for each factorial effect there is a distinct pencil b which specifies the treatment contrast. Where the term pencil describes a vector which can exist within the specified Galois field space, for example in a two factor, two level DoE system vectors (0 0), (0 1), (1 0), (1 1) are all distinct pencils which exist; in a six factor, three level DoE two such pencils are (0 1 2 1 0 1) or (0 0 0 0 0 1).

Fractional factorial designs given by s^{n-k} are specified by k linearly independent pencils b^1, ... ,b^k, and contains x treatment combinations which are specified by the relation Bx = c where B is a k x n matrix and c is a k x 1 fixed vector. For simplicity's sake c is often defined as a null vector creating the relation Bx = 0. The row space of B provides the defining relation of the fractional design. The defining relation is often given in compact notation and provides information on the aliasing structure of the fractional factorial design. An example of a 2^{5-2} design is given to clarify these concepts. A 2^{5-2} fractional design consists of $2^5/2^2 = 8$ treatment combinations with 5 factors at two levels. One defining relation which can produce a 2^{5-2} design is

$$B = \begin{bmatrix} 1 & 1 & 0 & 1 & 0 \\ 1 & 0 & 1 & 0 & 1 \end{bmatrix} \tag{45}$$

Where b^1=[1 1 0 1 0] and b^2 = [1 0 1 0 1] which can be expressed in compact notation as b^1 = 124 and b^2 = 134. Using Bx = 0 we can get the following system of equations

$$x_1 + x_2 + x_4 = 0 \tag{46}$$

$$x_1 + x_3 + x_5 = 0$$

Examining all possibilities of x which can satisfy (46) results in treatment combinations x = [0,0,0,0,0], [0,0,1,0,1], [0,1,0,1,0], [0,1,1,1,1], [1,0,0,1,1], [1,0,1,1,0], [1,1,0,0,1], [1,1,1,0,1]. It can be shown that the same result is achieved if either b^1 or b^2 = [0,1,1,1,1]. Therefore, the defining relation of the 2^{5-2} design specified by (45) is 124 = 135 = 2345. It can also be seen that using compact notation and maintaining modulo 2 multiplication that 124 x 135 = 2345 which provides a simpler approach to determining complete defining relation. The terminology of *codeword* has been borrowed from algebraic coding theory to label the defining relations when presented in compact notation and the number of elements in each codeword is known as the wordlength. Wordlength is used to determine the strength of the defining relation, a stronger defining relation results in less information being lost due to aliasing of the effects. The strength of a defining relation is also known as the resolution of the design which is determined by the shortest codeword in the defining relation. The resolution of the design is given as a roman numeral and will typically fall between III and V, where a III resolution design aliases two or greater factor interactions with the main effect of the additional factors and IV resolution designs alias three or greater factor interactions with the main effect of the additional factors. The resolution of the design matrix is equal to the number of elements in shortest codeword in the defining relation. Minimum aberration design is a codeword based approach to selecting defining relations for fractional factorial DoE. Minimum aberration design dictates that for any two designs of an equal resolution, the defining relation with the greatest sum of wordlengths will produce the stronger design matrix.

Defining relations and codewords can also be used to determine which factorial effects are being aliased by the additional factors being incorporated into the fractional design. In the 2^{5-2} example shown previously the defining relation is given as I =124 = 135 = 2345 resulting in a resolution III design. The F_1 main effect may be given in codeword form as 1, multiplying 1 by each codeword in the defining relation results in the relation 1(I) = 124(1) = 135(1) = 2345(1) → 1 = 24 = 45 = 12345. This shows that the main effect F_1 is aliased by interaction effects F_2F_4, F_4F_5, and $F_1F_2F_3F_4F_5$. Performing the same operation with codewords 4 and 5 results in the aliasing structures of 4 = 12 = 1345 = 235 and 5 = 1245 = 13 = 234. The results of 12 = 4 and 13 = 5 are of interest for demonstrating the mechanics of aliasing using the design matrix shown below.

$$M = \begin{bmatrix} 0 & 0 & 0 & 0 & 0 \\ 0 & 0 & 1 & 0 & 1 \\ 0 & 1 & 0 & 1 & 0 \\ 0 & 1 & 1 & 1 & 1 \\ 1 & 0 & 0 & 1 & 1 \\ 1 & 0 & 1 & 1 & 0 \\ 1 & 1 & 0 & 0 & 1 \\ 1 & 1 & 1 & 0 & 0 \end{bmatrix} \quad (47)$$

It can be seen that column 4 is the modulo 2 addition of column 1 and 2 and column 5 is the modulo addition of column 1 and 3. In other words when columns 1 and 2 have the values 0 and 1 or 1 and 0 then column 4 will have the value of 1 whereas when columns 1 and 2 have the values of 1 and 1 or 0 and 0 then column 4 will have the value of 0 likewise, for columns 1 and 3 vs. column 5. Recalling from equation (41) that the *g*-tuple specifies the coefficient array *l* in treatment contrasts and that the values of *g* for the main effect for columns 4 and 5 are essentially the same as the *g* -tuple for the interact effects of F_1F_2 and F_1F_3 respectively the aliasing caused by the fractional factorial becomes apparent [84] [85] [86].

2.4 Multiphysics-based Computational Modeling

Multiphysics-based computational modeling is based upon the principles of finite element analysis. The 'multiphysics' aspect is achieved by coupling the governing partial differential equations/ordinary differential equations (PDEs/ODEs) for different physical phenomena being examined in the model. The work undertaken in this thesis relies upon the commercially available multiphysics modeling platform COMSOL Multiphysics®. Structurally, COMSOL consists of a baseline application and separate modules which include the physics interfaces used to specify disparate physical phenomenon including their governing physics equations and associated boundary conditions. The baseline application includes a graphical user interface, the ability to specify geometries, an automated meshing tool, a limited material properties database, advanced solvers, and the ability for the user to input their own PDE/ODEs. Modules with relevance to this work include AC/DC module, Heat Transfer module, Structural Mechanics module, and an enhanced materials database. [87]

Creating a multiphysics model in COMSOL follows a straightforward workflow. A new project is initiated by determining which dimensional space the model will be simulated in (3D, 2D-axis symmetric, 2D, 1D), which physics module to include (heat flow, AC/DC, statics, etc.) and which type of study will by utilized (stationary, time dependant, frequency domain, etc.). Once these options are determined the next step is to define the geometry of the model. A model's geometry creates domains, boundaries, edges, and vertices which are 3D, 2D, 1D, and 0D objects respectively. Once the geometry has been established it is good practice to create definitions, these are groupings of domains, boundaries, etc. which enable the quick selection of specific geometries as physics and meshes are added to the model. The next step in the process

is assigning materials to the domains which have been created. Materials assign physical properties to domains such as Poisson's ratio, dielectric constant, and coefficient of thermal expansion. These properties can be assigned either as constants or as equations which vary with other physical properties, for example, the coefficient of thermal expansion will vary with temperature. Material properties can either be assigned based on values contained within COMSOL's material database or by the user generating the model. Following the assignation of materials, the physics interface is used to assign initial conditions and boundary conditions. The next step in the process is to create the mesh. It is possible to rely on the automated COMSOL meshing feature to create a physics driven mesh. With this option, the only user input requirement is a selection of a general size category where a fine mesh will have a greater resolution than a coarse mesh at the expense of a greater computing load. It is also possible to specify specific meshes to specific geometries. Once the mesh is defined the model can be simulated based upon the study which was specified at the beginning of the process. COMSOL will utilize optimized solvers based upon the physics being simulated and the hardware the simulation is being run on. Once a solution has been converged upon the results interface allows for control over the interpretation and graphical display of results that have been generated.

3. Methodology

Undertaking the design of a novel production technique for multi-layered FMI coatings requires a systemic approach. An appropriate factorial DoE setup has been established to examine a large design space of variables contributing to the deposition of fibre coatings.

3.1 Materials

The fabrication of CMCs requires considerable material selection for each component of the composite: the fibre, FMI, matrix, and in certain applications the environmental barrier coating. Additionally, materials utilized in the fabrication process must also be carefully selected.

Initially a variety of ceramic fibres were procured for this work from two commercial ceramic fibre vendors: COI Ceramics (Hi-Nicalon™, Sylramic™) and UBE Industries (Tyranno™). Additionally, a reel of SCS-6 single filament silicon carbide fibre by Specialty Materials, Inc. was found from a previous research project. Materials properties of Hi-Nicalon, Sylramic, Tyranno and SCS-6 can be found in Section 2.1.3, and a brief summary of the most relevant properties can be found in Table 3. To reduce the potential variability, it was decided, after some initial EPD coating experiments, to work entirely with Hi-Nicalon™ for fabricating microcomposites for this research.

Table 3: Fibres and Select Properties

Fibre	Producer	Filament Diameter (μm)	Tow Count	Characteristic Strength (GPa)	Characteristic Modulus (GPa)
SCS-6	Specialty Materials Inc.	140	1	6	390
Hi-Nicalon	COI Ceramics	14	500	2.8	270
Sylramic	COI Ceramics	10	800	3.2	400
Tyranno	UBE Inc.	11	800	3.3	187

For EPD, the properties of the FMI depend upon the ceramic powder to form the interphase as well as the additives used to control the colloidal properties during deposition. The powders used for the FMI were procured from MK-Nano and are listed in Table 4.

Table 4: Powders Selected for FMI

Commercial Name	Composition	Average Particle Size*
MKN-SiCb-040	β-SiC	40 nm
MKN-Si3N4-020	Si_3N_4	20 nm
MKN-ZrC-050	ZrC	50 nm
MKN-hBN-N70	Hexagonal BN	70 nm
MKN-Al2O3-A100	α-Al_2O_3	100 nm
MKN-3YSZ-040	ZrO_2(3%Y_2O_3)	40 nm

*Average particle size was characterized and reported by the vendor

Polyvinyl alcohol (PVA) was obtained (Sigma Aldrich, 363146) to act as a binder for the ceramic particles deposited during EPD. Agents for modifying the zeta potential include Cetrimonium bromide (CTAB) (Sigma Aldrich, H5882) and dextrin, a polysaccharide with the chemical formula $(C_6H_{10}O_5)_n$ (Sigma Aldrich, D2006-500G) combined with HCl [88].

For the purpose of this thesis a RMI process was selected as the route for matrix production. As covered in section 2.2.3.3 RMI requires a polymer-based precursor which is pyrolyzed into porous carbon prior to the infiltration of a liquid metal phase. The phenolic resin (Durez 34237, SBHPP) was selected for its high char retention. Microcrystalline cellulose was sourced from Sigma Aldrich (C8002). For the liquid metal addition 99.99% pure silicon was purchased from Stanford Advanced Materials in shaved pellet form (shown in Figure 9).

Figure 9: Shaved silicon pellets with micrometer to provide an indication of pellet size

3.2 Multi-Layered FMI

Several variations of multi-layered FMIs are to be examined in this work to explore their potential for fibre debond and to act as an environmental protection barrier for the fibre phase. The different FMI coating compositions are given in Table 5.

Table 5: Coating Labels and component of each layer in the coating composition

Coating	Layer 1	Layer 2	Layer 3
SiC/Al_2O_3	MKN-SiCb-040	MKN-Al2O3-A100	
BN/PSZ	MKN-hBN-N70	MKN-3YSZ-040	
ZrC/ZTA	MKN-ZrC-050	85wt%MKN-Al2O3-A100 + 15wt%MKN-3YSZ-040	
SiC/Si_3N_4/SiC	MKN-SiCb-040	MKN-Si3N4-020	MKN-SiCb-040

Coatings are labelled following the convention that the inner layers, that is the layer closest to the fibre, appears first in the name. Traditionally, fibre-matrix interphase compositions utilize ceramics with a hexagonal crystal structure ensure with weak internal bonding across the basal planes to ensure the low

fracture energy failure criteria is achieved [14]. In this work several ceramics are selected, for example Al_2O_3, which do not possess this hexagonal crystal structure. It is hypothesized that the combination of internal stresses generated during processing and constrained sintering conditions will lead to the fabrication of a weakened ceramic structure in the FMI.

3.3 Stationary Electrodeposition of Multilayer FMIs

To examine the feasibility of producing a fibre coating using EPD, a lab-scale test cell was fabricated in this research to coat small sections of ceramic fibres. This lab scale setup has been designated as the stationary EPD coating cell because the fibre bundle remains stationary in reference to the outer electrode. An early version of the setup is shown in Figure 10 which highlights the main components.

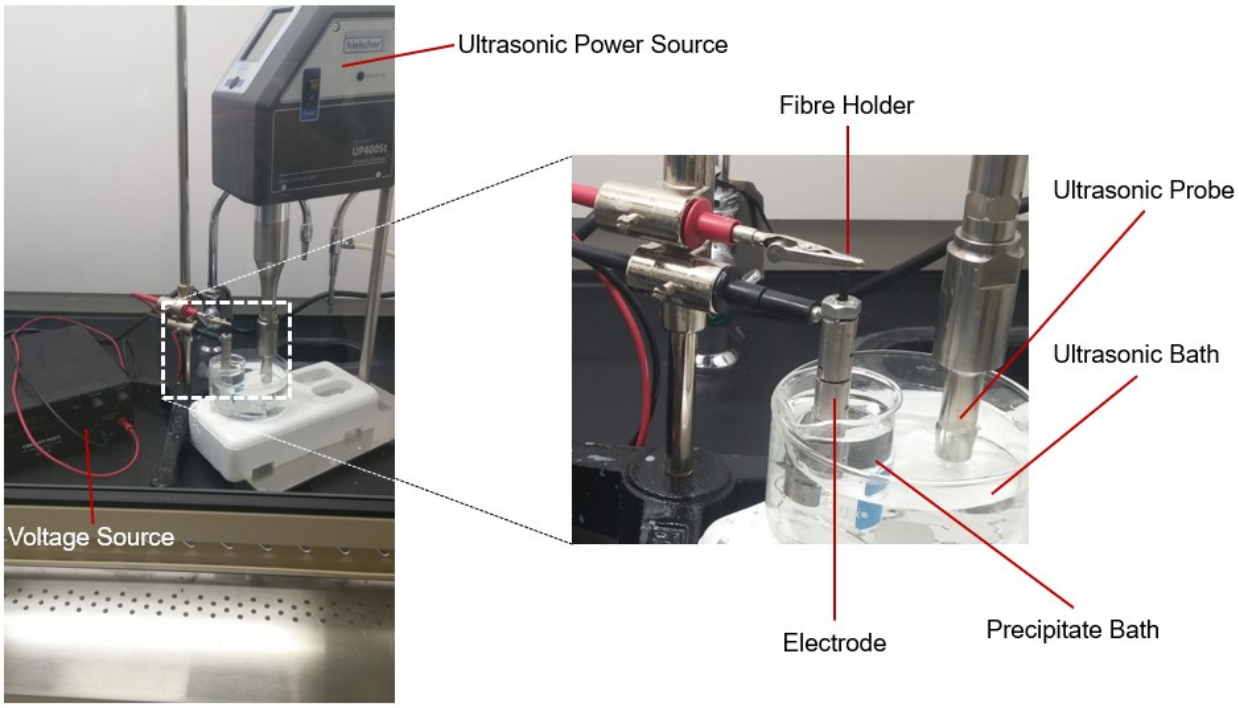

Figure 10: Stationary EPD Cell

The components of the stationary include the voltage source (PSC-6600, Circuit Test), the electrode (Inner Diameter 1/8 in, Outer Diamter 1/4 in, 410 Stainless Steel), the fibre holder (standard alligator clip), the precipitate bath where the colloid is held for the deposition process (40 mL volume), an ultrasonic agitation system to prevent agglomeration in the colloid (UP400St, Hielscher USA) with a Sonotrode s24d3 (Hielscher USA) ultrasonic probe. The polarity of the electrode and fibre holder can be reversed at the voltage source depending upon the expected charge of the colloid particles. Modifications to the setup include the replacement of the initial ultrasonicator probe with the s24d3 version which is more suited the

volumes encountered in this work, and the addition of a Teflon shield within the outer electrode to prevent accidental contact between the inner and outer electrode.

3.3.1 Zeta Potential of Ceramic Particles within Colloid

To determine the Zeta Potential of the charged particles within the slurry, a Litesizer™ 500 (Anton Paar), equipped with Kalliope analysis software, and Omega cuvettes were utilized. The Litesizer™ is a dynamic light scattering (DLS) based particle sizing system wherein a 658 nm 40 mW laser is projected through the colloid sample. As the laser beam interacts with particles suspended within the colloid it is scattered forming an interference speckle pattern which is detected using a photomultiplier. The intensity of the speckle pattern varies as the particles undergo Brownian motion within the solvent, the varying intensity is correlated to the speed of the particles which is then correlated to the particle size. For the determination of zeta potential electrophoretic light scattering (ELS) is utilized. Electrophoretic light scattering operates under a similar principle to dynamic light scattering except the particle movement is driven by an imposed alternating electric field rather than random Brownian motion and the speed of the particles is measured by examining the Doppler shift of the laser light as it interacts with the moving particles. Typically, the Doppler shift is measured using a technique known as phase-analysis light scattering (PALS) where the laser is split into a sample beam and a modulated reference beam. The modulator vibrates at a specified frequency determined by a mathematically generated sine wave which can be compared to the scattered beam. This technique allows for the detection of smaller particle movements which reduces the magnitude of the electric field required to generate particle movement. The Litesizer™ uses a modified version of PALS known as continuous monitored PALS (cmPALS) where an additional un-modulated reference beam is compared to the modulated beam to detect any non-linearity or change in the modulator characteristics [89] [90].

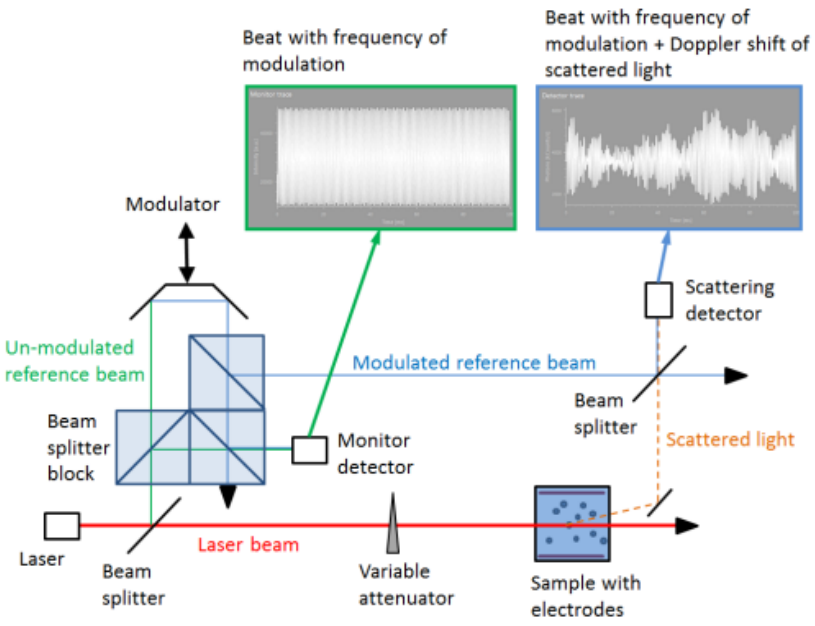

Figure 11: Diagram illustrating the setup of the continuously monitoring phase analysis light scattering system within the Litesizer™ [90]

For zeta potential measurements a minimal powder load (> 300 mg) is added to the solvent and agitated using the ultrasonic agitator (UP400St, Hielscher USA) for 30 seconds then slowly pipetted into an Omega style cuvette avoiding the formation of bubbles within the cuvette.

Figure 12: Omega style cuvette

3.3.2 Factorial Design of Experiments for Stationary EPD Trials

To assess the effectiveness of EPD for producing multi-layered FMIs this work has identified six primary factors of interest. These factors are: Electric Field Strength, Electric Field Duration, Surfactant, Solids Loading, and Binder Usage. The factors and their low and high level settings are presented in Table 6.

Table 6: Stationary Electrodeposition factors and their level settings

Factor	Low Level	High Level
Electric Field	50 V/cm	100 V/cm
Duration	30 seconds	60 seconds
Surfactant	CTAB	Dextrin + HCl
Solids Loading	4wt%	8wt%
Binder usage	None	4% PVA

Electric field is determined by dividing the overall voltage of the power supply by the inner radius of the electrode. The CTAB mixture is produced by adding 0.4wt% CTAB powder to the solute then magnetically stirring the solution for 24 hours. The dextrin+HCl mixture is produced by adding 0.4wt% dextrin powder to the solute then reducing the pH of the solute to 2 by adding HCl then magnetically stirring the solution for 24 hours. The 4% PVA mixture is produced by adding PVA crystals to distilled water then increasing the temperature of the mixture to greater than 90 °C and stirring until the crystals are completely dissolved.

Initially, the system response of primary concern was the debond energy of the deposited FMI; however, during tensile testing of the microcomposite samples it became apparent that the significant variation observed in the tensile properties of the microcomposites due to variability in the tensile properties of the matrix. This variability rendered the determination of the debond energy system response statistically futile. As a result, tensile strength and FMI thickness were examined. The procedure for determining these properties is covered in Section 3.5 and 3.6. A 2^{5-2} factorial design such as the example given in section 2.3.1 balances the number of trials and the number of factors. The design matrix is presented in Table 7, where 0 represents a low level setting and 1 represents a high level setting. Two batches of samples were manufactured according to this DoE, Batch 2 consisting of twelve samples which were tested at room temperature and batch 3 consisting of six samples which were tested at room temperature following exposure to a high temperature oxygen bearing atmosphere.

Table 7: Design Matrix for Stationary EPD of Multi-layered FMIs

Trial Run	Electric Field	Duration	Surfactant	Solids Loading	Binder Usage
1	0	0	0	0	0
2	0	0	1	0	1
3	0	1	0	1	0
4	0	1	1	1	1
5	1	0	0	1	1
6	1	0	1	1	0
7	1	1	0	0	1
8	1	1	1	0	0

Following the tensile results from the high temperature exposure testing, another batch of microcomposites were fabricated using only coating compositions of BN/PSZ and SiC/Si_3N_4/SiC. For these microcomposites a 3^2 full factorial design was utilized to examine the effects of deposition time and voltage (Table 8). The colloid conditions included using CTAB as the zeta potential causing agent, no binder and 4wt% solids loading. Thirteen microcomposites and one coated fibre bundles per trial run and coating type (a total of 252 fibre bundles) were fabricated. From the microcomposites in this batch six microcomposites were reserved for room temperature testing, and six microcomposites were reserved for high temperature testing, and one microcomposite sample was reserved for future possible testing such as mass change in oxidizing atmospheres measured through thermogravimetric analysis.

Table 8: 3^2 full factorial design examining deposition time and voltage for high temperature microcomposite testing

Trial	Deposition Time (s)	Voltage (V)
1	30	12.5
2	75	12.5
3	120	12.5
4	30	32.25
5	75	32.25
6	120	32.25
7	30	50
8	75	50

9	120	50

3.4 Reactive Melt Infiltration Fabrication of the Matrix Phase

A RMI approach to matrix fabrication was selected based upon results from the literature review and the equipment and consumables available for this work. The three primary components for creating the pre-carbon resin mixture are the phenolic resin, crystalline cellulose and SiC powder.

As covered in section 2.2.3.3, RMI is conducted in three thermally activated steps: resin stabilization, resin pyrolysis and liquid metal infiltration. The thermal treatments are based upon the schedule given in Margiotta's work [91]. The actual thermal schedule using in this study for each of the three steps is outlined in Table 9, Table 10, and Table 11.

Table 9: Thermal Treatment for Pre-Carbon Resin Stabilization

Step	Treatment	Duration (h)
1	Ramp to 300 °C	1
2	Soak at 300 °C	5
5	Ramp to Room Temperature	1

Table 10: Thermal Treatment for Pre-Carbon Resin Pyrolysis

Step	Treatment	Duration (h)
1	Ramp to 250 °C	4
2	Ramp to 375 °C	4
3	Ramp to 1000 °C	7
4	Soak at 1000 °C	2
5	Ramp to Room Temperature	7

Table 11: Thermal Treatment for Porous Carbon Liquid Metal Infiltration

Step	Treatment	Duration (h)
1	Ramp to 1445 °C	4.8
2	Soak at 1445 °C	4
3	Ramp to Room Temperature	4.8

3.5 Experimental Methods for Evaluating FMI

3.5.1 Fabrication of Microcomposite Samples for Interphase Evaluation

Microcomposite samples are produced using a single fibre tow with the interphase coating conditions depending upon the manufacturing batch (Table 12). Batch 1 consisted entirely of fibre bundles to conduct a preliminary examination of the EPD process prior to proceeding with microcomposite fabrication. For batches 2-5, following the EPD application of the interphase coatings the samples are infiltrated with a resin system consisting of 76.5wt% phenolic resin, 8.5wt% micro cellulose, and 15wt% SiC nanopowder pre-carbon resin system. The samples are then heat treated, pyrolyzed and silicized according to the procedure outlined in section 3.4.

Table 12: Fibre bundle and microcomposite batches manufactured

Batch No.	Interphase Coating Conditions	Purpose	Samples Produced	Notes
Batch 1	N/A	Preliminary Examination of EPD process	60	Used Sylramic, Tyranno, SCS, and Hi-Nic fibre
Batch 2	(Table 7) See 3.3.2	RT Tensile Testing	384	
Batch 3	(Table 7) See 3.3.2	RT Tensile Testing following 1000 °C Exposure	192	
Batch 4	(Table 8) See 3.3.2	HT Tensile Testing	252	Microcomposite samples were destroyed during silicization due to furnace over-temp
Batch 5	(Table 8) See 3.3.2	HT Tensile Testing	216	

Following processing, microcomposite cross sections were hand polished with a progression of 120, 200 and 400 grit sandpaper to reduce outlying geometrical features. Samples are then scanned using a 3D scanner (Shapegrabber AI310) to determine their cross-sectional areas. The laser scanner has a resolution of 0.0254 mm. Samples were inserted vertically in a small reservoir of plasticine to secure them while the scanning occurred. Samples were scanned vertically from the top edge of sample holder to a height of 30 mm, samples are scanned 3 times with the sample holder rotating 120 ° between each scan to complete a 360 ° scan. The point clouds generated by the 3D scans are imported into Polyworks Inspector, a 3D

scanning software, and converted into a polygon model (Figure 13). The polygon model is then sectioned into planes perpendicular to the fibre axis and the cross sectional area of the intersection of the polygon model with each plane is generated into a report which can be exported into an excel file for further analysis. Manufactured microcomposites typically adhered to geometrical properties of 0.4 mm^2 diameters and 40 mm - 50 mm specimen lengths resulting in 25 mm – 35 mm gage lengths.

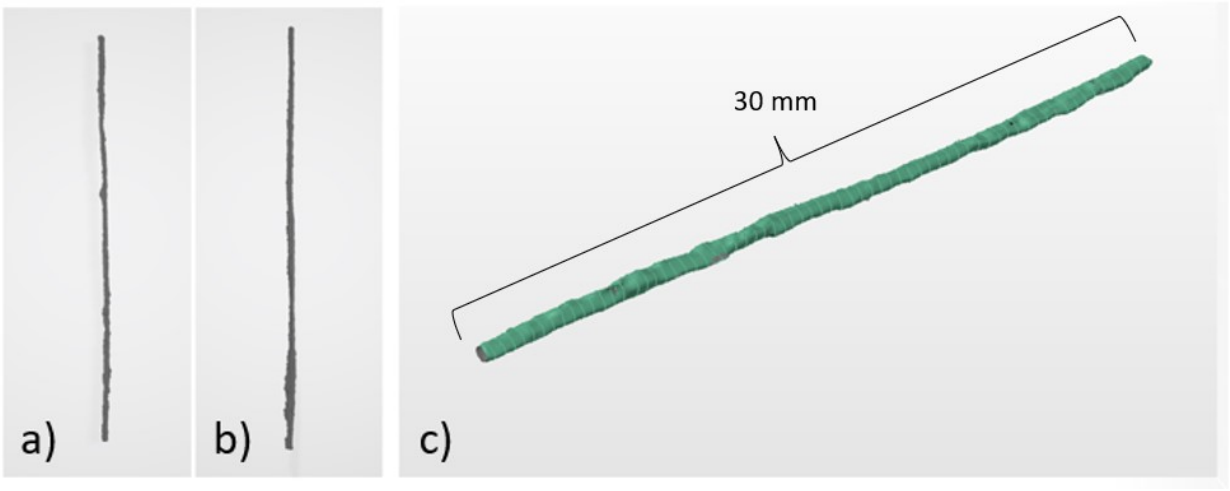

Figure 13: a) b) 3D scanned microcomposites shown as .stl files and c) polygon model sectioned for cross section report

3.5.2 Microcomposite Tensile Test Setup

An electromechanical test frame (ADMET eXpert 5601) was procured for conducting tensile tests of the microcomposites. Aluminium and alumina rods were machined to hold pinned specimen tabs as shown in Figure 14. An ADMET 1500FHI-200 load cell with a 200 lbf (889.64 N) capacity is used to record loads. A Thermcraft TSP-5-2-4-1S-J15084/1A furnace with a maximum temperature capability of 1535 °C can be moved into place for high temperature testing.

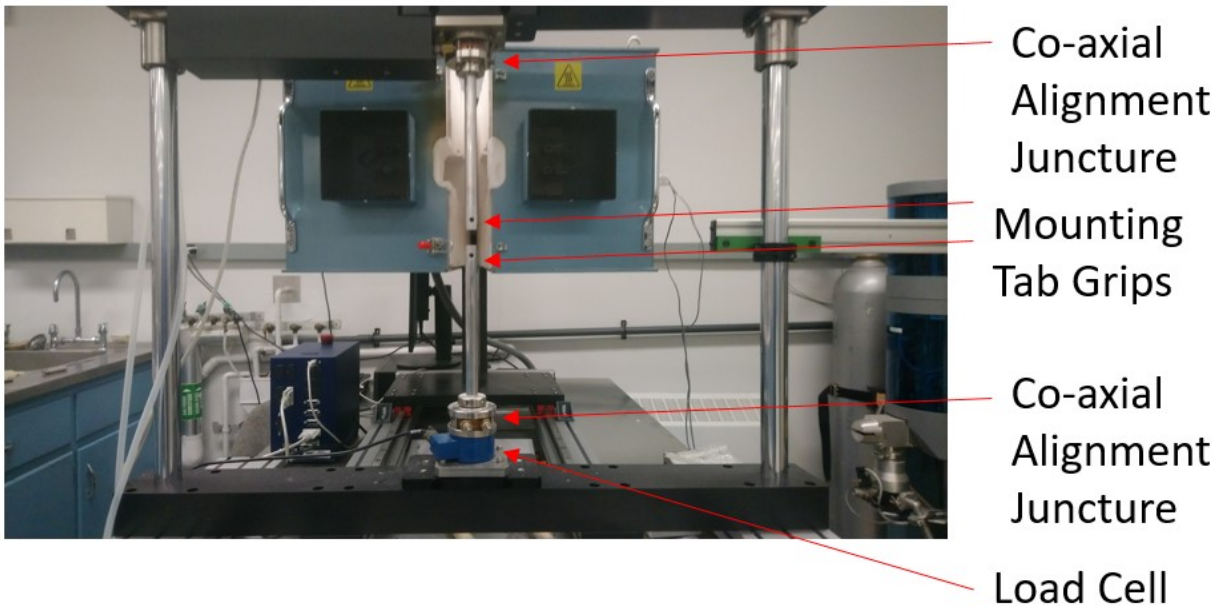

Figure 14: Admet eXpert 5601 with aluminum rods for pinned specimen tabs

Specimen are adhered to aluminum tabs using epoxy for room temperature tests and alumina tabs using AREMCO Ultratemp 516 high temperature adhesive for high temperature tests. Microcomposites are aligned within test tabs using a 3D printed tab holder. Tensile testing is undertaken using a displacement control mode with the displacement of the upper rod moving at a speed of 1 mm/min until a pre-load of 7 N is achieved for room temperature tests and 1 N for high temperature tests. The compliance of test setup is determined using three fibre samples each of three different lengths according to the methodology outlined by Silva et al. [92].

To elucidate the effects of high temperature exposure, six samples from each trial run given in Table 7 were placed in an open tube furnace (SentroTech ST-1500C) and heated at a rate of 4 °C/min to 1000 °C then soaked for a 1 hour duration before cooling at a rate of 4°C/min back to room temperature. These samples were then used to quantify tensile strength retention following exposure to a high temperature oxygen environment.

For high temperature tensile tests, the samples are heated to 1200 °C over the course of 90 minutes then soaked at 1200 °C for 30 minutes to eliminate any potential thermal gradients developed during heating.

3.6 Microscopy of Microcomposites and Fibre Coatings

For cross-sectional examination of coated fibre bundles and microcomposites, samples are cold mounted in an epoxy puck and allowed to cure overnight in an 800 mbar vacuum. Samples are then polished through

a progression (320 SiC until plane, 9μm diamond, 3 μm diamond, 0.05 μm alumina) specified by Buehler for the polishing of carbon fibre samples [93].

3.6.1 Scanning Electron Microscopy

A Philips XL30 SEFG scanning electron microscope is used to characterize microcomposite samples following the electrodeposition process as well as following testing. Secondary Electron (SE) examination mode is used to characterize samples where a greater depth of field yields more useful information than elemental composition. For samples where elemental composition is the data of primary interest BSE examination mode is used. For samples where low conductivity is a concern an Edwards E306 Carbon Coater is utilized to deposit a 9 nm layer coating of graphite on the surface, in some cases two layers of conductive graphite coating were deposited. An Octane Elect Plus sensor for energy dispersive X-ray detection (EDX) has been utilized in conjunction with TEAMs software to perform EDX analysis on post test samples to examine the elemental composition and extent of oxidation. Optical Microscopy and ImageJ Analysis

Optical microscopy has been performed on Batch 4 coated fibre bundles prior to their sintering heat treatment to characterize the thickness of the deposited coatings following EPD. An Olympus GX71 was used in either bright-field or dark-field view mode depending upon the sample being examined.

ImageJ, an opensource software package for reviewing and analysing images was utilized to measure coating thicknesses from the optical microscope images [94]. Images were converted to 8-bit type files which removes the colour from the image and assigns each pixel a tone value from 0 (white) to 255 (black). Following the type conversion a pixel:μm scale was determined using the 'Set Scale' function. This process was automated using the macro found in Appendix B1.

Following the conversion of the .tif file to a 8-bit type, the ImageJ multipoint tool was used to collect X and Y coordinates of the centre of up to 60 fibres per image. These coordinates are placed into the x1 and y1 arrays in a second programmed macro found in Appendix B2. Following the identification of the fibre centres the Image>Adjust>Threshold feature is used with the threshold range selected to filter out tones that do not correspond to the tone of the coatings. Upon application of the threshold feature, coating pixels are assigned a tone value of 255 and non-coating pixels are rendered white. The thickness measuring macro is then executed on the thresholded image (Figure 15). The basic functionality of the thickness measuring macro is to draw four 75 pixel lines (north, south, east, and west) from each fibre centre identified in the multi-point selection. These lines are then evaluated for the tone value of the pixel along the line (see Figure 16) and this data is recorded into a distance column and pixel column in an accompanying tab separated .txt file. These files are then uploaded into a programmed excel spreadsheet which records the

coating length for each drawn line and compiles the data from each individual fibre into an average. These values are then averaged again to create an overall coating thickness average for each trial run.

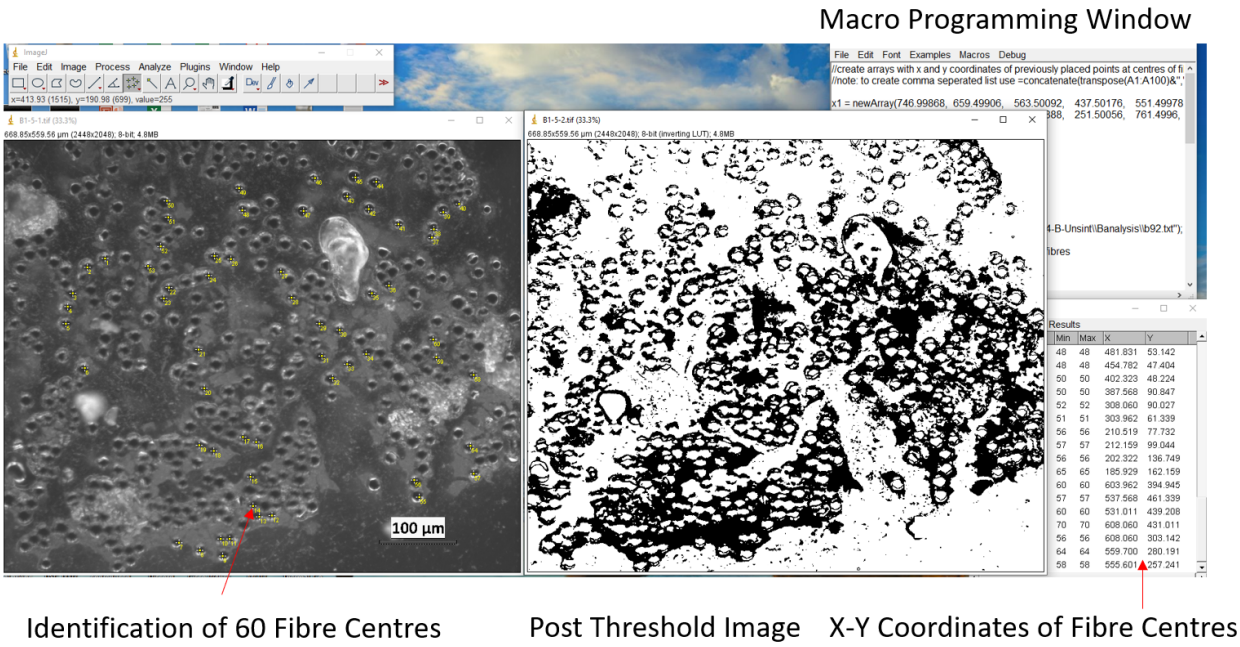

Figure 15: Overview of the ImageJ process for evaluating fibre bundle coating thickness original image has been captured using darkfield mode

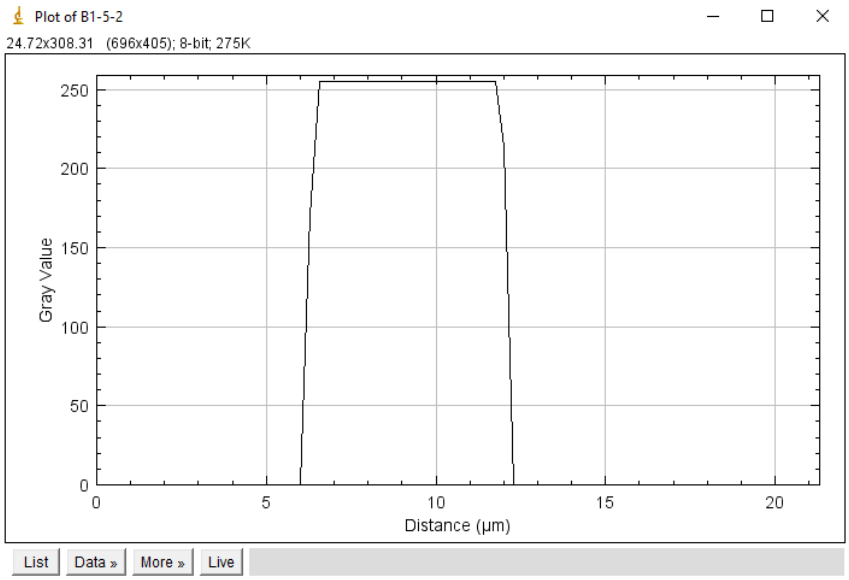

Figure 16: ImageJ Profile Plot of a line superimposed across a coating section in sample B1-5-2 following a threshold function

4. Evaluation of FMIs using Microcomposites

4.1 Initial Feasibility Study of Stationary EPD System

To evaluate whether a circular electrode could be utilized to deposit ceramic powders onto ceramic fibres and initial test run of different powder combinations and ceramic fibre combinations were placed into the stationary EPD cell then examined in the SEM for evidence of powder deposition. Figure 17 through Figure 19 exhibit the SEM examination of a few of these combinations.

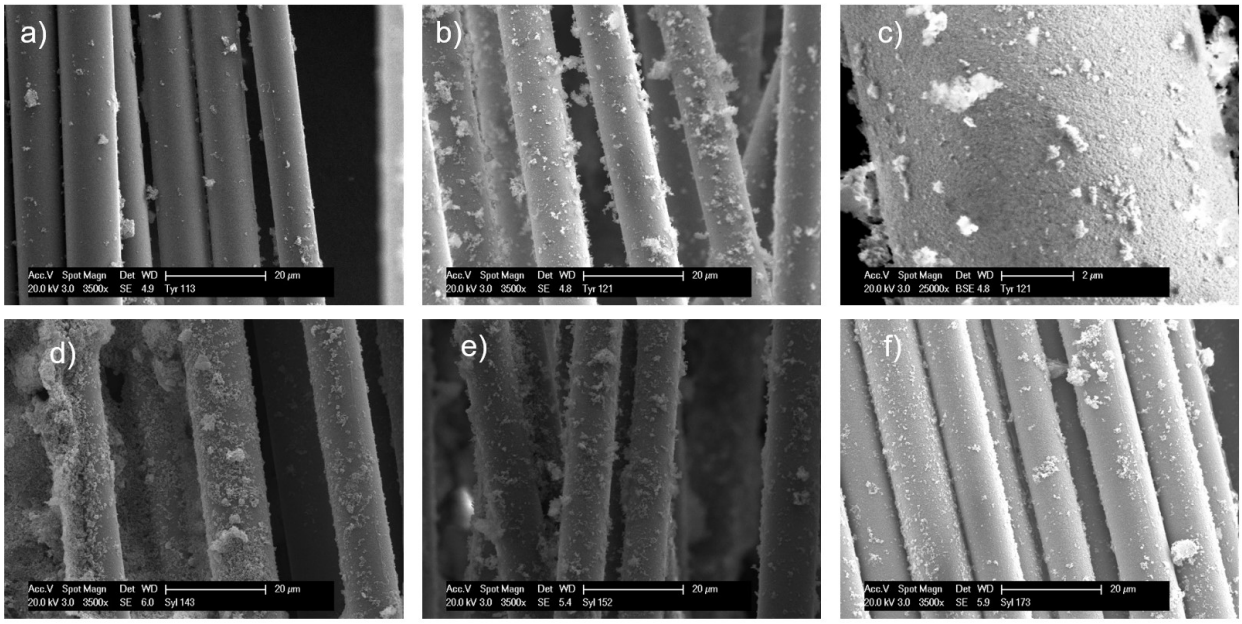

Figure 17: Al_2O_3/SiC coating applied to a)-c) Tyranno SiC fibre bundle and d)-f) Sylramic fibre bundle

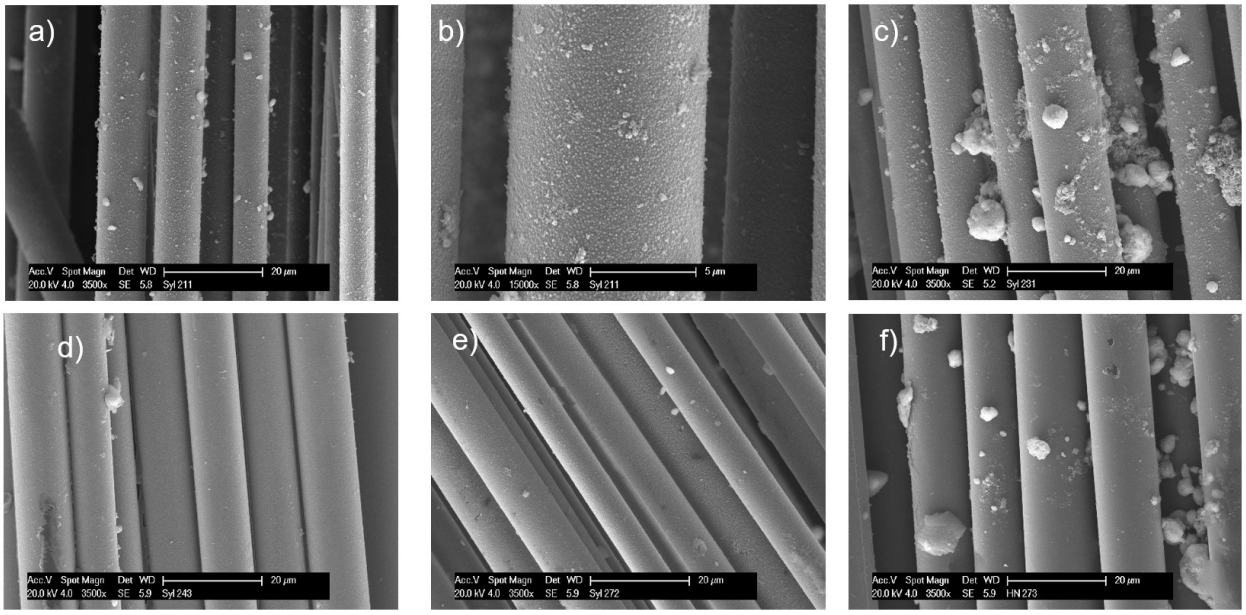

Figure 18: PSZ/BN coating applied to a)-e) Sylramic SiC fibre bundle and f) a Hi-Nicalon fibre bundle

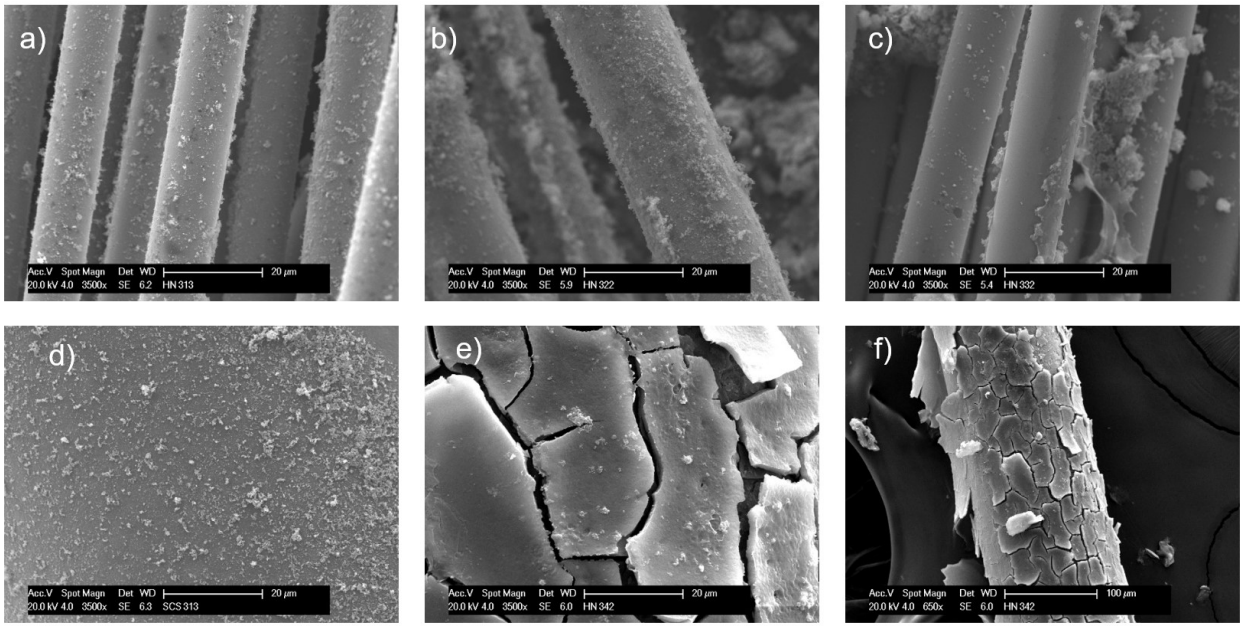

Figure 19: BN/ZTA coating applied to a)-c) Hi-Nicalon fibre bundles and d)-f) an SCS fibre

There are a few features to note from these early experiments. In Figure 17 there is evidence of agglomeration especially in image d) and e). In Figure 18, images d)-f) exhibit fibre bundles with very minimal deposition. Finally, in Figure 19 images e) and f) featuring the SCS filament it can be seen that a deposit was successfully coated upon the fibre, however, during drying the strength of the green body was

not able to overcome the stress gradient of the liquid phase leaving the deposit porous and resulting in significant mud cracking of the deposit.

4.2 Zeta Potential of Ceramic Nanopowder Colloids

The zeta potential and electrophoretic mobility of the ceramic nanopowder colloids as measured by the Litesizer™ are reported in Table 13.

Table 13: Zeta Potentials and Electrophoretic Mobility's of Ceramic Powders with CTAB and Dex+HCl as Zeta Potential Agents

Zeta Potential Agent	Nanopowder	Zeta Potential (mV)	Electrophoretic Mobility (µm*cm/Vs)
Dex+HCl	Al_2O_3	42.8 (SD = 2.37)	3.34
CTAB	Al_2O_3	41.3 (SD = 0.833)	3.22
Dex+HCl	$ZrO_2(3Y_2O_3)$	Unmeasured	Unmeasured
CTAB	$ZrO_2(3Y_2O_3)$	45.6 (SD = 0.656)	3.56
Dex+HCl	SiC	4.74 (SD = 0.826)	0.369
CTAB	SiC	53.0 (SD = 0.767)	4.13
Dex+HCl	Si_3N_4	Unmeasured	Unmeasured
CTAB	Si_3N_4	46.2 (SD = 0.733)	3.60
Dex+HCl	$85Al_2O_3$:$15ZrO_2$	24.2 (SD = 1.10)	1.89
CTAB	$85Al_2O_3$:$15ZrO_2$	40.5 (SD = 0.663)	3.16
Dex+HCl	BN	Unmeasured	Unmeasured
CTAB	BN	64.2 (SD = 0.616)	5.01
Dex+HCl	ZrC	Unmeasured	Unmeasured
CTAB	ZrC	Unmeasured	Unmeasured

Unfortunately, the Litesizer™ 500 encountered a hardware error before the entire run of colloid and powders could have their zeta potentials and electrophoretic mobility characterized, these results are reported as unmeasured in the table. Furthermore, the reported values for the Dex+HCl-SiC system appear to be a significant outlier in comparison to the other values that were measured, this powder colloid system will need to be re-examined once the machine is in working order again.

4.3 Microcomposite Tensile Testing

4.3.1 Microcomposite Cross-Section Evaluation

The microcomposite fabrication method utilized in this work resulted in some variance in the cross-sectional area of the microcomposite samples, both within individual samples as well as between samples. Cross-sectional variance results for batches 2 and 3 are reported in Table 14.

Table 14: Cross Sectional Variation within Microcomposites

Mean Cross Section (mm^2)	Cross Section Deviation in Individual Samples (mm^2)	Cross Section Standard Deviation Between Samples (mm^2)
0.383	0.168	0.137

4.3.2 Microcomposite Tensile Properties at Room Temperature and After Exposure to an Oxygen and Moisture Bearing Environment at 1000 °C

Representative tensile stress-strain curves for the samples show a mixture of brittle and damage tolerant behaviour and scatter within the tensile results as shown in Figure 20 and Figure 21.

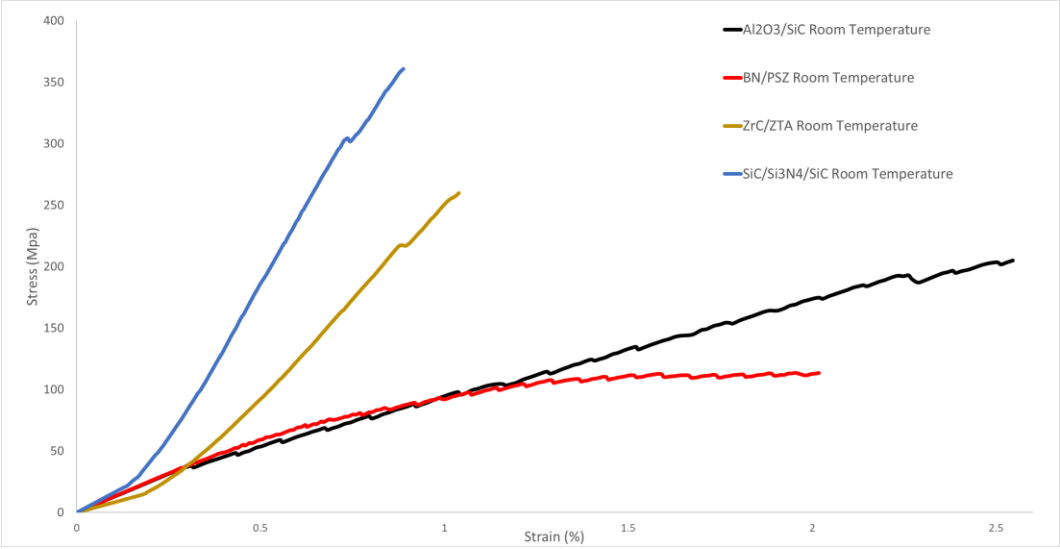

Figure 20: Representative tensile stress-strain curves for four different coating types of microcomposites at room temperature

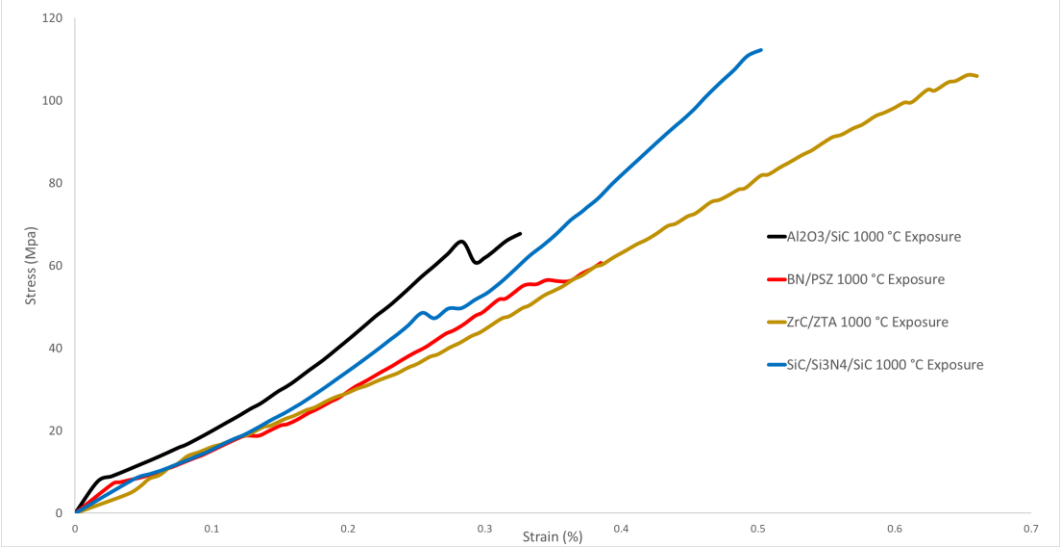

Figure 21: Representative tensile stress-strain curves for four different coating types of microcomposites after 1 h exposure at 1000 °C

The room temperature tensile stress-strain plots show examples of both pseudo-ductile failure (as seen in the Al_2O_3/SiC and BN/PSZ samples) as well as brittle failure (as seen in the ZrC/ZTA and SiC/S_3N_4/SiC samples). In the elevated temperature plots the stress-strain curves are much more characteristic of brittle failure. There is some evidence of pseudo-ductile behaviour being observed through a drop in the stress then a recovery as seen in the Al_2O_3/SiC, BN/PSZ, and SiC/Si_3N_4/SiC samples after elevated temperature exposure. The reduction of the pseudo-ductile behavior seen in post high temperature exposure composites and the absence of pseudo-ductile failure in some of the room temperature tensile samples suggests that the FMI is bonded too strongly to the fibre and matrix phases preventing the redirection of matrix damage and fibre pull-out necessary for graceful failure. This issue may be exacerbated in the post high temperature exposure samples due to oxidation and bonding of the fibre phase to the FMI. Tensile strength and strain at failure is reduced by exposure to 1000 °C in oxygen for 1 hour as seen in Figure 22 and Figure 23 as well as Table 15 through Table 18. Examining the results of the room temperature tensile tests, the highest strengths were exhibited by the SiC/Si_3N_4/SiC coating combination, followed by the ZrC/ZTA coating combination.

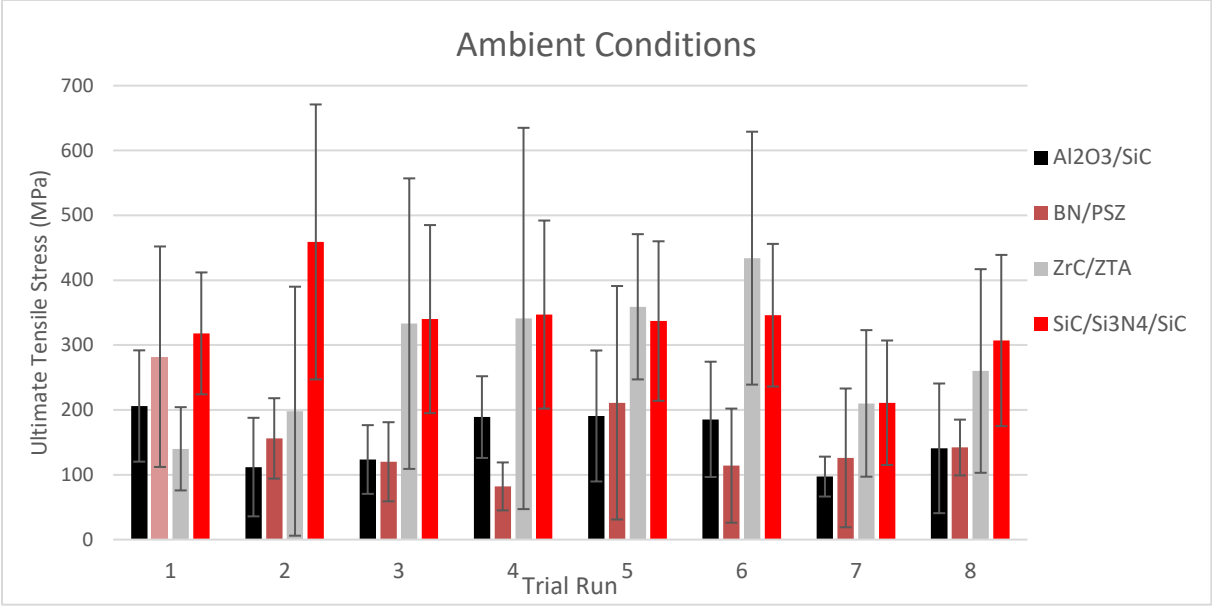

Figure 22: Ultimate Tensile Strengths test at room temperature of Al_2O_3/SiC, BN/PSZ, ZrC/ZTA, and SiC/Si_3N_4/SiC fibre matrix interphase coatings across the eight DoE trial run conditions

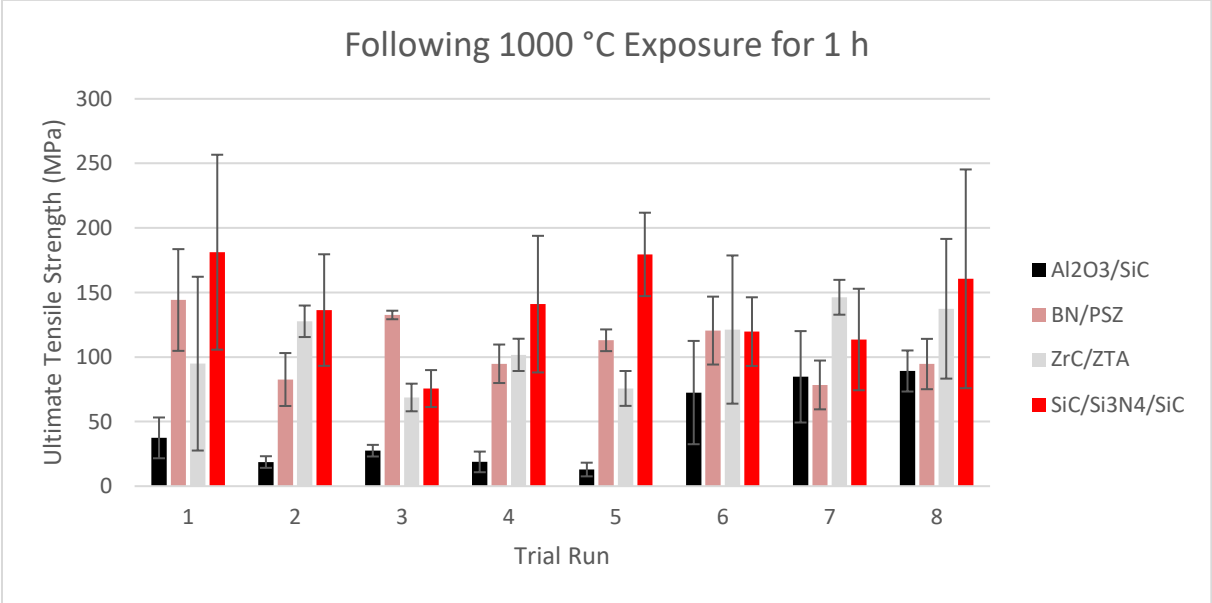

Figure 23: Ultimate Tensile Strengths test at room temperature following 1000 °C for 1 h of Al_2O_3/SiC, BN/PSZ, ZrC/ZTA, and SiC/Si_3N_4/SiC fibre matrix interphase coatings across the eight DoE trial run conditions

Table 15: Mechanical Properties of DoE Runs for Coating Al_2O_3/SiC

Run	Ultimate Tensile Strength (MPa)		Strain at Failure	
	Room Temperature	**1000 °C Exposure**	**Room Temperature**	**1000 °C Exposure**
1	**182.1** (SD = 61.8)	**37.4** (SD=15.8)	**0.0243** (SD = 0.01519)	**0.0064** (SD = 0.0039)
2	**79.4** (SD = 37.7)	**18.7** (SD = 4.5)	**0.0417** (SD = 0.0233)	**0.0058** (SD = 0.0019)
3	**101.7** (SD = 48.3)	**27.5** (SD = 4.5)	**0.0105** (SD = 0.0037)	**0.0068** (SD = 0.0024)
4	**171.5** (SD = 43.0)	**18.8** (SD = 8.0)	**0.0445** (SD = 0.0182)	**0.0051** (SD = 0.0021)
5	**149.6** (SD = 43.7)	**12.9** (SD = 5.3)	**0.0394** (SD = 0.0246)	**0.0041** (SD = 0.0026)
6	**172.3** (SD = 7.5)	**72.5** (SD = 40.0)	**0.0304** (SD = 0.0238)	**0.0047** (SD = 0.001135)
7	**97.2** (SD = 30.7)	**84.7** (SD = 35.4)	**0.0635** (SD = 0.0576)	**0.0059** (SD = 0.0031)
8	**90.4** (SD = 27.5)	**89.2** (SD = 15.9)	**0.0491** (SD = 0.0313)	**0.0128** (SD = 0.0074)

Table 16: Mechanical Properties of DoE Runs for Coating BN/PSZ

Run	Ultimate Tensile Strength (MPa)		Strain at Failure	
	Room Temperature	**1000 °C Exposure**	**Room Temperature**	**1000 °C Exposure**
1	**248.7** (SD = 145.9)	**144.2** (SD = 39.4)	**0.0347** (SD = 0.0176)	**0.0092** (SD = 0.0028)
2	**137.0** (SD = 38.4)	**82.6** (SD = 20.5)	**0.0542** (0.0313)	**0.0075** (SD = 0.0028)
3	**96.6** (SD = 41.4)	**132.6** (SD = 3.3)	**0.0590** (SD = 0.0407)	**0.0136** (SD = 0.0043)
4	**98.4** (SD = 35.6)	**94.8** (SD = 14.9)	**0.0603** (SD = 0.0189)	**0.0115** (SD = 0.0034)
5	**128.4** (SD = 72.9)	**113.0** (SD = 8.4)	**0.0335** (SD = 0.0208)	**0.0082** (SD = 0.0022)
6	**84.1** (SD = 40.5)	**120.5** (SD = 26.3)	**0.0439** (SD = 0.0340)	**0.0082** (SD = 0.0036)
7	**93.7** (SD = 48.6)	**78.4** (SD = 18.9)	**0.0536** (SD = 0.0391)	**0.0059** (SD = 0.0018)
8	**133.0** (SD = 36.0)	**94.6** (SD = 19.5)	**0.0103** (SD = 0.0047)	**0.0068** (SD = 0.0013)

Table 17: Mechanical Properties of DoE Runs for Coating ZrC/ZTA

Run	Ultimate Tensile Strength (MPa)		Strain at Failure	
	Room Temperature	**1000 °C Exposure**	**Room Temperature**	**1000 °C Exposure**
1	**70.2** (SD = 41.0)	**94.9** (SD = 67.3)	**0.0418** (SD = 0.0247)	**0.0049** (SD = 0.0026)
2	**154.3** (SD = 145.8)	**127.7** (SD = 12.2)	**0.0678** (SD = 0.0327)	**0.0236** (SD = 0.0065)
3	**267.9** (SD = 132.9)	**68.7** (SD = 10.7)	**0.0405** (SD = 0.0238)	**0.0103** (SD = 0.0041)
4	**249.7** (SD = 169.5)	**101.7** (SD = 12.5)	**0.0437** (SD = 0.0368)	**0.0149** (SD = 0.0094)
5	**341.5** (SD = 93.9)	**75.7** (SD = 13.5)	**0.0483** (SD = 0.0254)	**0.0071** (SD = 0.0036)
6	**365.7** (SD = 104.2)	**121.3** (SD = 57.4)	**0.0274** (SD = 0.0391)	**0.0119** (SD = 0.0056)
7	**171.1** (SD = 82.54)	**146.3** (SD = 13.5)	**0.0095** (SD = 0.0052)	**0.0060** (SD = 0.0021)
8	**201.5** (SD = 41.29)	**137.4** (SD = 54.1)	**0.0154** (SD = 0.0159)	**0.0070** (0.0027)

Table 18: Mechanical Properties of DoE Runs for Coating SiC/Si_3N_4/SiC

Run	Ultimate Tensile Strength (MPa)		Strain at Failure	
	Room Temperature	**1000 °C Exposure**	**Room Temperature**	**1000 °C Exposure**
1	**294.1** (SD = 66.7)	**181.2** (SD = 75.5)	**0.0145** (SD = 0.0038)	**0.0099** (SD = 0.0014)
2	**310.4** (SD = 62.7)	**136.4** (SD = 43.2)	**0.0211** (SD = 0.0167)	**0.0119** (SD = 0.00279)
3	**226.2** (SD = 77.3)	**75.6** (SD = 14.3)	**0.0135** (SD = 0.0047)	**0.0084** (SD = 0.0026)
4	**217.3** (SD = 49.2)	**141.0** (SD = 52.9)	**0.0166** (SD = 0.0102)	**0.0152** (SD = 0.0047)
5	**284.6** (SD = 68.9)	**179.5** (SD = 32.3)	**0.0210** (SD = 0.013)	**0.0076** (SD = 0.0011)
6	**304.7** (SD = 95.0)	**119.7** (SD = 26.6)	**0.0199** (SD = 0.0097)	**0.0102** (SD = 0.0077)
7	**214.4** (SD = 88.9)	**113.6** (SD = 39.3)	**0.0253** (SD = 0.0234)	**0.0074** (SD = 0.0013)
8	**264.6** (SD = 81.2)	**160.6** (SD = 84.7)	**0.0127** (SD = 0.0078)	**0.0091** (SD = 0.0011)

One challenge of using microcomposites (vs. full size samples) for the characterization of tensile properties is the degree of scatter present in the results. This scatter arises from several factors related to either microcomposite processing or the functional properties of the CMC. During the microcomposite processing, cross-sectional areas vary; low cross-sectional area areas ensures that internal porosity will have a significant effect on material properties. Also, there are uncertain residual stress states and variable internal fibre spacing causing variation in the fibre volume fraction [95] [96]. Variability due to functional properties is caused by uncertainty in the tensile properties of the matrix phase (varied due to processing conditions), inherent variation in the tensile properties of the individual fibre, and the uncharacterized ability of the interphase to effectively transfer loads between the fibre phase and the matrix phase during deformation [44]. To reduce the effect of the scatter on the results, test data has been filtered; for each data set the upper and lower quartile has been calculated, data outside a range of 1.5x the interquartile above and below the upper and lower quartile respectively has been excluded [95]. Despite the scatter in the properties observed in this study, microcomposites remain a cost and time effective method of examining large design spaces for determining suitable process/material combinations during development. One approach for reducing the scatter is to use a PIP matrix fabrication approach to reduce the contributions of residual carbon, residual silicon, and residual porosity to the matrix property variability. This will increase the process time but the improved reliability of the characterization properties are likely worth the trade-off in the future studies.

A comparison of the tensile strength retention of the different coating combinations after thermal exposure are exhibited in Figure 24 and Figure 25.

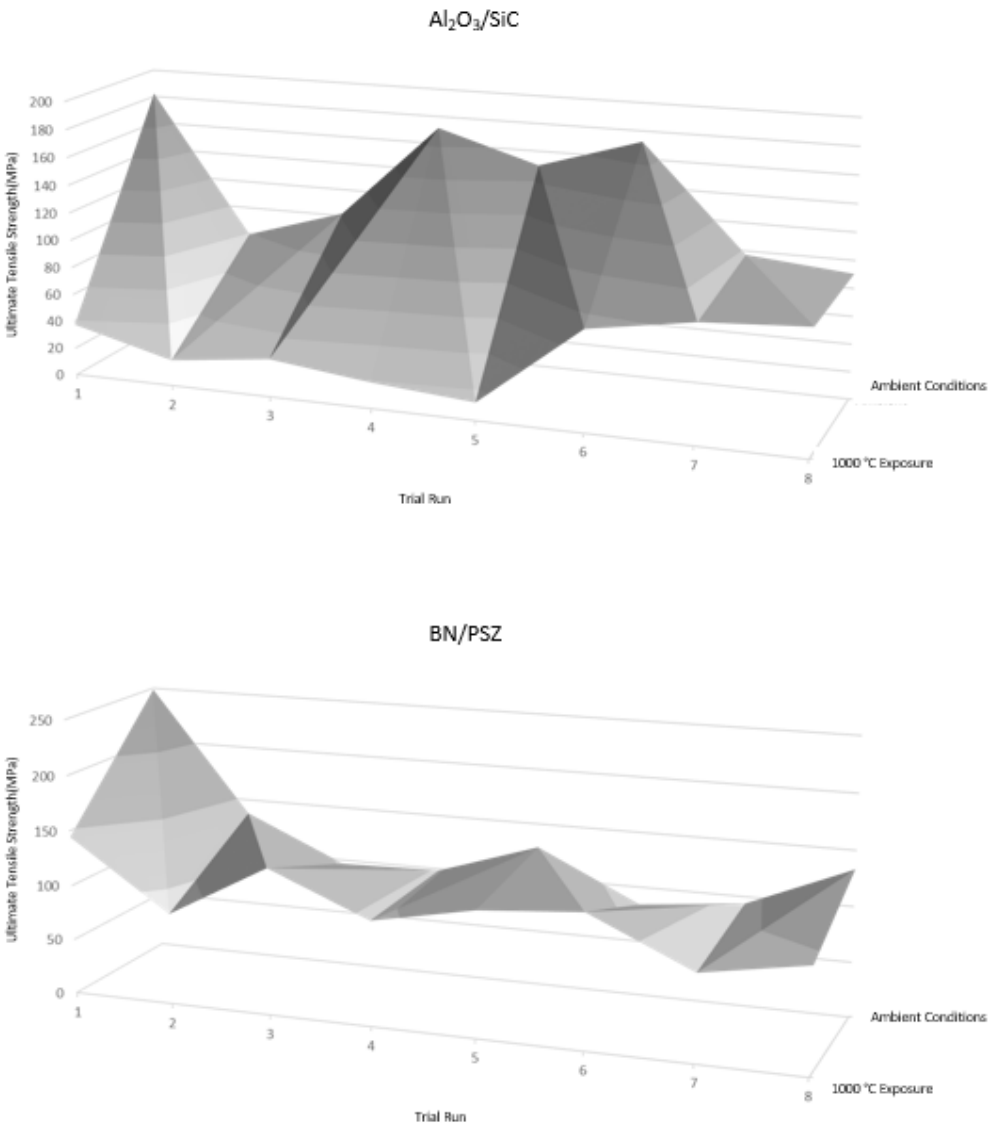

Figure 24: Surface plots of tensile strength degradation for each trial run condition caused by 1 h of exposure to 1000°C for Al_2O_3/SiC and BN/PSZ coatings

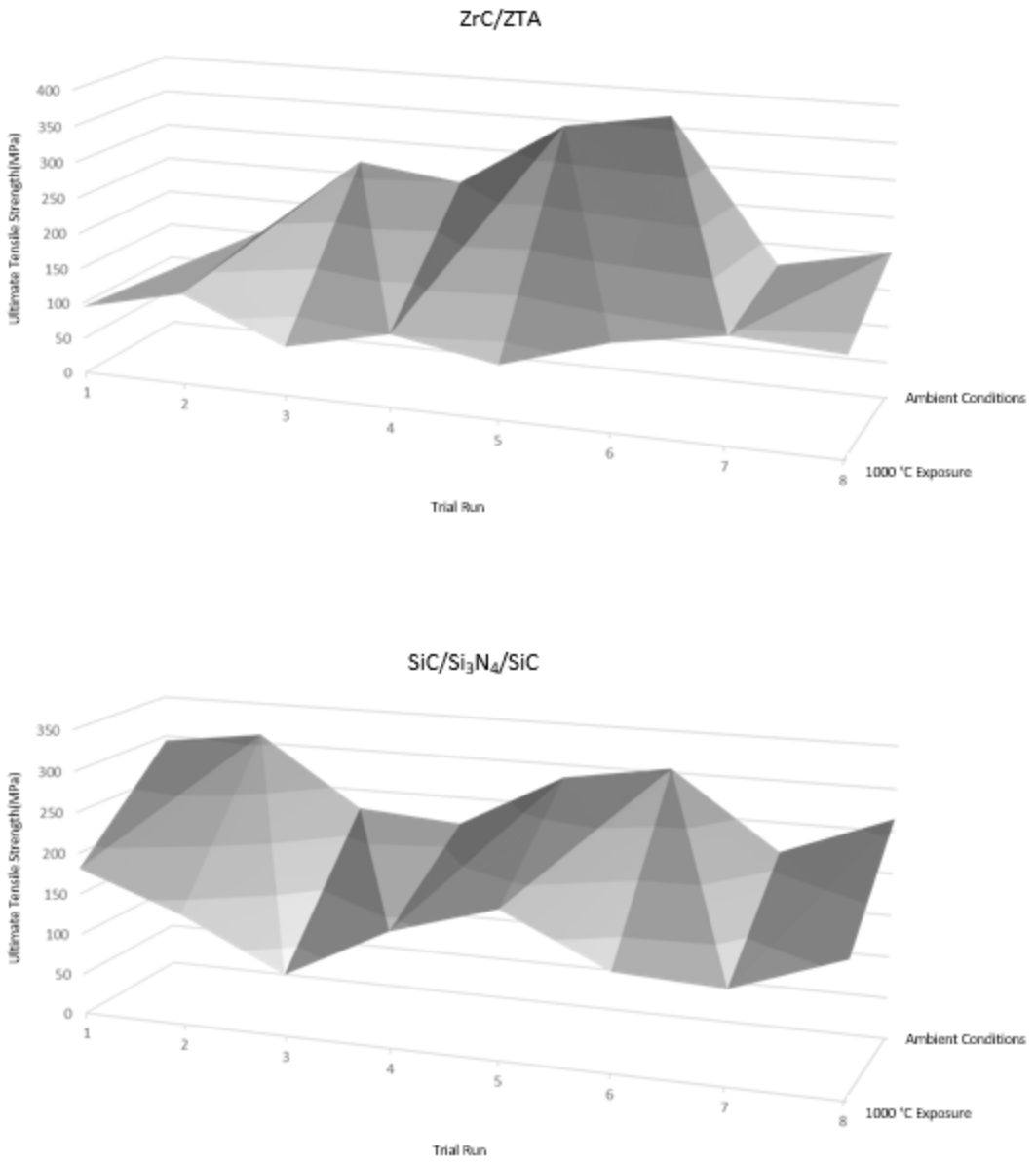

Figure 25: Surface plots of tensile strength degradation for each trial run condition caused by 1 h of exposure to 1000°C for ZrC/ZTA and SiC/Si_3N_4/SiC coatings

Based upon the results seen in Table 15 through Table 18 the two coatings of greater potential for their ability to resist environmental degradation are the BN/PSZ and SiC/Si_3N_4/SiC combinations. These results are further illustrated in the surface plots in Figure 24 and Figure 25, where the gradient indicating strength degradation is least apparent in the BN/PSZ coating followed by the SiC/Si_3N_4/SiC.

The use of BN to create a B_2O_3 layer which acts as an environmental protection barrier for the fibre phase has been previously reported [32] [97] [98] [99] [100]. The loss in tensile strength for the Al_2O_3/SiC and ZrC/ZTA coating combinations suggests that using an oxide to act as an environmental barrier coating is

not as effective against oxidation as that with a semi-sacrificial reactive coating such as BN. This is likely due to the deposited interphase being discontinuous allowing oxygen to reach the fibre surface. In a comparison of the trial runs under different processing conditions, process conditions in trial runs 7 and 8 have the overall best results for strength retention following high temperature exposure. The commonality between trial runs 7 and 8 include high voltage, high deposition time and low solids loading. This design space is explored further in Batch 4 and Batch 5 microcomposites.

Lastly, for the first two coating variations (Al_2O_3/SiC and BN/PSZ), the measured mechanical properties exhibited generally lower tensile strengths and higher strain to failures suggesting that the interphase is not performing its desired role of transferring loads between the fibre phase and the matrix phases as well as transferring loads between individual fibres [14]. In most circumstances, a larger strain to failure indicates a greater pseudo-ductility which is desirable; however, if this larger strain to failure is accompanied by a low ultimate tensile stress than the potential structural applications of the CMC become severely limited.

4.3.3 High Temperature Tensile Testing of Microcomposites

Based upon the results of the room temperature tests of microcomposites after exposure to 1000 °C, Batch 4 (Table 12) was fabricated with BN/PSZ and SiC/Si_3N_4/SiC coating systems for tensile test under high temperature. Unfortunately, during the silicization of batch 4 the furnace malfunctioned and had a significant over-temp event which compromised the entire batch. Batch 5 was fabricated using the same conditions as batch 4. Six samples from each trial run for batch 5 were tested at room temperature to establish a baseline strength for these composites, then the two coating conditions which exhibited the greatest strength were selected for high temperature testing at 1200 °C in air. These samples were affixed to alumina tabs using ADMET 516 high temperature adhesive as covered in section 3.5.2. It was discovered during high temperature testing that these samples were failing within the adhesive without bearing significant load. Scanning electron microscopy was utilized to examine the failure points of these samples, select results are presented in Figure 26.

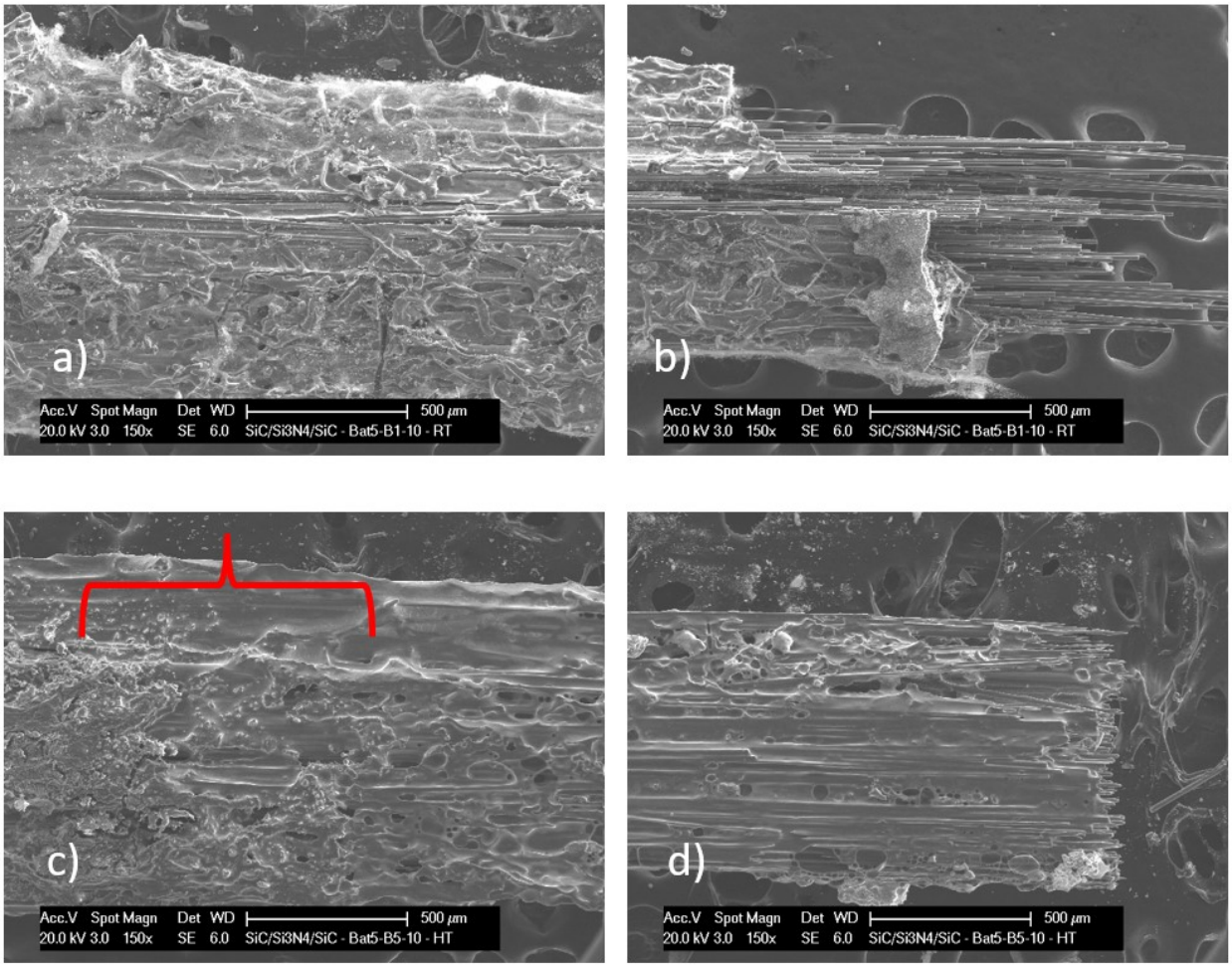

Figure 26: SEM images of a) Sample B1-10 post room temperature tensile test gage section b) Sample B1-10 post room temperature tensile test fracture surface c) Sample B5-10 post high temperature tensile test, transition between gage section to bonding zone d) Sample B5-10 post high temperature tensile test terminal point within adhesive

Samples B1-10 and B5-10 were examined under SEM, both of which were also adhered to alumina tabs using the high temperature adhesive. Sample B1-10 was tested at room temperature and fractured in the gage section in a manner consistent with other microcomposite tensile tests detailed in Section 4.3.2. Sample B5-10 was tested at 1200 °C and the sample pulled out of the adhesive before an appreciable load could be applied. Examining the transition zone between the gage section and the adhesive it can be seen that the matrix coating became porous either during the adhesive curing treatment or during the heating prior to the application of load by reacting with the adhesive. This is even more apparent on another high temperature test specimen shown in Figure 27, where large, interconnected pores are more evident.

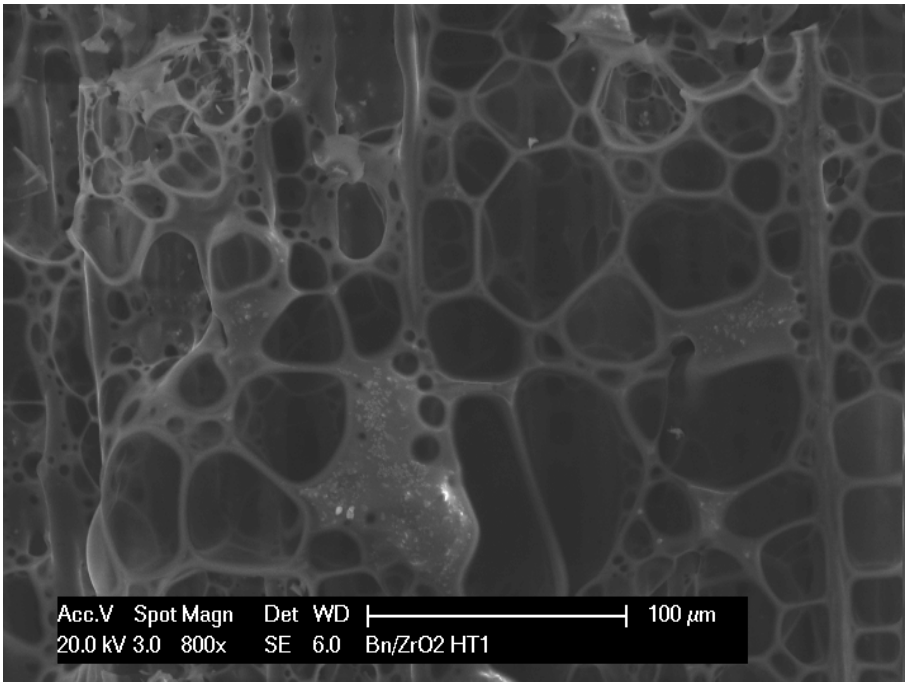

Figure 27: SEM examination with 800x magnification of a BN/PSZ batch 5 sample following a high temperature tensile test

AREMCO 516 Ultra-Temp adhesive is a ZrO_2 based adhesive which utilizes a proprietary blend of solvents which volatize during curing to allow for the consolidation of ZrO_2 powder thereby forming the adhesive bond. A thermogravimetric analysis of the microcomposite system in contact with the high temperature adhesive would elucidate whether the reaction between of the coating matrix and adhesive occurs during curing or during the heat ramp and soak portion of the high temperature test. It may be possible to employ an additional bond coat between the microcomposite and the high temperature adhesive to allow for high temperature testing of microcomposites; however, exploring bond coat systems was deemed beyond the scope of this work.

4.4 Microscopy Examination of Microcomposites and Coated Fibre Bundles

4.3.1 Electron Microscopy Examination of Microcomposites and Coated Fibre Bundles

For the first coating (Al_2O_3/SiC) an examination using the BSE mode of the SEM reveals porosity between the Al_2O_3 base coating and the fibre surface (Figure 28). It appears that the coating recedes from the fibre surface during sample processing. There isn't a well defined boundary between the Al_2O_3 content and the SiC inclusions deposited in the second coating step suggesting that the Al_2O_3 content deposited in the first step is preventing further infiltration into the fibre bundles by subsequent coating steps. Similar occurrence is observed on the second coating variety (BN/PSZ) as seen in Figure 29.

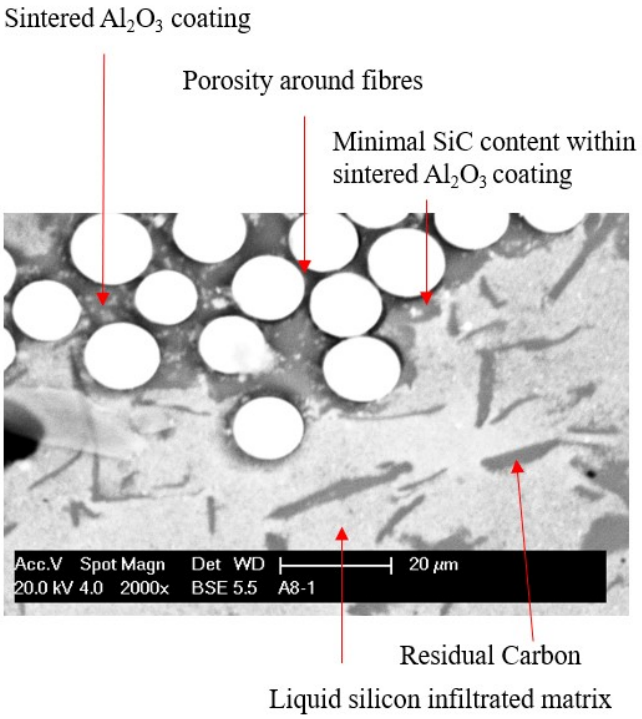

Figure 28: BSE image of Al_2O_3/SiC coating at 2k magnification showing interphase debonding from the fibres

A common feature shared between the first coating combination (Al_2O_3/SiC) and the second coating combination (BN/PSZ) is that both coatings use a larger nano particle for the first deposition step. This leads to two possible issues for the processing of CMCs with EPD deposited FMIs. The first, as evidenced by inter-fibre porosity, is the likelihood of access to regions between the internal fibres as they are blocked by previously deposited nanopowders. Additionally, the conversion of the deposited nanopowder green body to solid ceramic by sintering during processing leads to a reduction in the coating volume. This volume reduction is greater in green bodies with larger particle sizes [101]. Porosity within the matrix phase of the microcomposite presents a significant challenge to characterizing the tensile properties due to three compounding reasons: porosity reduces cross sectional area bearing load increasing the stress applied to the phases surrounding the porosity, it further aggravates this issue by acting as a stress concentrator, and finally it acts as a pathway for the ingress of oxygen further degrading the fibre and matrix phases.

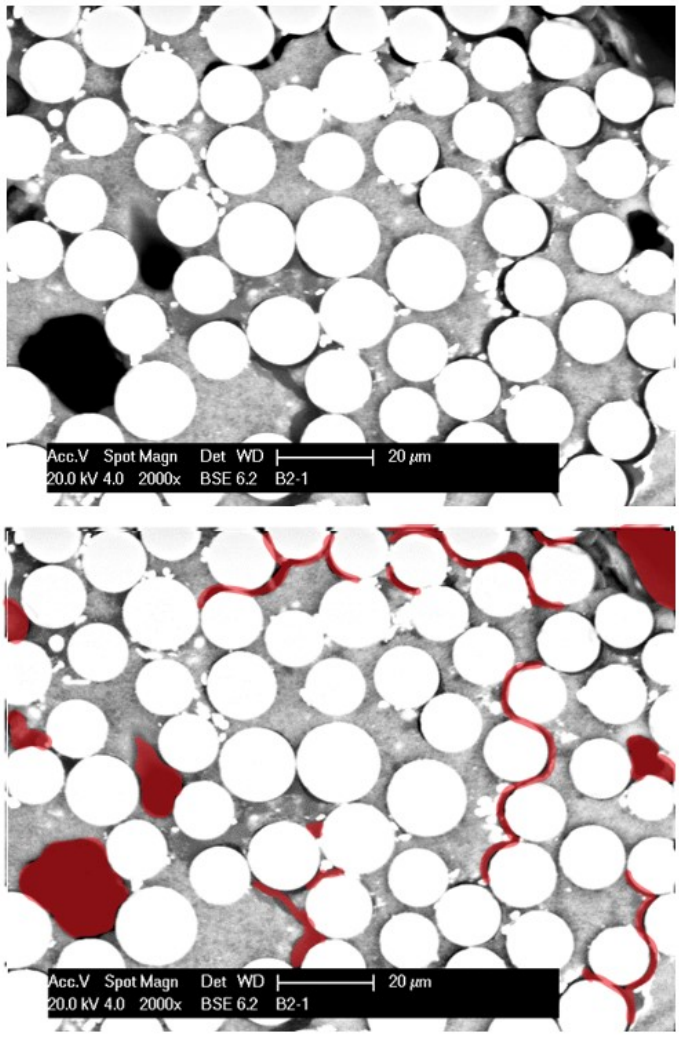

Figure 29: BSE image of BN/PSZ coating sample at 2k magnification showing interphase debonding and inter-fibre porosity highlighted with red

The third (ZrC/ZTA) and fourth (SiC/Si_3N_4/SiC) coating combinations demonstrate overall greater mechanical strength properties with the SiC/Si_3N_4/SiC coating demonstrating both the most consistent higher strength between trial runs as well as less scatter within each trial run.

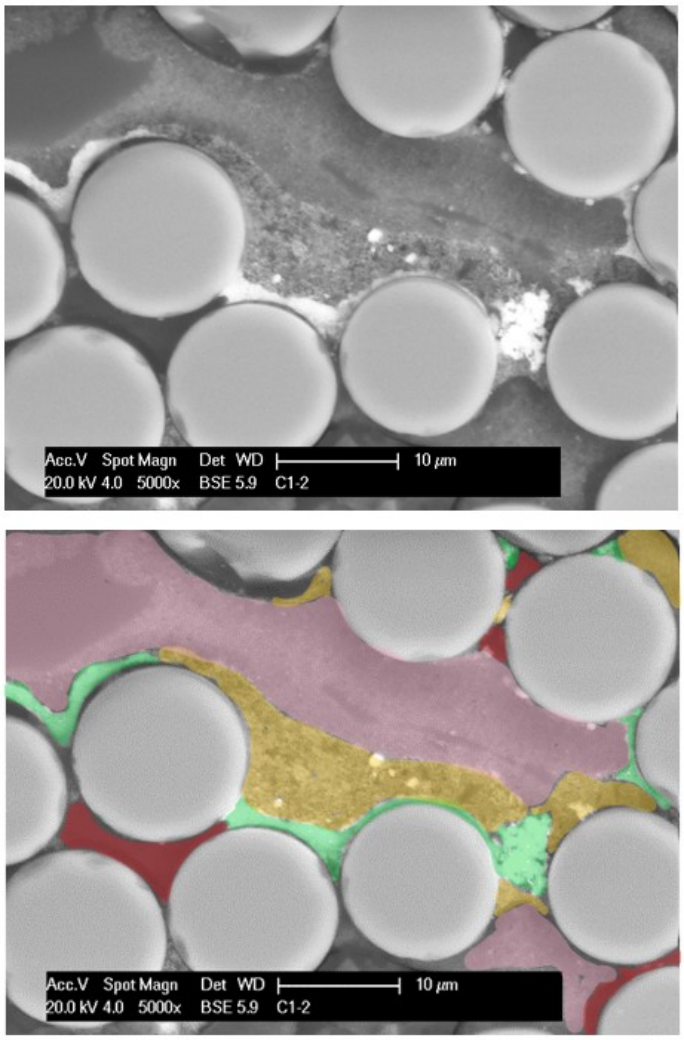

Figure 30: BSE examination of ZrC/ZTA coated sample at 5kx, purple highlighted region is LSI matrix, orange highlighted region is ZTA coating, green highlighted region is ZrC, red highlighted region is porosity

Figure 30 provides evidence as to why the ZrC/ZTA coating produced better microcomposites in terms of tensile strength despite the utilization of a deposition layer with a larger nano particle. It can be seen that the initial ZrC coating is able to infiltrate onto the fibre tows more successfully than BN or Al_2O_3 of the initial coatings. It can also be seen that in some regions the second ZTA coating envelopes the ZrC coating and provides a secondary layer between the ZrC coating and the liquid silicon infiltrated matrix. Porosity between closely packed fibres is still observable in Figure 30.

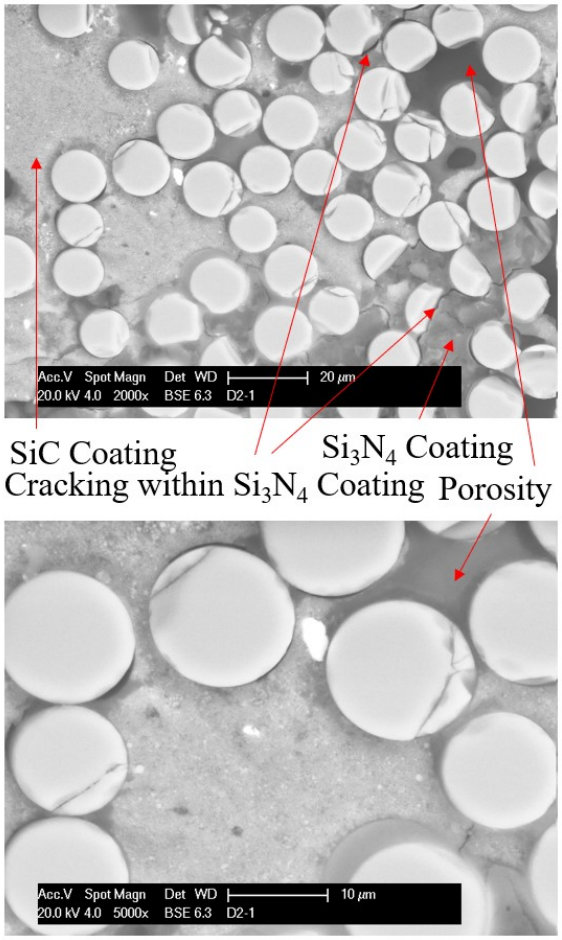

Figure 31: BSE images of SiC/Si_3N_4/SiC sample at 2kx and 5kx magnifications

Figure 31 shows an SEM image of a sample from the fourth coating (**SiC/Si_3N_4/SiC**). There are fewer regions in this sample where the coating has receded from the fibre. This is the case in the regions dominated by SiC deposition as well Si_3N_4 depositions. Similar to Figure 29, a crack can be observed branching within the coating and between the fibres. This cracking is more readily observed within the Si_3N_4 dominated region (labelled by arrows) than in the SiC dominated region. The improved tensile properties could be a result of the addition of a third coating step as well as of using a smaller nanopowder for initial deposition.

Based upon the results shown in Table 15 through Table 18 and Figure 28 through Figure 31 it is evident that the initial coating layer should consist of a smaller nano powder to increase the probability of inter-fibre deposition and reduce the risk of coating recession from the fibre during processing. However, the scatter in the tensile results must be considered before drawing definite conclusions about optimal deposition parameters. Based upon the results from batch 2 and 3, additional batches were fabricated focusing primarily on the BN/PSZ and SiC/Si3N4/SiC compositions utilizing 3-level variables to determine

whether factors such as electric field, and duration have a linear or parabolic effect upon the tensile properties. The use of more optimal coating parameters is expected to improve the uniformity of the coating around individual fibres and contribute to greater inter-fibre infiltration. However, if substantial coating durations are required to ensure full infiltration, one must balance the performance and the cost in large scale production.

Polished cross sections of the different coating combinations after thermal exposure were examined using the BSE scanning mode of the SEM, as well as an EDX spectrometer. The oxidation of the matrix and fibre phase can be observed in all four coating examples shown in Figure 32 through Figure 35. The contrast seen within the fibre phase in the samples exposed to high temperature indicates that oxidation within the fibre phase is occurring with the most significant oxidation occurring in the Al_2O_3/SiC coating (Figure 32) and the ZrC/ZTA coating (Figure 34) which is expected based upon the lower tensile strength observed. The observation that oxidation is present within fibres near the center of the sample as well as near the edges indicates that oxygen is able to ingress throughout the microcomposite. This is likely mechanisms for this ingress are gas transport through pore networks and matrix microcracks, diffusion through residual carbon phases within the matrix, as well as diffusion along the fibre axis due to the limited length of the microcomposites being tested.

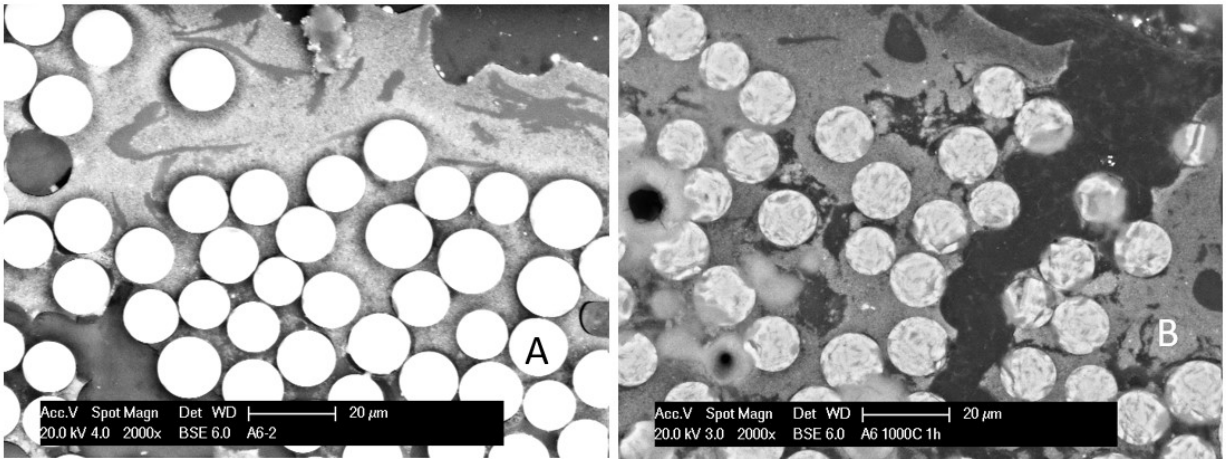

Figure 32: Al_2O_3/SiC coating under BSE inspection at 2kx magnification A) Room Temperature B) 1 h exposure at 1000 °C

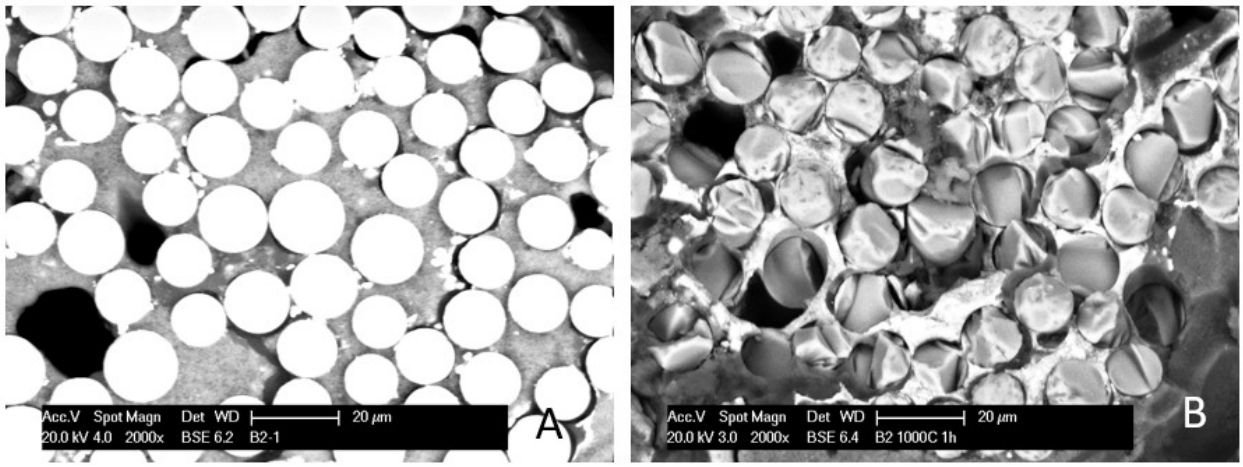

Figure 33: BN/PSZ coating under BSE inspection at 2kx magnification A) Room Temperature B) 1 h exposure at 1000 °C

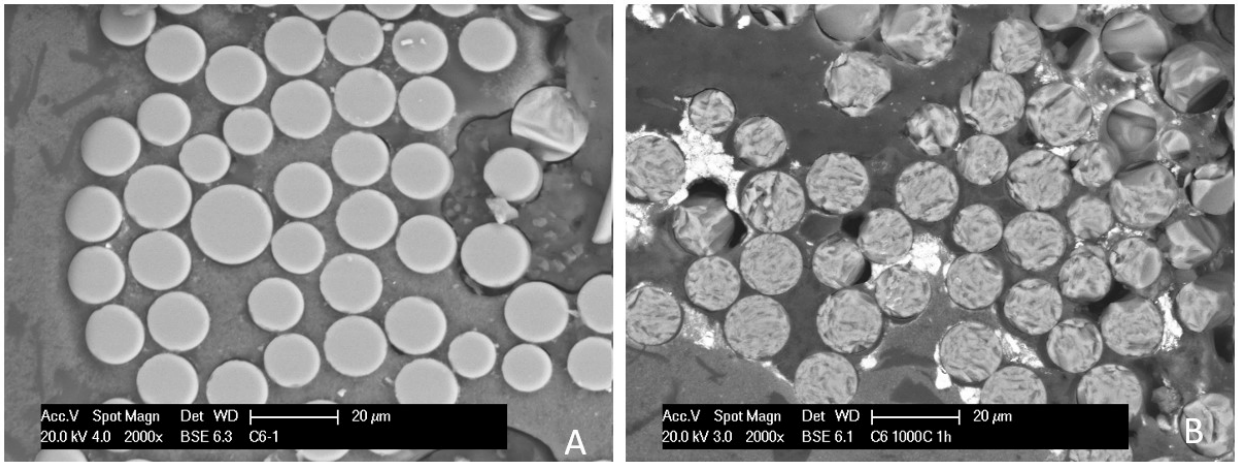

Figure 34: ZrC/ZTA coating under BSE inspection at 2kx magnification A) Room Temperature B) 1 h exposure at 1000 °C

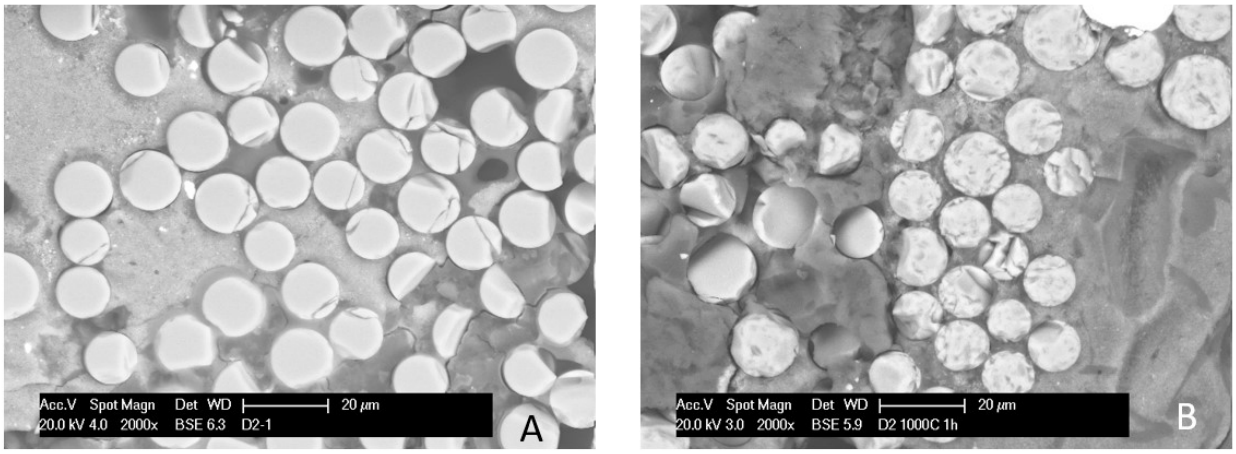

Figure 35: $SiC/Si_3N_4/SiC$ coating under BSE inspection at 2kx magnification A) Room Temperature B) 1 h exposure at 1000 °C

Further confirmation of fibre degradation through oxidation is accomplished by the EDX analysis of the samples shown in Figure 36 through Figure 39. The spot EDX analysis seen in Figure 36 features three spots with the first spot examining a fibre and the following two spots examining different interphases. The first spot confirms that oxygen has penetrated the matrix and interphase and has partially converted the SiC fibre into SiO_2, similar to that seen in uncoated SiC fibre samples exposed to high temperature oxidizing atmospheres [102]. Comparing spot 2 and spot 3 it is likely that the Al_2O_3 phase did not deposit on the fibre near spot 2 (no Al detected) whereas Al can be detected in spot 3.

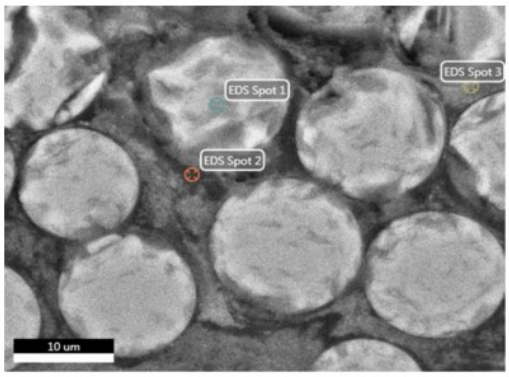

Spot 2

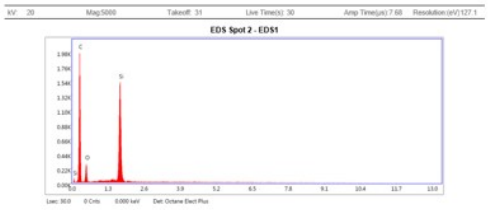

Element	Weight %	Atomic %	Net Int.	Error %	Kratio	Z	A	F
C K	75.96	84.14	388.00	8.31	0.2855	1.0193	0.3687	1.0000
O K	12.50	10.40	50.85	14.59	0.0151	0.9740	0.1244	1.0000
SiK	11.53	5.46	438.61	2.98	0.0936	0.8833	0.9163	1.0027

Spot 1

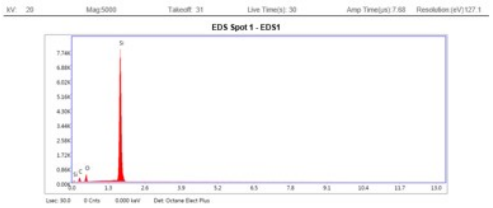

Element	Weight %	Atomic %	Net Int.	Error %	Kratio	Z	A	F
C K	29.31	45.57	43.05	13.56	0.0342	1.0805	0.1081	1.0000
O K	14.79	17.27	83.27	11.47	0.0268	1.0348	0.1751	1.0000
SiK	55.90	37.17	2129.34	2.03	0.4911	0.9418	0.9327	1.0005

Spot 3

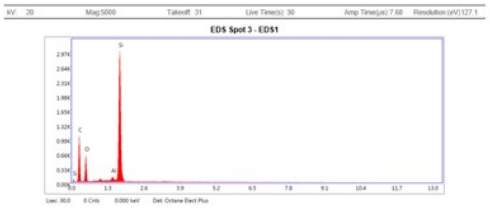

Element	Weight %	Atomic %	Net Int.	Error %	Kratio	Z	A	F
C K	56.65	68.89	201.72	10.11	0.1361	1.0366	0.2318	1.0000
O K	21.75	19.85	119.03	11.56	0.0325	0.9912	0.1508	1.0000
AlK	1.00	0.54	36.65	8.27	0.0071	0.8807	0.7938	1.0108
SiK	20.60	10.71	838.51	2.85	0.1641	0.8998	0.8838	1.0016

Figure 36: Spot based EDX analysis of Al_2O_3/SiC coated sample exposed to 1000 °C for 1 h with: Spot 1 focusing on a fibre, Spot 2 focusing on interphase, and Spot 3 focusing on a second area of interphase

The spot EDX analysis of a BN/PSZ coated sample indicates the deposition of the PSZ phase signaled by the presence of Zr at spot 1 and spot 3; however, B_2O_3 and BN (i.e., B or N) were undetected within the interphases of this sample, due to the inability of the EDS to measure light elements. In comparing spot 2 from Figure 36 and spot 5 from Figure 37 both of which target the edge of a fibre, it can be seen that the BN/PSZ coating protected the fibre from oxidation more effectively based upon the lower oxygen content detected in spot 5. (However, it is to be noted, the detection of oxygen by EDS is only qualitative, the observations were made by the relative peak intensity of oxygen vs. that of silicon on the EDS spectra.)

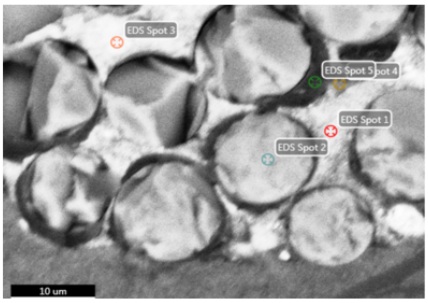

Spot 3

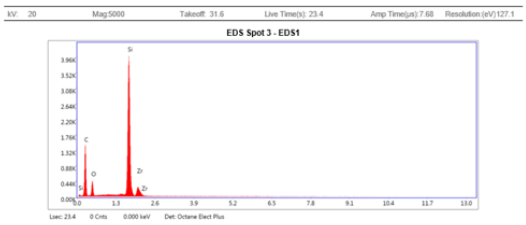

Element	Weight %	Atomic %	Net Int.	Error %	Kratio	Z	A	F
C K	61.28	75.03	366.03	9.90	0.1449	1.0418	0.2270	1.0000
O K	15.12	13.90	127.44	12.00	0.0204	0.9966	0.1355	1.0000
SiK	20.05	10.50	1430.36	2.58	0.1643	0.9056	0.9018	1.0029
ZrL	3.54	0.57	88.30	7.40	0.0240	0.6980	0.9743	0.9990

Spot 1

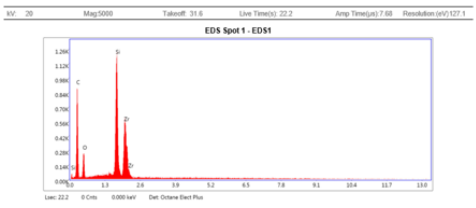

Element	Weight %	Atomic %	Net Int.	Error %	Kratio	Z	A	F
C K	60.14	77.05	229.62	10.40	0.1511	1.0611	0.2367	1.0000
O K	15.11	14.53	73.84	13.17	0.0197	1.0165	0.1281	1.0000
SiK	11.20	6.14	474.87	3.57	0.0906	0.9260	0.8682	1.0060
ZrL	13.56	2.29	223.59	4.12	0.1012	0.7140	1.0456	0.9996

Spot 5

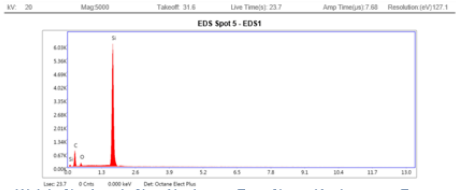

Element	Weight %	Atomic %	Net Int.	Error %	Kratio	Z	A	F
C K	56.67	72.85	191.31	11.02	0.0964	1.0478	0.1623	1.0000
O K	8.03	7.75	53.77	13.54	0.0110	1.0025	0.1363	1.0000
SiK	35.31	19.41	2069.86	2.04	0.3026	0.9109	0.9398	1.0010

Figure 37: Spot based EDX analysis of BN/PSZ coated sample exposed to 1000 °C for 1 h with: Spot 1 focusing on interphase, Spot 3 focusing on a second area of interphase, and Spot 5 focusing on the edge of a fibre

In addition, two EDX line scans were carried out on the ZrC/ZTA (Figure 38) and SiC/Si_3N_4/SiC coatings (Figure 39). In both line scans there is greater oxygen content in the matrix phase than in the centres of the fibres; however, oxygen content increases at the edge of fibres as highlighted by the red circles in Figure 38 and Figure 39. Figure 39 gives an example of a carbon-rich portion of the matrix between the 17.1 µm and 53.1 µm line markers (within the circles), this region coincides with the greatest oxygen peak height at the fibre surface indicating that the carbon rich phase is less effective at protecting the fibres from oxidation during the exposure at 1000 °C.

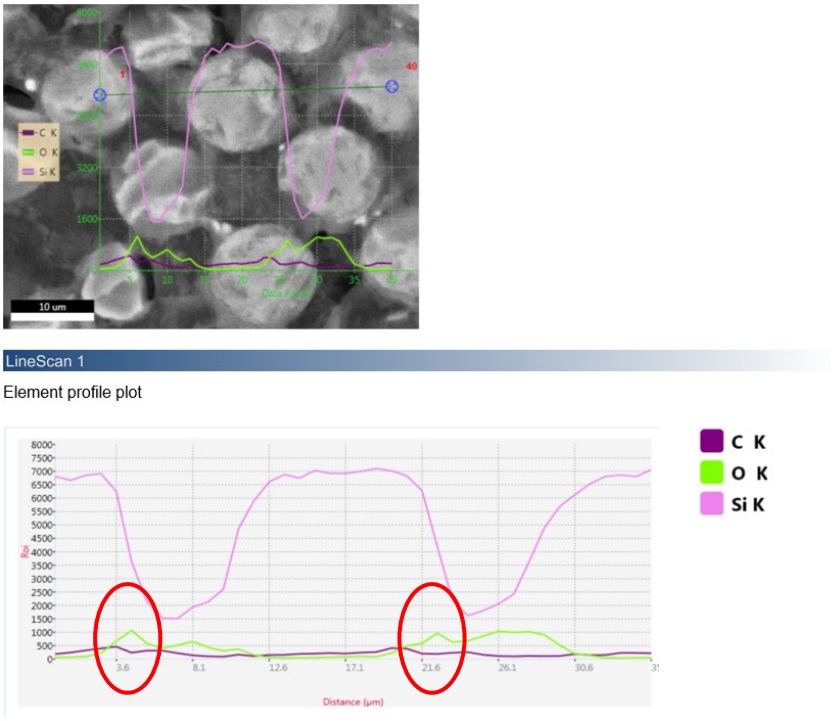

Figure 38: Line based EDX analysis of ZrC/ZTA coated sample exposed to 1000 °C for 1 h with increased oxygen content at the edge of fibres

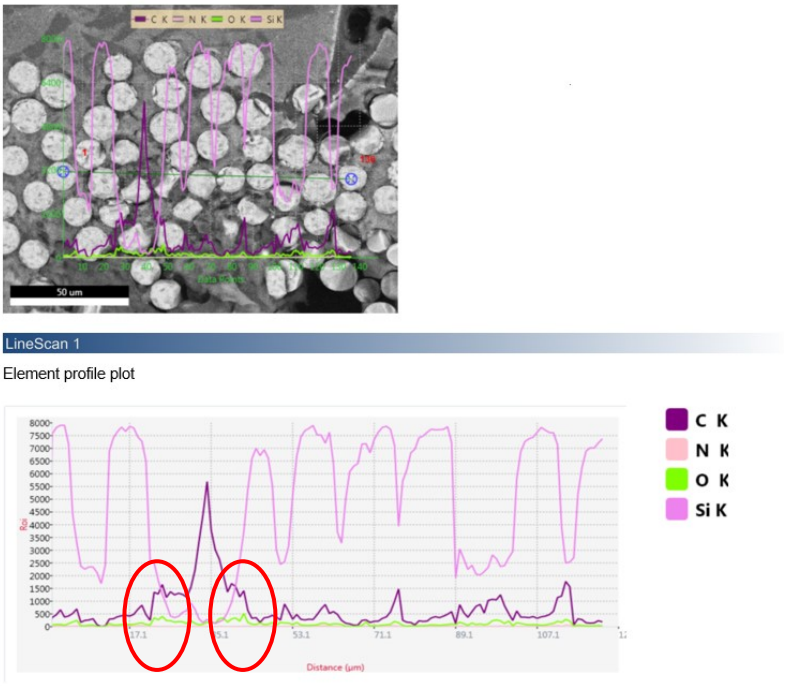

Figure 39: Line based EDX analysis of SiC/Si_3N_4/SiC coated sample exposed to 1000 °C for 1 h with increased oxygen content at the edge of fibres bordering a carbon rich zone

Based upon the results of the microstructural analysis it is apparent that the current coating parameters are producing discontinuous FMI coatings which are not effectively protecting the fibre phase from oxidation. Future work will focus on optimizing the BN/PSZ and SiC/Si_3N_4SiC coating parameters to achieve a more continuous FMI and thermogravimetric analysis testing the samples at high temperature for characterizing oxidation resistance imparted by the optimized coatings.

4.3.2 Optical Microscopy Examination of Coated Fibre Bundles

The results of the measured coating thicknesses for Batch 4 fibre bundles, with two particular coating schemes, are displayed in Figure 40 and Figure 41 with the data presented in Table 19 and Table 20.

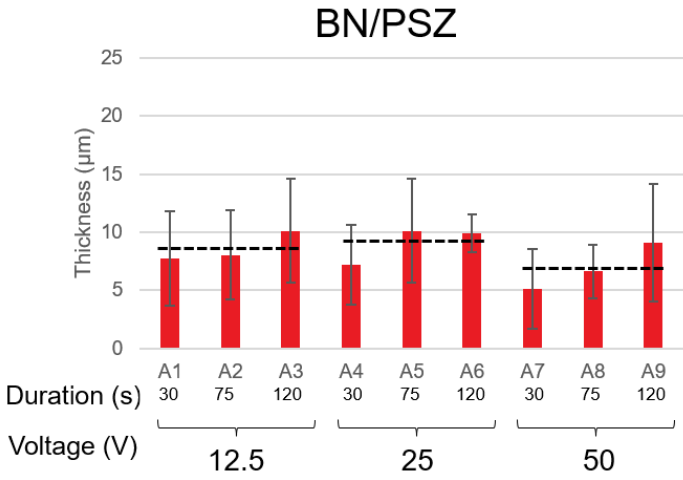

Figure 40: Coating Thicknesses of BN/PSZ coatings vs. deposition duration (s) and voltage (V)

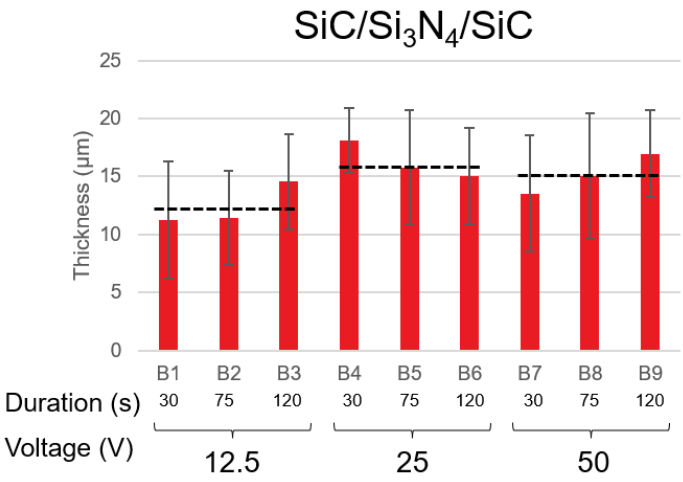

Figure 41: Coating Thicknesses of SiC/Si_3N_4/SiC coatings vs. deposition duration (s) and voltage (V)

Table 19: Measured Coating Thicknesses for Batch 4 - BN/PSZ Fibre Bundle Samples

Sample	Voltage (V)	Deposition Time (s)	Coating Thickness (µm)	Coating Thickness Standard Deviation (µm)
A1	12.5	30	7.74	4.09
A2	12.5	75	8.05	3.87
A3	12.5	120	10.13	4.50
A4	25	30	7.19	3.43
A5	25	75	10.11	4.49
A6	25	120	9.92	1.62
A7	50	30	5.11	3.43
A8	50	75	6.64	2.30
A9	50	120	9.09	5.10

Table 20: Measured Coating Thicknesses for Batch 4 - SiC/Si_3N_4/SiC Fibre Bundle Samples

Sample	Voltage (V)	Deposition Time (s)	Coating Thickness (µm)	Coating Thickness Standard Deviation (µm)
B1	12.5	30	11.24	5.08
B2	12.5	75	11.43	4.10
B3	12.5	120	14.56	4.14
B4	25	30	18.15	2.79
B5	25	75	15.79	4.90
B6	25	120	15.04	4.18
B7	50	30	13.53	5.01
B8	50	75	15.02	5.41
B9	50	120	16.97	3.73

It was envisioned that an increased voltage and deposition time will create a greater deposit build up which will in term result in a thicker coating layer based upon the mechanics of EPD (equations (28) and (29) on page 21). For BN/PSZ coating, this predication holds. However, it seems that the prolonged deposition time did not yield thicker SiC/Si_3N_4/SiC coating at 25V; in fact, the shorter duration produced the thickest coating of SiC/Si_3N_4/SiC. As only two cross sections for each sample were used and the cross sections are not always uniform, increased number of samples and number of sampling lines used for each fibre core in future work will help to better characterize the trend. However, it did point out one important aspect from this study, that is the non-uniformity of the coating layer. It can be seen in section 5.5 that the electric field

along the length of the fibre will vary with greater field strength expected near the top of the colloid and at the bottom of the electrode in comparison to the midpoint of the fibre.

Table 21: Change coating thickness results as a function of sampling lines

Sample	Number of Sampling Lines	Average Coating Thickness (µm)	Coating Thickness Standard Deviation (µm)
B4	4	18.15	2.79
B4	16	18.77	1.94

A more thorough examination of the coating thickness will include a progressive polishing step to reveal subsequent cross sections along equal depth intervals for characterization of coating thickness vs. fibre height. While every effort was made to ensure that the thresholding process was applied to capture only the coating phase, the tone-based process may have introduced some false-positive and false-negative pixels, leading to variation in thickness measurement. A solution to this issue for future work would be using a coloured epoxy for mounting then applying a colour-based thresholding filter to ensure the coating is well differentiated from the mounting puck. To examine the effect of using four profile lines rotating around the fibre centre in 90 ° increments as opposed to 16 lines rotating in 22.5 ° increments, the program was modified. Sample B4 was selected to test the difference as it had the lowest SD:Average ratio of all the samples, the results are given in Table 21. It can be seen that increasing the sampling line count doesn't alter the thickness range significantly. The averaged thickness increases slightly, likely as a result of coating gaps having a lower weight in the averaging in the case of 16 measurements.

5. Multiphysics Modeling of the EPD Process

COMSOL version 5.6 utilizing a 3D space and a stationary study was used in this study to model the electric field properties within the stationary electrodeposition cell.

5.1 COMSOL Model Geometry

Geometry representing an ideal stationary electrodeposition cell was created using the geometry interface within COMSOL as shown in Figure 42.

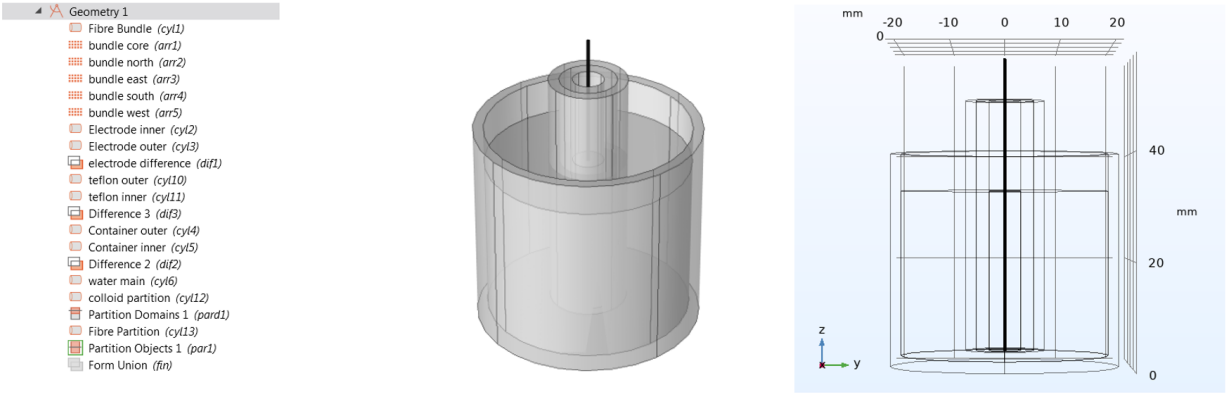

Figure 42: Model tree and geometry of stationary electrodeposition cell

The geometry consists of a fibre bundle, electrode shield, electrode, colloid, and colloid container. COMSOL allows geometries to be partitioned to assist in creating physics boundary conditions and meshing, two partitions were utilized with this geometry. The first partition separates the colloid surrounding the fibre bundle within the electrode to allow for a finer mesh to be generated within this area of interest. The second partition creates domains of the top 2 mm of each fibre to allow for the application of voltage to the fibre top. A 3D geometry was initially employed to allow for greater freedom in evaluating effects of fibre placements and non-symmetries within the model. A 2D or axisymmetric approach was considered should the computational time to resolve the simulation become burdensome to the work.

The fibre bundle consists of 489 cylindrical fibres of 14 μm diameter and 55 mm length. The fibres within the fibre bundle are arranged in five arrays to partially emulate the roundness of the fibre bundle in reality. The initial array consists of 17 x 17 fibres and forms the core of the fibre bundle, four additional arrays are arranged in the cardinal directions around the core, and each consist of 11 x 5 fibres for a total of 489 fibres in the bundle. The distance between each fibre centre is assigned the parameter of **df** which is originally

set at 0.02 mm but can be varied in a parametric study to examine whether the spacing between the fibres affects the field within the fibre bundle. The geometry representing an ideal fibre bundle is shown in Figure 43.

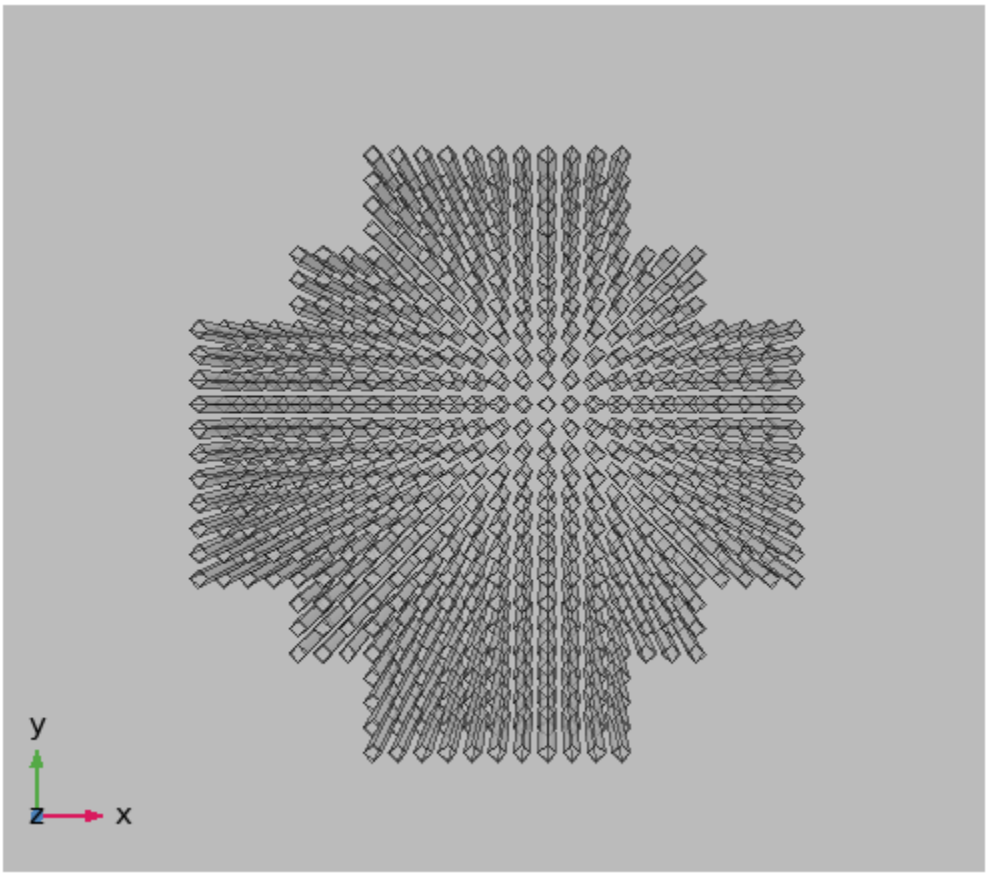

Figure 43: Fibre bundle array with a core of 17 x 17 fibres, and four cardinal arrays of 11 x 5 fibres

Note that the fibres are represented as diamonds in the geometry view because the length scale of the radius is several orders of magnitude lower than the length scale of the other geometrical features. The fibres regain their cylindrical shape during the meshing of the model.

5.2 COMSOL Materials

Five materials have been added to the model to assign material properties to the domains, these materials are shown in Figure 44.

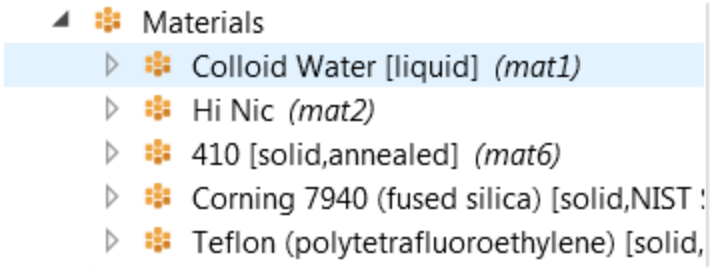

Figure 44: Materials assigned to stationary EPD model

Colloid Water and *Hi Nic* are custom materials which have been added to the model specifically for this work. The remaining three materials were taken from the COMSOL materials database, these materials are *Teflon (polytetrafluoroethylene)[solid,1.05mm thickness]* for the Teflon shield, *410[solid,annealed]* for the electrode, and *Corning 7940(fused silica)[solid,NIST 5006]* (Pyrex) for the container holding the colloid. The material properties of interest for this simulation are relative permittivity, relative permeability, and electrical conductivity.

	Property	Variabl	Value	Unit	Property group
✓	Relative permittivity	epsilo...	9	1	Basic
	Relative permeability	mur_is...	1	1	Basic
	Density	rho	2.7[g/c...	kg/m³	Basic
	Poisson's ratio	nu	.3	1	Basic
	Young's modulus	E	270[GPa]	Pa	Basic
	Electrical conductivity	sigma...	8.33E-7[...	S/m	Basic

Figure 45: Material properties of the custom material Hi Nic

✓	Relative permittivity	epsilo...	1	1
	Thermal conductivity	k_iso ;...	k(T[1/K]...	W/(m·...
	Resistivity	res_is...	res(T[1/...	Ω·m
	Coefficient of thermal expansi...	alpha...	(alpha(T...	1/K
	Heat capacity at constant pres...	Cp	C(T[1/K]...	J/(kg·K)
	Electrical conductivity	sigma...	sigma(T...	S/m
	Density	rho	rho(T[1/...	kg/m³

Figure 46: Material properties of 410 [solid, annealed]

For the *Hi Nic* custom material the relative permittivity was obtained from the work of Ishikawa [103], the relative permeability was set to 1 due to SiC being a non-magnetic material, the electrical conductivity was measured using a Fluke 87V multimeter with resistance values being measured in length increments of 10 mm (10 mm, 20 mm, 30 mm, etc.). Material properties for 410 stainless steel are obtained from the COMSOL materials database and expressed as piecewise equations, an example of the conductivity piecewise equation is shown in Figure 47.

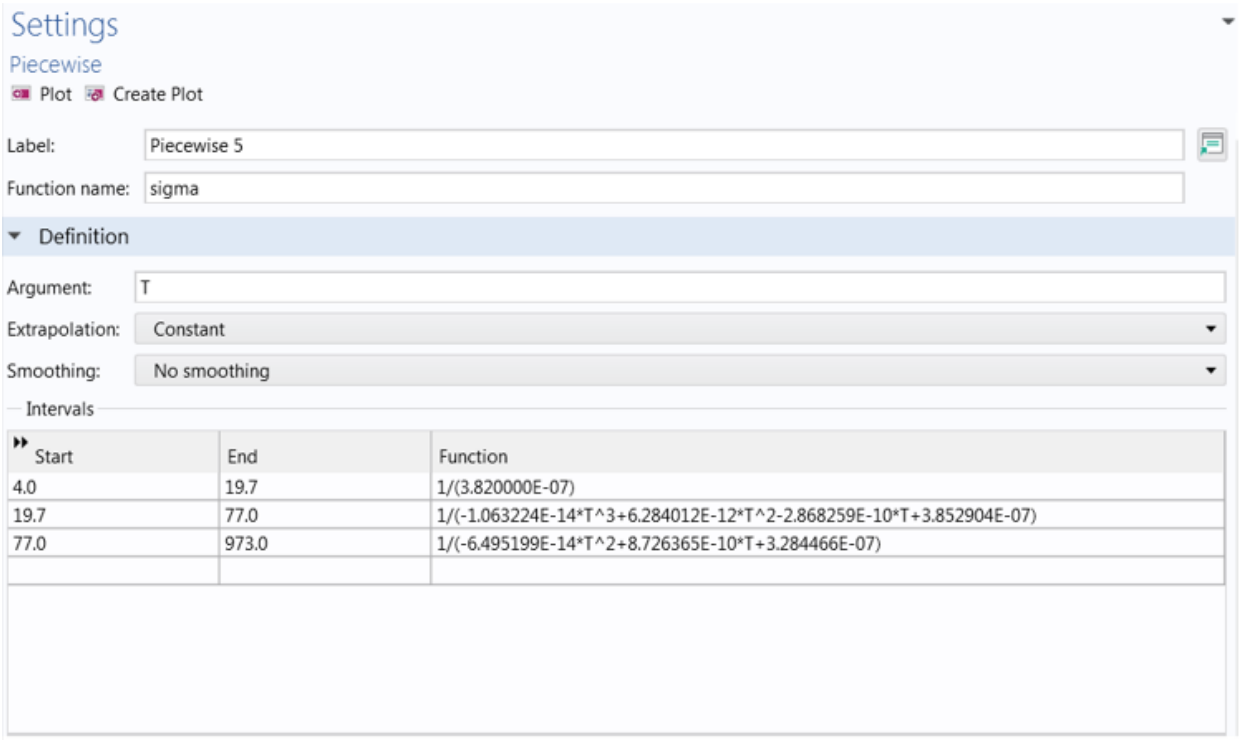

Figure 47: An example of a piecewise material property equation for conductivity, the conductivity of 410 stainless steel varies with T (Temperature)

Additional materials properties may be added to a material node if additional physics are added to the model in the future.

5.3 COMSOL Multiphysics Simulation

The AC/DC module was used to add the physics interface to this COMSOL module, specifically the electrostatics interface. Electrostatics is used to compute electric field, and potential distributions by solving Gauss' law (11) for electric field using scalar electric potential as the dependant variable.

$$\nabla \cdot \mathbf{E} = \frac{\varphi}{\varepsilon_r \varepsilon_0} \tag{48}$$

Where $\nabla \cdot \mathbf{E}$ is the divergence of the electric field, φ is the charge density, ε_r is the dielectric constant, and ε_0 is the permittivity of a perfect vacuum.

The boundary conditions imposed upon the model utilize two terminal junctions to specify an initial potential to the top of the electrode and the fibre tops domain. The initial potential for the fibre tops is **V_el**/2 and the initial potential for the electrode top is -**V_el**/2 where **V_el** is a parameter which can be varied during a parametric study.

5.4 COMSOL Meshing

A distributed mesh was utilized in this work to account for the significant variance in dimensions between the fibre phase and the remaining domains in the geometry. The first stage of meshing is to dictate a size function for the mesh which will be imposed on the fibre domain, this mesh is given a minimum element size of 0.002 mm, a free quad mesh is then applied to the surface of the fibre tops as seen in Figure 48.

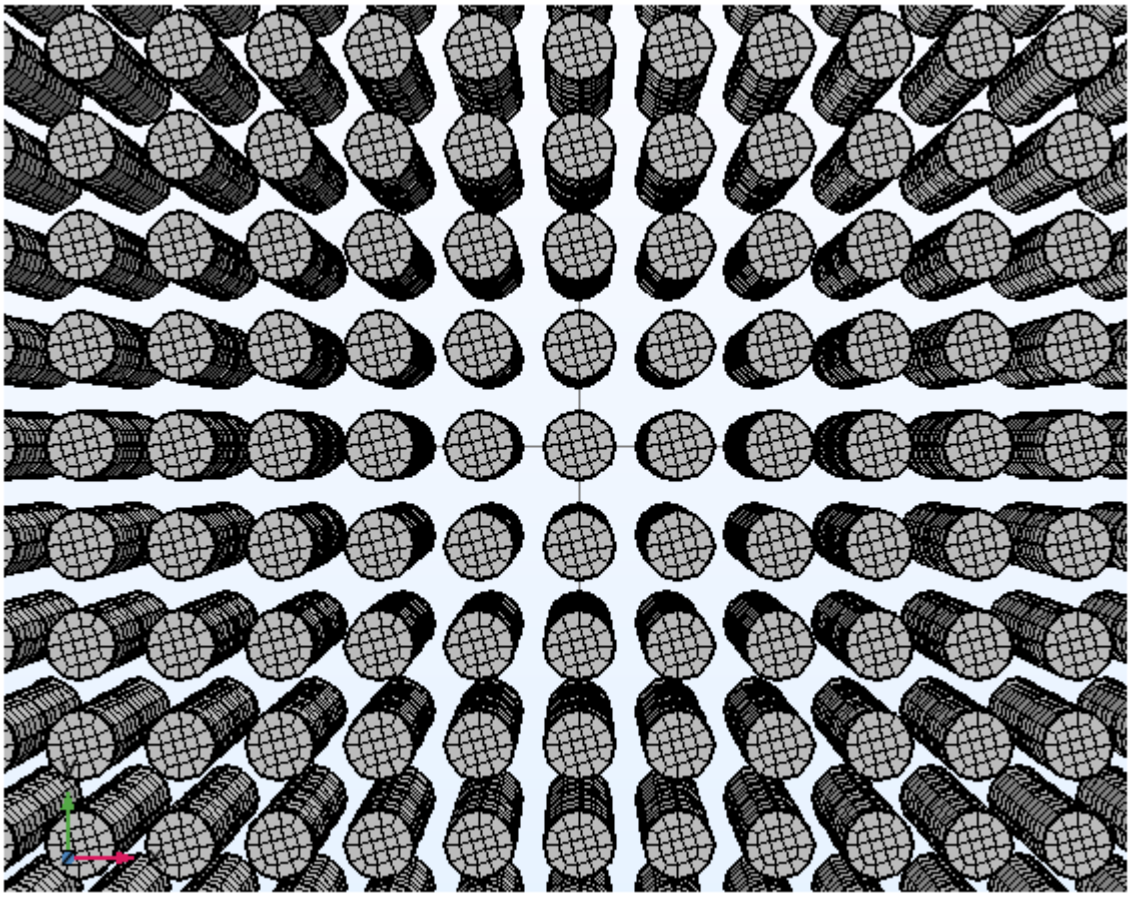

Figure 48: Free-quad mesh with minimal element size of 0.002 mm imposed on the surface of the fibre tops

The free-quad mesh is then swept down the fibre domain dividing the fibre length into 7 segments as seen in Figure 49, creating high aspect ratio computationally efficient elements for these high aspect ratio features.

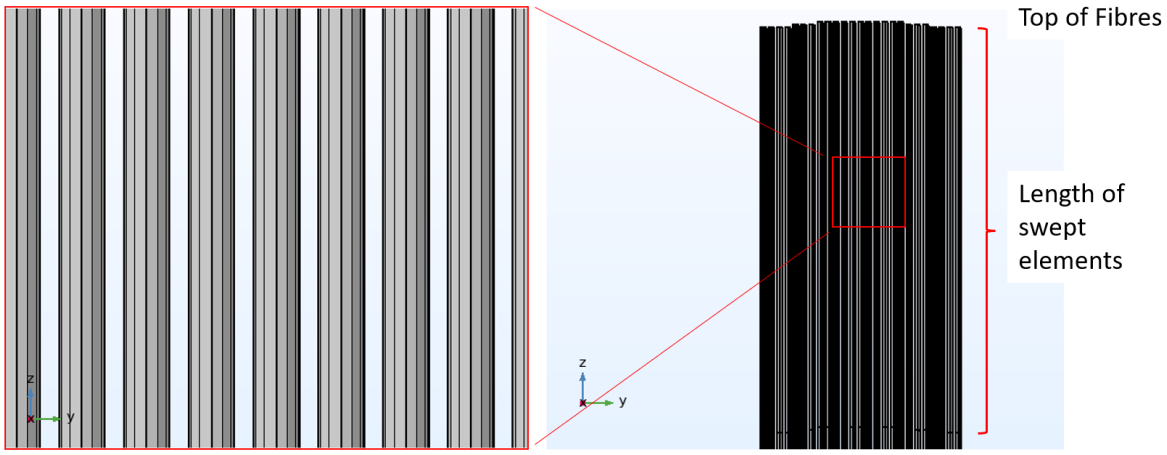

Figure 49: High aspect ratio swept elements covering the fibre domain

To mesh the colloid domain partition which covers the colloid contained within the electrode a boundary layer automated meshing feature is used to create elements along the surface boundary where the fibres emerge from the colloid as seen in Figure 50.

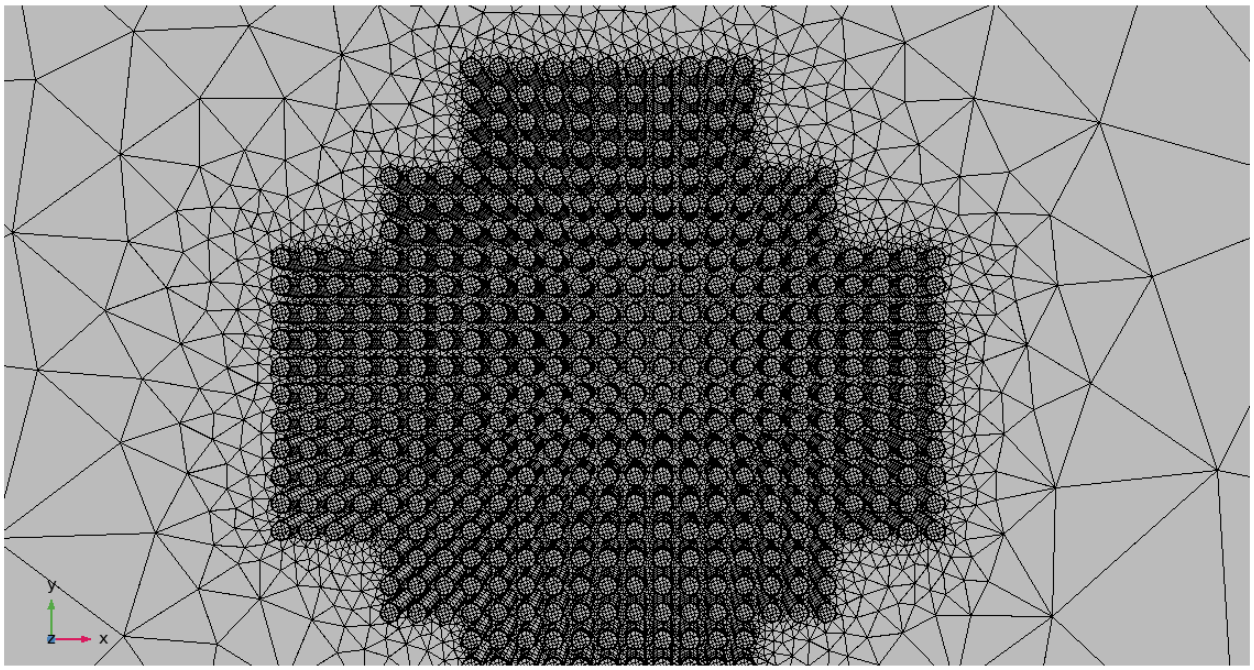

Figure 50: Boundary layer mesh along surface of colloid within electrode

The boundary layer meshing feature increases the density of the mesh in a normal direction along surfaces allowing for a finer resolution near surfaces. This mesh is advantageous for increasing the resolution in the complex are within the fibre bundle while reducing the computational cost for determining the electrical field in the greater colloid. Since the boundary layer feature is another mesh which is applied to a boundary as opposed to a domain the boundary layer must also be swept down the partitioned colloid domain. The remaining domains of the model are meshed using the automated free-tetrahedral meshing function. Three separate free-tetrahedral meshes are utilized to cover the remaining domains, a mesh with a 'fine' size distribution is applied to the electrode and electrode shield domains, a mesh with a 'normal' size distribution is applied to the remaining colloid and a mesh with a 'coarse' size distribution is applied to the container domain. The overall mesh can be seen in Figure 51.

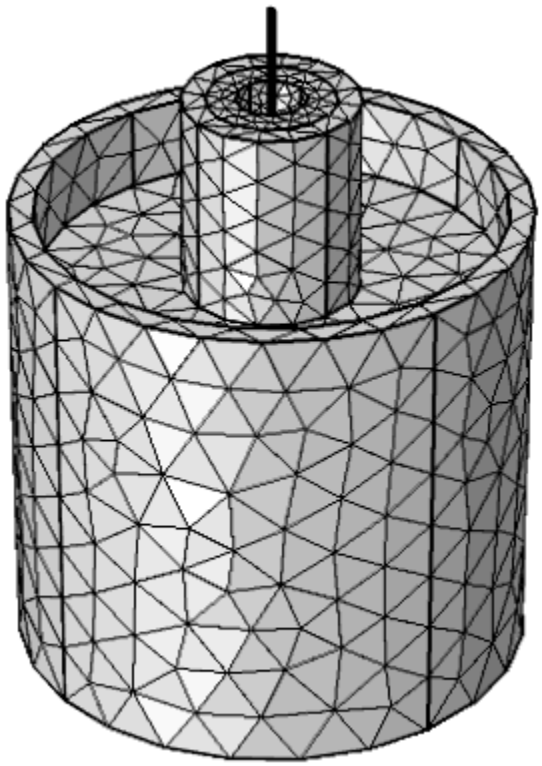

Figure 51: Meshed stationary EPD cell

In total there are 627397 elements generated for the mesh with a specific breakdown of element type given in Figure 52. At this point in the study the meshing was not varied to check for mesh effects upon the results, this process will be performed in future work.

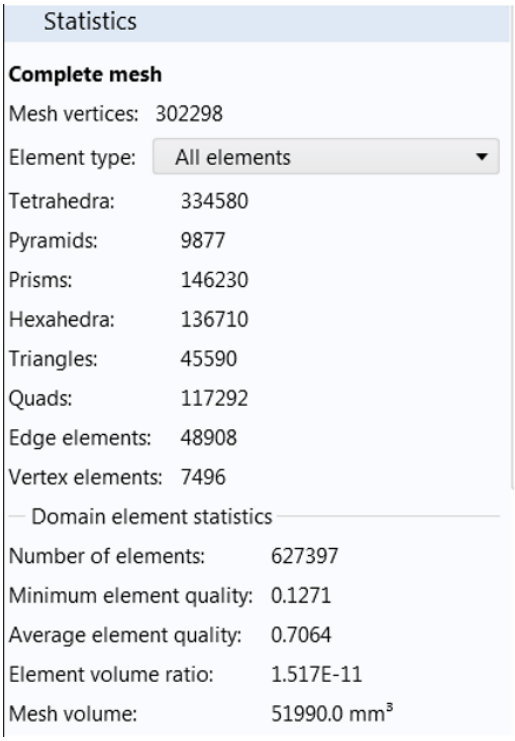

Figure 52: Breakdown of the FEA elements used to model the electrostatic properties of the stationary EPD cell

5.5 Results and Guidance for Future Studies

An initial stationary study was computed to examine the electric field using baseline parameters of 50 V electric potential, a centred fibre bundle, and 0.02 mm spacing between fibre centres. This study represents an ideal case for the EPD of ceramic powders on the fibre bundle in a stationary EPD cell. The overall electric field within the colloid has been calculated using a root mean squared averaging of each vector component of the electric field and plotted along an y-z plane sliced through the centre of the colloid as seen in Figure 53 with electric potential of the system shown in Figure 54.

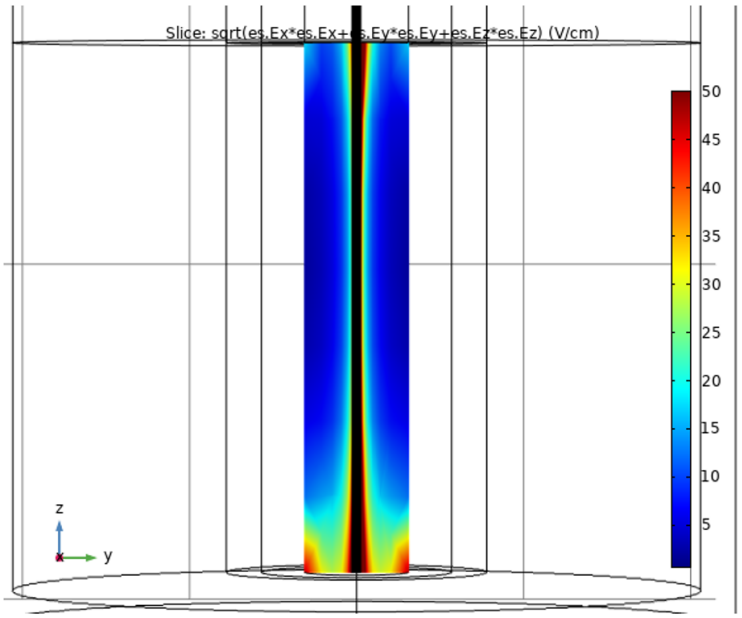

Figure 53: Electric field (V/cm) through the colloid within the electrode using baseline parameters (V_el = 50 V, df = 0.02 mm, OS = 0 mm)

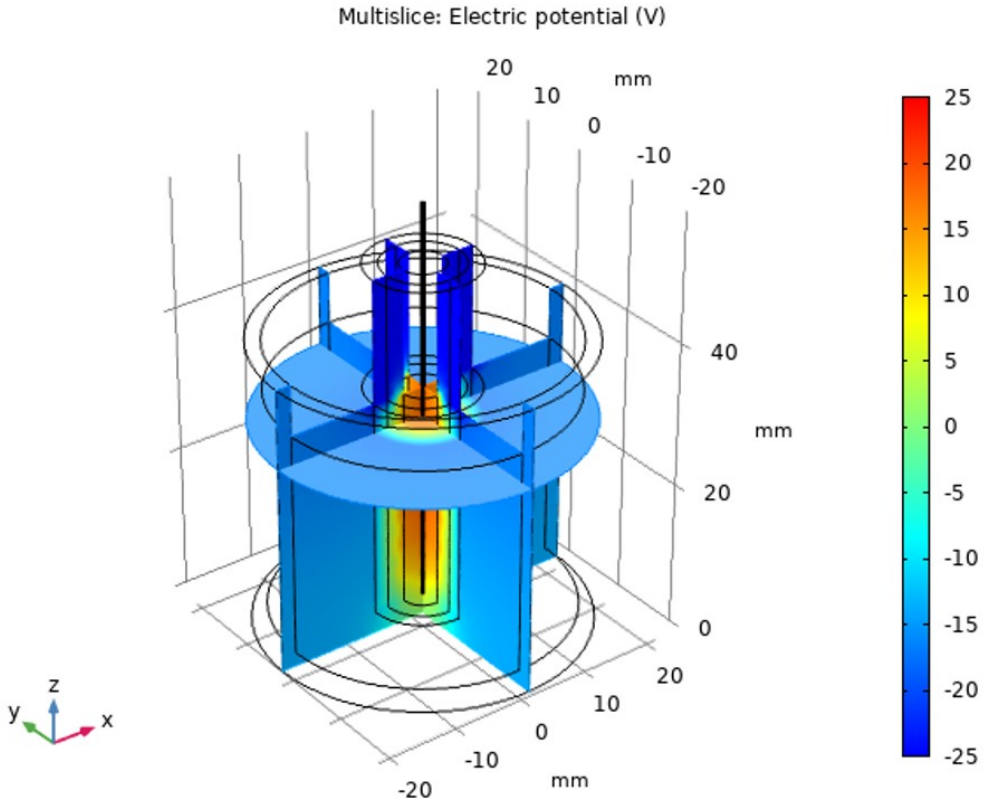

Figure 54: Electric Potential (V) of stationary EPD cell using baseline parameters (V_el = 50 V, df = 0.02 mm, OS = 0 mm)

Three stationary studies using parametric sweeps were computed to examine the effect of varying the voltage, the location of the fibre bundle centre, and the intra-bundle fibre spacing. Each of these parametric variables is examined for their effect on the electric field within the colloid as well as the value of the electric field seen at the surface of a fibre at the edge of the fibre bundle and a fibre in the centre of the fibre bundle.

5.5.1 Voltage

The simplest parametric study involves examining the effect of different applied voltage levels upon the electric field within the EPD cell. This parametric study is also most aligned with the variance of conditions used to coat fibre bundles in section 3.2. Three voltage levels (12.5 V, 25 V, and 50 V) were specified to correspond with the voltage levels used for the 3^2 full factorial design (Table 8).

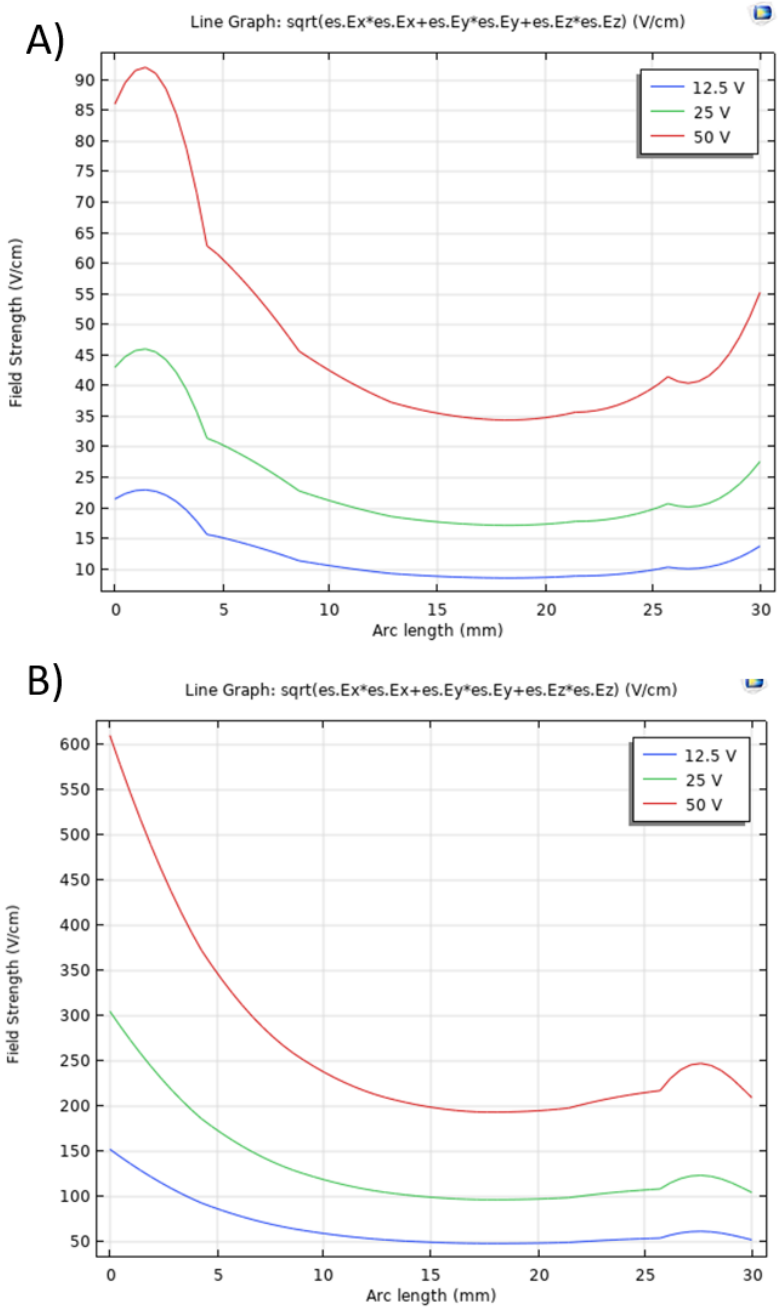

Figure 55:Electric Field Strength with varying voltages at the surface of A) a fibre located on the outside of the fibre bundle B) a fibre located at the centre of the bundle where arc length measures distance of the fibre from the bottom of the electrode to the top of the colloid

As expected, reduced electric potential results in lower values for electric field at the surface of the fibre. It is remarkable to see that there is a significant variance of the electric field at the base of the fibre vs. the core of the fibre. For the 50 V condition, the base of the fibre will be exposed to nearly 3x the electric field

than the position15 mm up the fibre; this inevitably would have an effect on the coating thickness and properties. Indeed, the differences in coating thickness in different locations were observed. Another result of note is the difference of electric field seen by fibres in the core of the bundle as opposed to fibres at the outer edge of the bundle. Based on this result it would be envisioned that the fibres at the centre of the fibre bundle would preferentially coat faster than fibres at the edge of the bundle, however, microscopic evaluations of coated fibre bundles have not borne this observation out. It is a much more common observation that outer fibres are more heavily coated than inner fibres in the bundles that have been inspected. Combined the experimental results with that from the COMSOL simulation, it realized that at least two factors are at play: the electric field (driving force) and also the transport of the particulate materials (rate). As EPD is a transport based process, in order for ceramic particles to coat inner fibres they need to be able to travel under the applied electric field to the vicinity of the inner fibres without first coating the outer fibres.

5.5.2 Fibre Bundle Centre Offset

When placing the fibre bundle into the stationary EPD it was not an uncommon occurrence for the bundle to contact the Teflon shield as it is being inserted into the EPD cell; this is especially the case if the fibre has been wetted, as capillary effects will lead to the fibre bundle becoming attached to the Teflon shield. A study with a parametric sweep while placing the centre of the fibre bundle with a y-position offset 0, 0.1 cm, and 0.2 cm was conducted to examine the effect of a non-symmetrical placement on the electric field at the surface of fibres. A fibre in the centre of the fibre bundle and a fibre at the edge of the bundle nearest to the Teflon shield were selected for a closer examination of the electric field at their inner and outer edges (Figure 57).

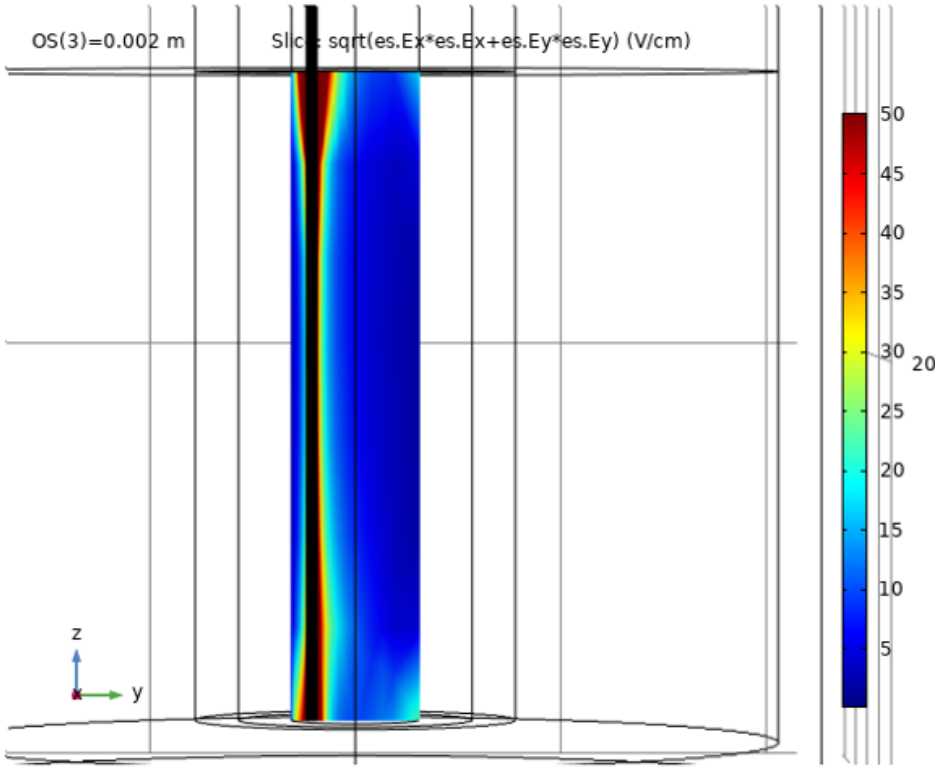

Figure 56: Electric field (V/cm) through the colloid within the electrode with a fibre bundle centre offset of 0.2 cm

An examination of Figure 56 reveals that there is a slight distortion of the electric field surrounding the fibre bundle based upon the centre offset, leading to stronger electric field on the side of the fibre bundle furthest from the Teflon shield, as further illustrated in Figure 52.

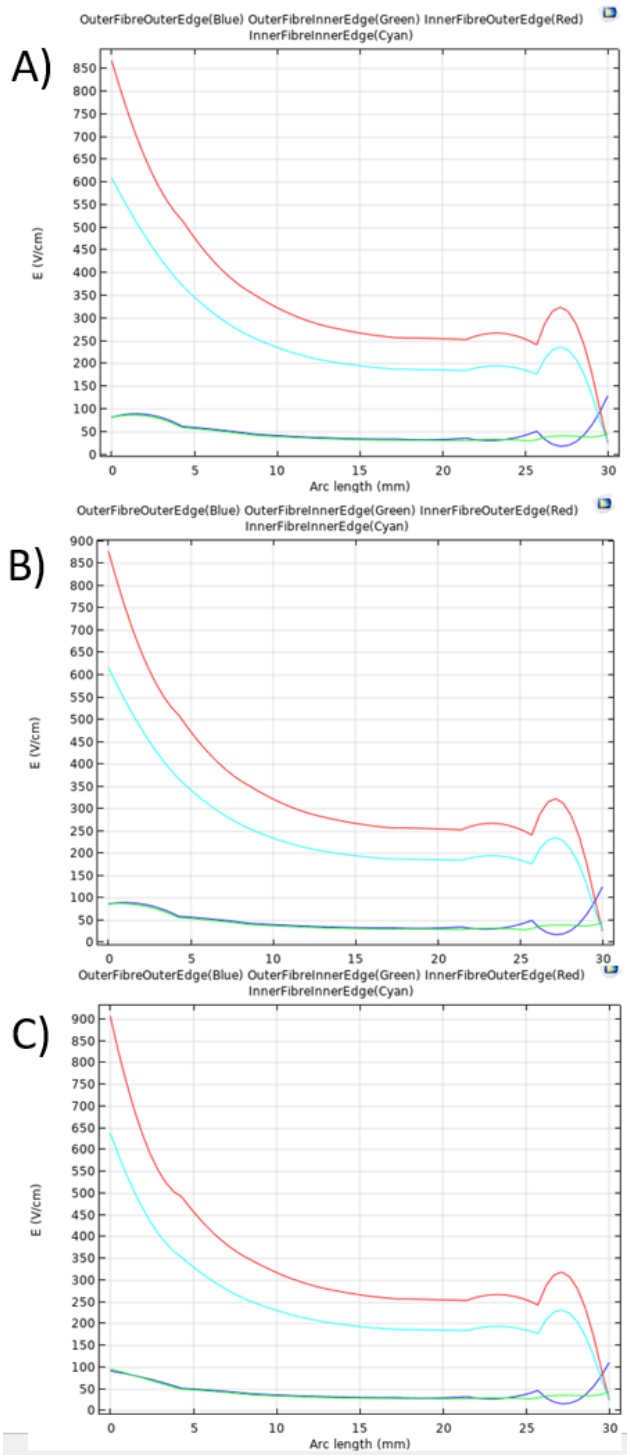

Figure 57: Electric Field Strength with varying fibre bundle offsets where arc length measures distance of the fibre from the bottom of the electrode to the top of the colloid, Red and Cyan line are outer and inner edge of an inner bundle fibre respectively; Blue and Green line are outer and inner edge of an outer fibre A) no offset B) 0.1 cm offset C) 0.2 cm offset

Further examining the electric field at the surface of the fibres, it shows a minimal alteration of the field profile along the fibre length as the offset increases, the greatest difference between the three parametric studies is an increasing magnitude of field strength near the inner fibre as the offset increases. However, this magnitude increase is not significant when compared to the overall field strength along the fibre length.

5.5.3 Intra-Bundle Fibre Spacing

It is challenging to control the separation of fibres within the stationary EPD cell; however, it is of interest to examine the effect of separating the fibres within the bundle with the view of designing an EPD cell that allows for the spreading of fibres as they enter the colloid. A potential benefit of a cell that allows the separation of the fibres is the improved uniformity of the powder within the colloid to access the internal fibres. For this parametric sweep the distance between fibre centres within the bundle was set to 20 μm, 40 μm, and 80 μm. Based on the results presented in Figure 58 increasing the spacing between fibre centres of the fibre bundle has the greatest effect on fibres in terms of the potential at the centre of the bundle. Overall, increased spacing reduces the magnitude of the electric field seen at the fibre surface of the inner fibres, and reduces the difference between the inner edge and outer edge of the fibre at the centre of the bundle. Also, by increasing the spacing, the particulates will have increased access of the inner fibres, contributing to more uniform coatings.

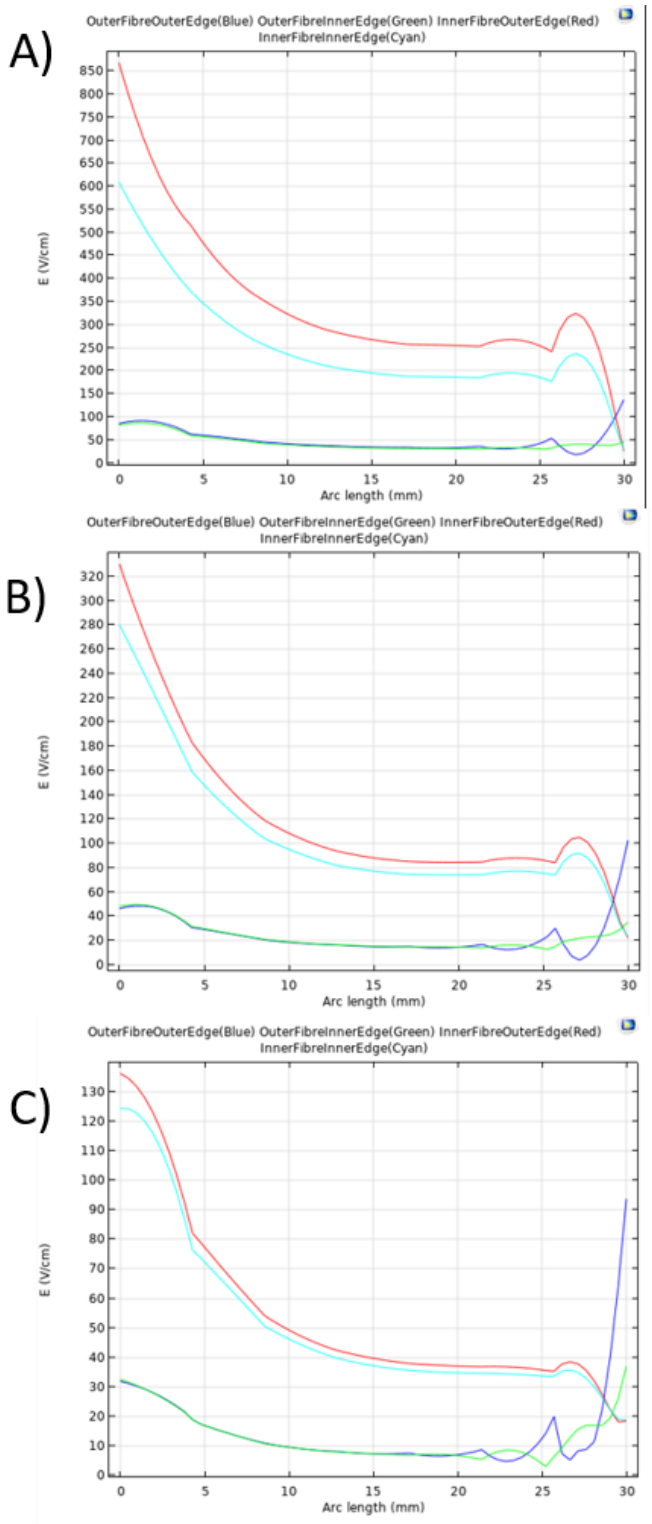

Figure 58: Electric Field Strength with varying distance between fibre centres (df) where arc length measures distance of the fibre from the bottom of the electrode to the top of the colloid, Red and Cyan line are outer and inner edge of an inner bundle fibre respectively; Blue and Green line are outer and inner edge of an outer fibre A) df = 0.02 mm B) df = 0.04 mm C) df = 0.08 mm

5.5.4 Stationary EPD Cell with No Teflon Shield

The final test case explored with this COMSOL simulation setup is the removal of the Teflon shield. The Teflon shield was included in the EPD setup to prevent the accidental contact between the charged fibres and the charged electrode. In a water-based EPD setup contact will potentially lead to heating of the fibre phase as current increases; however, in a non-polar solvent EPD setup such as one using ethanol there is potential for dangerous arcing between the fibre and electrode leading to explosions.

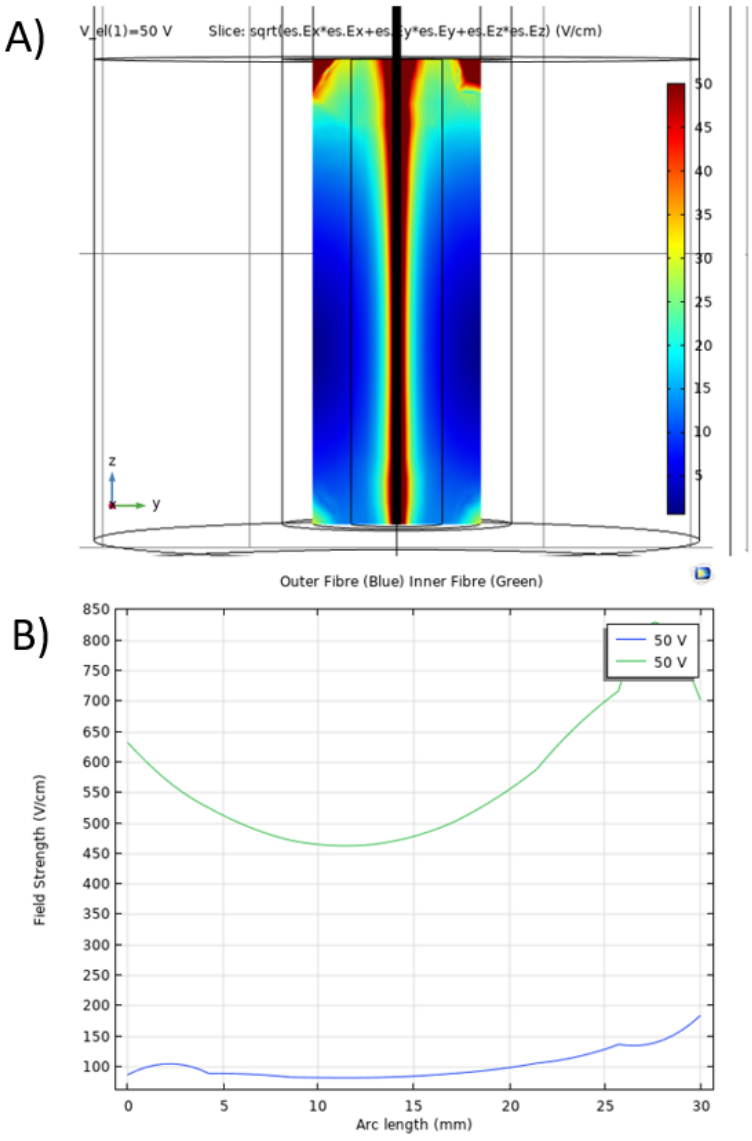

Figure 59: A) Electric field (V/cm) through the colloid within the electrode without a Teflon shield B) Electric Field Strength along length of an inner (Green) and outer (Blue) arc length measures distance of the fibre from the bottom of the electrode to the top of the colloid

Based upon the significant differences (600V/cm at fibre bottom vs. 200 V/cm at fibre position 15 mm for an inner fibre, Figure 55B) observed in the modeled electric field at the bottom of the fibre in comparison with the centre of the fibre it was decided to conduct a simulation where the material of the Teflon shield was changed to match the water phase effectively removing the shield. The results are displayed in Figure 59. The removal of the Teflon shield results in a more uniform distribution of the electric field along the fibre length, especially for the inner fibre; however, the greatest extent of electric field is now seen near the top of the fibre. Based upon these results it may be possible to design an optimized shield which creates a more uniform distribution of electric field across the length of the fibre to improve the uniformity of the coating.

6. Conclusions and Recommendations

6.1 Conclusions

- EPD setup deposits ceramic nanopowder onto SiC fibre bundles
- Four fibre coating combinations initially evaluated in tensile testing at room temperature and tensile testing at room temperature following exposure to standard atmosphere at 1000 °C for 1 h
    - Al_2O_3/SiC, BN/PSZ, ZrC/ZTA, SiC/Si_3N_4/SiC were the four coatings
    - ZrC/ZTA and SiC/Si_3N_4/SiC demonstrated best tensile properties at room temperature
    - SEM evaluation revealed more uniform coating layers on ZrC/ZTA and SiC/Si_3N_4/SiC samples
    - BN/PSZ and SiC/Si_3N_4/SiC demonstrated best tensile strength retention following high temperature exposure
    - SEM evaluation revealed less fibre degradation in BN/PSZ and SiC/Si_3N_4/SiC samples following high temperature exposure
- BN/PSZ and SiC/Si_3N_4/SiC samples were fabricated for high temperature tensile tests
    - High temperature adhesive degraded matrix phase of microcomposites preventing evaluation of high temperature tensile properties
    - Optical microscopy indicated that coating thickness generally increases with deposition duration, 25 V had greatest deposition efficiency
- FEA modeling utilized to evaluate electric field for stationary EPD setup
    - Variations in field strength along the fibre axis as well as between fibres on the inside of the fibre bundle and outside of the fibre bundle are predicted
    - Increased spacing between fibres and removal or modification of Teflon shield reduces this variation

6.2 Future Work

1) Progressive polishing and optical microscopy of coated fibre bundles to characterize fibre coating thickness variations along the fibre axis with colouring of epoxy system to improve accuracy of thresholding technique
2) Redesign of EPD stationary cell to improve electric field uniformity across fibre length and encourage spreading of fibres from fibre bundle
3) Application of EPD setup to a fibre reel wherein the fibre is drawn from the colloid bath to incorporate dip coating deposition process to EPD process and allow for the continuous coating of fibre reels
4) Addition of deposit layer to COMSOL FEA model to include added resistance of deposited layer to electric field calculation
5) Addition of deposition layer growth physics to COMSOL FEA model to create time dependant simulation feature for modeling deposition layer growth
6) Fabrication of microcomposites using a PIP method and characterization of tensile properties
7) Thermogravimetric analysis of coated fibre bundles to compare environmental protection potential of coatings
8) Exploration of potential bond coats to protect microcomposites from high temperature adhesive to enable high temperature microcomposite testing
9) Determination of a characterization technique which can be utilized for determining residual stresses in sintered fibre coatings
10) Fabrication of 2D CMC layups following procedures established for microcomposites to produce dog-bone samples for tensile characterization and high temperature tensile characterization

Appendix A: References

[1] J. Hutchinson and H. Jensen, "Models of Fiber Debonding and Pullout in Brittle Composites with Friction," *Mechanics of Materials,* vol. 9, pp. 139-163, 1990.

[2] W. Callister and D. Rethwisch, Materials science and engineering: an introduction, Wiley, 2007.

[3] P. N. Bansal, Handbook of Ceramic Composites, Kluwer Academic Publishers, 2005.

[4] M. P. Boyce, Gas turbine engineering handbook, Butterworth-Heinemann, 2012.

[5] P. Schilke, "Advanced Gas Turbine Materials and Coatings," General Electric, 2004. [Online]. Available: http://site.ge-energy.com/prod_serv/products/tech_docs/en/downloads/ger3569g.pdf.

[Accessed 03 2015].

[6] B. Heidenreich, "C/SiC and C/C - SiC Composites," in *Ceramic Matrix Composites: Materials, Modeling and Technology*, Hoboken, NJ, John Wiley & Soncs, Inc., 2015, pp. 147-216.

[7] A. F. McLean and E. A. Fisher, "Brittle Materials Design, High Temperature Gas Turbine," Defense Advanced Research Projects Agency, Watertown Mass., 1981.

[8] G. Nehls, "Composites World," Gardner Business Media Inc., 21 8 2021. [Online]. Available: https://www.compositesworld.com/news/ge-aviation-reaches-advanced-manufacturing-milestone-for-cmc-and-am-jet-engine-components. [Accessed 12 7 2022].

[9] O. Flores, R. Bordia, D. Nestler, W. Kernkel and G. Motz, "Ceramic Fibers Based on SiC and SiCN Systems: Current Research, Development, and Commercial Status," *Engineering Materials,* vol. 16, no. 6, pp. 621-636, 2014.

[10] M. Leuchs, Ceramic Matrix Composites: CVI, John Wiley & Sons, Inc., 2012.

[11] G. Corman and K. Luthra, "Silicon melt infiltrated ceramic composites (HiPerCompTM)," in *Handbook of Ceramic Composites*, Boston, Kluwer Academic Publishers, 2005, pp. 99-115.

[12] D. Zhu, "Aerospace ceramic materials: thermal, environmental barrier coatings for SiC/SiC ceramic matrix composites for turbine engien applications," *Journal of Materials Science and Technology,* vol. 35, no. 5, pp. 833-851, 2019.

[13] P. Mallilck, Fiber-reinforced composites: materials, manufacturing, and design, CRC Press, 2007.

[14] J. Lamon, "Influence of Interfaces and Interphases on the Mechanical Behavior of Fiber-Reinforced Ceramic Matrix Composites," in *Ceramic Matrix Composites: Materials, Modeling and Technology*, Hoboken, New Jersey, John Wiley & Sons, Inc., 2015, pp. 40-64.

[15] D. Koch, K. Tushtev, J. Horvath, R. Knoche and G. Grathwohl, "Evaluation of mechanical properties and comprehensive modeling of CMC with stiff and weak matrices," *Advances in Science and Technology,* vol. 45, pp. 1435-1443, 2006.

[16] M. Gerenda's, Y. Cadoret, C. Wilhelmi, T. Machry, R. Knoche, T. Behrendt, T. Aumeier, S. Denis, J. Goering, D. Koch and K. Tushtev, "Improvement of Oxide/Oxide CMC and Development of Combustor and Turbine Components in HiPOC Program," in *Turbo Expo: Power for Land, Air, and Sea*, Vancouver, Canada, 2011.

[17] K. Faber, "Ceramic Composite Interfaces: Properties and Design," *Annual Review of Materials Science,* vol. 27, pp. 449-524, 1997.

[18] J. DiCarlo and H.-M. Yun, "Non-oxide (Silicon Carbide) Fibers," in *Handbook of Ceramic Matrix Composites*, Boston, Kluwer Academic Publishers, 2005, pp. 33-55.

[19] A. Bunsell, "Oxide Fibers," in *Handbook of Ceramic Matrix Composites*, Boston, Kluwer Academic Publishers, 2005, pp. 3-33.

[20] K. Morishita, S. Ochiai, H. Okuda, T. Ishikawa, M. Sato and T. Inoue, "Fracture toughness of a crystalline silicon carbide fiber (Tyranno-SA3)," *Journal of the American Ceramic Society,* vol. 89, pp. 2571-2576, 2006.

[21] J. Lamon, S. Mazerat and M. R'Mili, "Reinforcement of Ceramic Matrix Composites: Properties of SiC-Based Filaments and Tows," in *Ceramic Matrix Composites: Materials, Modeling and Technology*, Hoboken, NJ, John Wiley & Sons, Inc., 2015, pp. 3-26.

[22] "ASTM Standard C1239-13: Standard Practice for Reporting Uniaxial Strength Data and Estimating Weibull Distribution Parameters for Advanced Ceramics," ASTM International, West

Conshohocken, 2013.

[23] "ASTM Standard C1683-10(2015): Standard Practice for Size Scaling of Tensile Strengths Using Weibull Statistics for Advanced Ceramics," ASTM International, West Conshohocken, 2015.

[24] S. Robertson, K. Sprinkle and M. Ruggles-Wrenn, "Testing Advanced SiC Fiber Tows at Elevated Temperature in Silicic Acid-Saturated Steam," in *ASME Turbo Expo 2017: Turbomachinery Technical Conference and Exposition*, Charlotte, NC, 2017.

[25] Y. Gogotsi and M. Yoshimura, "Oxidation and properties degredation of SiC fibers below 850 C," *Journal of Materials Science Letters,* vol. 13, pp. 680-683, 1994.

[26] W. Gauthier, F. Pailler, J. Lamon and R. Pailler, "Oxidation of silicon carbide fibers during static fatigue in air at intermediate temperatures," *Journal of the American Ceramic Society,* vol. 92, pp. 2067-2073, 2009.

[27] D. Mocaer, R. Pailler, R. Naslain, C. Richard, J. Pillot, J. Dunogues, C. Gerardin and F. Taulelle, "Si-CN ceramics with a high microstructural stability elaborated from the pyrolysis of new polycarbosilazane precursors," *Journal of materials science,* vol. 28, pp. 2615-2631, 1993.

[28] J. DiCarlo, "Advances in SiC/SiC Composites for Aero-Propulsion," in *Ceramic Matrix Composites: Materials, Modeling and Technology*, Hoboken, NJ, John Wiley & Sons, Inc., 2015, pp. 217-235.

[29] S. Zhu, M. Mizuno, Y. Kagawa and Y. Mutoh, "Monotonic tension, fatigue and creep behavior of SiC-fiber-reinforced SiC-matrix composites: a review," *Composites Science and Technology,* vol. 59, pp. 833-851, 1999.

[30] Y. Katoh, L. Snead, C. H. Jr., T. Nozawa, T. Hinoki, A. Ivekovic, S. Novak and S. G. d. Vincente, "Current status and recent research achievements in SiC/SiC," *Journal of Nuclear Materials,* vol. 455, pp. 387-397, 2014.

[31] J. Lamon, "Chemical Vapor Infiltrated SiC/SiC Composites (CVI SiC/SiC)," in *Handbook of Ceramic Composites*, Boston, Kluwer Academic Publishers, 2005, pp. 55-76.

[32] F. Rebillat, J. Lamon and A. Guette, "The concept of a strong interface applied to SiC/SiC composites with a BN interphase," *Acta Materialia,* vol. 48, pp. 4609-4618, 2000.

[33] N. Jacobson, G. Morscher and D. Bryant, "High-Temperature Oxidation of Boron Nitride: II, Boron Nitride Layers in Composites," *Journal of the American Ceramic Society,* vol. 82, pp. 1473-1482, 1999.

[34] G. Morscher, J. Hurst and D. Brewer, "Intermediate Temperature Stress Rupture of a Woven Hi-Nicalon BN-Interphase, SiC Matrix Composite in Air," *Journal of the American Ceramic Society,* vol. 83, pp. 1441-1449, 2000.

[35] H. Liu, H. Cheng, J. Wang and G. Tang, "Dielectric properties of the SiC fiber-reinforced SiC matrix composites with the CVD SiC interphases," *Journal of Alloys and Compounds,* vol. 491, pp. 248-251, 2010.

[36] A. Kohyama, J.-S. Park and H.-C. Jung, "Advanced SiC fibers and SiC/SiC composites towards industrialization," *Journal of Nuclear Materials,* vol. 417, pp. 340-343, 2011.

[37] J. Solti, S. Mall and D. Robertson, "Modeling Damage in Unidirectional Ceramic Matrix Composites," *Composites Science and Technology,* vol. 54, pp. 55-66, 1995.

[38] M. Moevus, D. Rouby, N. Godin, M. R'Mili, P. Reynaud, G. Fantozzi and G. Farizy, "Analysis of damage mechanisms and associated acoustic emission in two SiC/[Si-B-C] composites exhibiting

different tensile behaviours. Part I: Damage patterns and acoustic emission activity," *Composites and Science Technology,* vol. 68, pp. 1250-1257, 2008.

[39] W. Feng, L. Zhang, Y. Liu, X. Li, L. Cheng and B. Chen, "Thermal and mechanical properties of SiC/SiC-CNTs composites fabricated by CVI combined with electrophoretic deposition," *Materials Science and Engineering: A,* Vols. 500-504, p. 626, 2015.

[40] P. Boisse, "Textile Reinforcements: Architecture, Mechanical Behavior, and Forming," in *Ceramic Matrix Composites: Materials, Modeling and Technology*, Hoboken NJ, John Wiley & Sons, Inc., 2015, pp. 65-86.

[41] R. Sambell, D. Bowen and D. Phillips, "Carbon fibre composites with ceramic and glass matrices," *Journal of Material Science,* vol. 7, pp. 663-675, 1972.

[42] S. Pompidou and J. Lamon, "Analysis of crack deviation in ceramic matrix composites and multilayers based on the Cook and Gordon mechanism," *Composites Science and Technology,* vol. 67, no. 10, pp. 2052-2060, 2007.

[43] H. He and H. J.W., *Journal of Applied Mechanics,* vol. 56, pp. 270-278, 1989.

[44] N. Lissart and J. Lamon, "Damage and Failure in Ceramic Matrix Minicomposites: Experimental Study and Model," *Acta Materiallia,* vol. 45, no. 3, pp. 1025-1044, 1997.

[45] A. Evans, J.-M. Domergue and E. Vagaggini, "Methodology for Relating the Tensile Constitutive Behavior of Ceramic-Matrix Composites to Constituent Properties," *Journal of the American Ceramic Society,* vol. 77, no. 6, pp. 1425-1435, 1994.

[46] J. Cook and J. E. Gordon, "A mechanism for the control of crack propagation in all-brittle systems," *Proceedings of the Royal Society,* vol. 28A, pp. 508-520, 1964.

[47] D. B. Marshall, M. C. Shaw and W. L. Morris, "Measurement of Interfacial Debonding and Sliding Resistance in Fiber Reinforced Intermetallics," *Acta Materialia,* vol. 40, no. 3, pp. 443-454, 1992.

[48] P. D. Jero and R. J. Kerans, "The contribution of interfacial roughness to sliding friction of ceramic fibers in a glass matrix," *Scripta Metallurgia et Materialia,* vol. 24, no. 12, pp. 2315-2318, 1990.

[49] R. J. Kerans and T. A. Parthasarathy, "Theoretical analysis of the fiber pullout and pushout tests," *Journal of the American Ceramic Society,* vol. 74, no. 7, pp. 1585-1596, 1991.

[50] Y. Xu and X.-T. Yan, Chemical Vapour Deposition: An Integrated Engineering Design for Advanced Materials, London: Springer, 2010.

[51] A. Zinn and D. Scott, "Low Temperature Metal Oxide Coating Formation". USA Patent US 6921707 B1, 26 Jun 2005.

[52] R. Naslain, O. Dugne, A. Guette, J. Sevely, C. Brosse, J.-P. Rocher and J. Cotteret, "Boron Nitride Interphase in Ceramic-Matrix Composites," *Journal of the American Ceramic Society,* vol. 74, no. 10, pp. 2482-2488, 1991.

[53] C. Brinker, G. Frye, A. Hurd and C. Ashley, "Fundamentals of Sol-Gel Dip Coating," *Thin Solid Films,* vol. 201, pp. 97-108, 1991.

[54] H. Hamaker, "Formation of deposition by electrophoresis," *Transcript of the Faraday Society,* vol. 36, pp. 279-283, 1940.

[55] L. Besra and M. Liu, "A review on fundamentals and applications of electrophoretic deposition (EPD)," *Progress in Materials Science,* vol. 52, pp. 1-61, 2007.

[56] B. Derjaguin and L. Landau, "The theory of stability of highly charged lyophobic sols and coalescence of highly charged particles in electrolyte solutions," *Acta Physicochim,* vol. 58, pp. 633-

652, 1941.

[57] E. Verwey and J. Overbeek, "Theory of the stability of lyophobic colloids," *Journal of Colloid Science,* vol. 10, pp. 224-225, 1955.

[58] I. Zhitomirksy, "Cathodic electrodeposition of ceramic and organoceramic materials. Fundamental aspects," *Advances in Colloid and Interface Science,* vol. 97, pp. 279-317, 2002.

[59] Y. Fukada, N. Nagarajan, W. Mekky, Y. Bao, H.-S. Kim and P. Nicholson, "Electrophoretic deposition - mechanisms, myths and materials," *Journal of Materials Science,* vol. 39, pp. 787-801, 2004.

[60] D. De and P. Nicholson, "Role of Ionic Depletion in Deposition during Electrophoretic Depositon," *Journal of the American Ceramic Society,* vol. 82, pp. 3031-3036, 1999.

[61] P. Sarkar and P. Nicholson, "Electrophoretic deposition (EPD): mechanisms, kinetics, and application to ceramics," *Journal of the American Ceramic Society,* vol. 79, pp. 1987-2002, 1996.

[62] Y.-C. Wang, I.-C. Leu and M.-H. Hon, "Kinetics of electrophoretic deposition for nanocrystalline zinc oxide coatings," *Journal of the American Ceramic Society,* vol. 87, pp. 84-88, 2004.

[63] J. Cordelair and P. Greil, "Discrete element modeling of solid formation during elecrophoretic deposition," *Journal of Materials Science,* vol. 39, pp. 1017-1021, 2004.

[64] D. Coelho, J.-F. Thovert and P. Adler, "Geometrical and transport properties of random packings of spheres and aspherical particles," *Physical Review E,* vol. 55, pp. 1959-1979, 1997.

[65] S. Put, J. Vleugels and O. V. d. Biest, "Functionally graded WC-Co materials produced by electrophoretic deposition," *Key Engineering Materials,* vol. 45, pp. 1139-1145, 2001.

[66] S. Put, G. Anne, J. Vleugels and O. V. d. Biest, "Functionally graded ZrO2-WC composites processed by electrophoretic deposition," *Key Engineering Materials,* vol. 46, pp. 189-192, 2002.

[67] C. Zhao, L. Vandeperre, J. Vleugels and O. V. d. Biest, "Cylindrical Al2O3/TZP functionally graded materials by EDP," *British Ceramic Transcript,* vol. 99, pp. 284-287, 2000.

[68] A. Boccaccini and I. Zhitomirsky, "Application of electrophoretic and electrolytic deposition techniques in ceramics processing," *Current Opinion in Solid State & Materials Science,* vol. 6, pp. 251-260, 2002.

[69] R. German, "Coarsening in Sintering: Grain Shape Distribution, Grain Size Distrubution, and Grain Growth Kinetics in Solid-Pore Systems," *Critical Reviews in Solid State and Materials Science,* vol. 35, pp. 263-305, 2010.

[70] J. Pepin, W. Borland, P. O'Callaghan and R. Young, "Electrode-Based Causes of Delaminations in Multilayered Ceramic Capacitors," *Journal of the American Ceramic Society,* vol. 72, pp. 2287-2291, 1989.

[71] N. Bansal and J. Lamon, Ceramic Matrix Composites: Materials, modeling and properties, Hoboken: John Wiley & Sons, Inc., 2015.

[72] J. Morell, D. Economou and N. Amundsen, "Chemical vapor infiltration of SiC with microwave heating," *Journal of Materials Research,* vol. 8, pp. 1057-1068, 1993.

[73] D. Gupta and J. Evans, "A mathematical model for chemical vapor infiltration with microwave heating and external cooling," *Journal of Materials Research,* vol. 6, pp. 810-819, 1991.

[74] A. Ortona, A. Donato, G. Filacchioni, U. De Angelis, A. La Barbera, C. Nannetti, B. Riccardi and J. Yeatman, "SiC-SiC f CMC manufacturing by hybrid CVI-PIP techniques: process optimisation," *Fusion Engineering and Design,* vol. 51, pp. 159-163, 2000.

[75] M. Kotani, A. Kohyama and Y. Katoh, "Development of SiC/SiC composites by PIP in combination with RS," *Journal of Nuclear Materials,* vol. 289, pp. 37-41, 2001.

[76] D. Behrendt and M. Singh, "Effect of carbon preform pore volume and infiltrants on the composition of reaction-formed silicon carbide materials," *Journal of Material Synthesis and Processing,* vol. 2, pp. 117-123, 1994.

[77] Y. Wang, S. Tan and D. Jiang, "The fabrication of reaction-formed silicon carbide with controlled microstructure by infiltrating a pure carbon preform with molten Si," *Ceramics International,* vol. 30, pp. 435-439, 2004.

[78] C. Byrne and D. Nagle, "Carbonization of wood for advanced materials applications," *Carbon,* vol. 35, pp. 259-266, 35.

[79] J. Margiotta, D. Zhang, C. Nagle and C. Feeser, "Formation of dense silicon carbide by liquid silicon infiltration of carbon with engineered structure," *Journal of Materials Research,* vol. 23, pp. 1237-1248, 2008.

[80] G. Gnesin and A. Raichenko, "Kinetics of the liquid-phase reactive sintering of silicon carbide," *Poroshkovya Metallurgiya,* vol. 5, pp. 35-43, 1971.

[81] F. Gern and W. Krenkel, "Morphology and infiltration dynamics of liquid siliconized carbon/carbon," in *Proceedings of the 10th International Conference on Composite Materials*, Whistler B.C., 1995.

[82] M. Hon, R. Davis and D. Newbury, "Self-Diffusion of Si-30 in Polycrystalline Beta-SiC," *Journal of Materials Science,* vol. 15, pp. 2073-2080, 1980.

[83] R. Fisher, The Design of Experiments, Macmillan, 1935.

[84] R. Mukerjee and J. Wu, A Modern Theory of Factorial Design, New York: Springer New York, 2006.

[85] J. Antony, Design of experiments for engineers and scientists, EBSCO Publishing, 2014.

[86] L. Eriksson, E. Johansson, N. Kettaneh-Wold, C. Wikstrom and S. Wold, Design of experiments. Principles and applications, Umetrics Academy, Sweden, 2000.

[87] M. Tabatabaian, COMSOL5 for Engineers, Mercury Learning & Information, 2015.

[88] A. Safinajafabadi, R. Sarraf-Mamoory and Z. Karimi, "Effect of organic dispersants on structural and mechanical properties of Al2O3/ZrO2 composites," *Materials Research Bulletin,* vol. 47, pp. 4210-4215, 2012.

[89] W. Tscharnuter, "Mobility measurements by phase analysis," *Applied Optics,* vol. 40, no. 23, pp. 3995-4003, 2001.

[90] B. Petrillow and C. Moitzi, "Faster, More Sensitive Zeta-Potential Measurements with cmPALS and the Litesizer™ 500," Anton Paar, 2017.

[91] J. Margiotta, "Study of Silicon Carbide formation by Liquid Silicon Infiltration of Porous Carbon Structures," John Hopkins Univeristy - PhD Dissertation, Baltimore, 2009.

[92] F. A. Silva, C. N. and R. Toledo Filho, "Tensile behavior of high performance (sisal) fibers," *Composite Science and Technology,* vol. 68, pp. 3438-3443, 2008.

[93] Beuhler, a division of Illinois Tool Works Inc., Buehler SumMet - A guide to Materials Preparation and Analysis, Lake Bluff, IL: Buehler, 2007.

[94] W. Rasband, "ImageJ2," U.S. National Institutes of Health, Bethesda MD, 1997-2022.

[95] H. Richter and P. Peters, "Tensile strength distribution of all-oxide ceramic matrix mini-composites

with porous alumna matrix phase," *Journal of the European Ceramic Society,* vol. 36, no. 13, pp. 3185-3191, 2016.

[96] A. Nagaraja, S. Gururaja and A. Udayakumar, "Tensile behavior of ceramic matrix minicomposites with engineered interphases fabricated by chemical vapor infiltration," *Journal of the European Ceramic Society,* vol. 42, pp. 2659-2671, 2022.

[97] F. Rebillat, A. Guette, L. Espitalier, C. Debieuvre and R. Naslain, "Oxidation resistance of SiC/SiC micro and minicomposites with a highly crystallized BN interphase," *Journal of the European Ceramic Society,* vol. 18, pp. 1809-1819, 1998.

[98] R. Naslain, "Design, preparation and properties of non-oxide CMCs for application in engines and nuclear reactors: an overview," *Composites Science and Technology,* vol. 64, pp. 155-170, 2004.

[99] H. Xu, L. Li, R. Zheng and C. Ma, "Influences of the dip-coated BN interface on mechanical behavior of PIP-SiC/SiC minicomposites," *Ceramics International,* vol. 47, no. 11, pp. 16192-16199, 2021.

[100] B. Xu, H. Yang, R. Luo, L. Wang, J. Huang and C. D., "Fabrication and performance of mini SiC/SiC composites with an electrophoresis-deposited BN fiber/matrix interphase," *Journal of the European Ceramic Society,* vol. 42, pp. 1904-1911, 2022.

[101] K. Konig, S. Novak, A. Boccaccini and S. Kobe, "The effect of the particle size and the morphology of alumina powders on the processing of green bodies by electrophoretic deposition," *Journal of Materials Processing Technology,* vol. 210, pp. 96-103, 2010.

[102] Y. Liu, Q. Fu, L. Li, Q. Shen, H. Li and K. Li, "Microstructure and mechanical properties of SiC fibres after exposure at elevated temperature," *Advances in Applied Ceramics,* vol. 115, no. 8, pp. 449-456, 2016.

[103] T. Ishikawa, "Recent developments of the SiC fiber Nicalon and its composites including properties of the SiC fiber Hi-Nicalon for ultra-high temperature," *Composites Science and Technology,* vol. 51, pp. 135-144, 1994.

Appendix B: Code and Macros

B1 – ImageJ Macro for converting image to 8 bit and setting scale

```
open("T:/…/B1-1-1.tif");

run("8-bit");

//setTool("line");

//line is drawn over calibrated microscope imposed scale
```

```
makeLine(183, 261, 537, 261);
run("Set Scale...", "distance=354 known=100 unit=um");
saveAs("Tiff", "T:/…/Banalysis/B1-1-1b.tif");
close();
```

B2 – Macro for measuring coating thickness from optical microscopy

```
//create arrays with x and y coordinates of previously placed points at centres of fibres
//use multi-point selection tool to indicate the centre of up to 60 fibres
//use Analysis>Measure to generate X and Y coordinates of each point
//note: to create comma seperated list use =concatenate(transpose(A1:A100)&",") in excel where x or y
//coordinates are placed in column A

x1 = newArray(123.00162,        …,        1052.49888);
y1 = newArray(789.00084,        …,        776.50194);

//array m1 indicates length of lines in pixels
m1 = newArray(-75, 75);

//variable sc to account for pixel to um ratio
//get scale by drawing line over scale bar then using Analysis>Set Scale
sc = 3.66;

// select the text file that will hold the values
// note: empty text file needs to be created prior to running macro
// remember to update file name between samples

file=File.open("T:\\...\\Aanalysis\\a92.txt");

//for each of the plotted points at the centre of the fibres

for ( i=0; i<x1.length; i++) {

//generate east and west line of length m1[j] pixels
```

```
	for(j = 0; j<m1.length; j++) {

		a = x1[i];
		b = y1[i];
		c = a + m1[j];

		makeLine(a, b, c, b);
//evaluate pixel value at each pixel along generated line (value 255 indicates black pixel, value 0 indicates
//white pixel)
		profile = getProfile();
		for (q=0; q<profile.length; q++) {
			setResult("Value", q, profile[q]);
			updateResults();
			s = q/sc;
			print(file, " "+s+"\t "+profile[q]+"\t ");
			}
		}
//repeat for North and South lines
	for(h=0; h<m1.length; h++) {

		a = x1[i];
		b = y1[i];
		c = b + m1[h];

		makeLine(a, b, a, c);

		profile = getProfile();
			for (r=0; r<profile.length; r++) {
			setResult("Value", r, profile[r]);
			updateResults();
			u = r/sc;
			print(file, " "+u+"\t "+profile[r]+"\t ");
			}
```

```
                    }
}
//clear the results to prepare for next image
run("Clear Results");
```